Universitetet i Stavanger

**FACULTY OF SCIENCE AND TECHNOLOGY**

# MASTER'S THESIS

| | |
|---|---|
| Study program/Specialization:<br><br>Petroleum Geoscience Engineering | Spring semester, 2019<br><br>Open |
| Author:<br>Laura Vaiciulyte | ……<br>(signature of author) |
| Faculty supervisor:<br><br>Christopher Townsend | |
| Title of master's thesis:<br><br>Structural Analysis of Half-Graben Growth Geometries, Gulf of Corinth, Greece. | |
| Credits (ECTS): 30 | |
| Keywords: Structural Geology<br>Half-Graben<br>Syn-rift<br>Growth Geometries<br>Normal Faults<br>LiDAR<br>Gulf of Corinth<br>Greece | Number of pages: 139<br><br>Stavanger, 25.06.2019 |

# Structural Analysis of Half-Graben Growth Geometries, Gulf of Corinth, Greece

Laura Vaiciulyte

25th June 2019

# Abstract

## Structural Analysis of Half-Graben Growth Geometries, Gulf of Corinth, Greece

Laura Vaiciulyte
The University of Stavanger, 2019
Supervisor: Chris Townsend

The Peloponnese peninsula in mainland Greece is a highly faulted region due to the active rift in the Gulf of Corinth. The rift is relatively recent and contains highly preserved structures and sediments, making it an excellent area for structural and sedimentological syn-rift strata growth geometry analyses. Syn-rift sequences absent of growth strata geometries can be observed at several locations in the southern area of the Gulf of Corinth. The growth strata sequences are typically characterized by significant changes in dip and thickness. In this project, the locations visited in the Gulf of Corinth lack the conventional evidence of growth geometries, therefore, display a deficiency of typical characteristics of dip increase down-section and thickness increase towards a fault. This project focuses on growth strata deposit analysis and the syn-rift characterization issue when considering growth strata absent sequences, due to the syn-rift strata importance for petroleum exploration industry as a potential hydrocarbon reservoir area.

The main challenge is the discrimination between syn-rift and post-rift packages. Previously, general mapping and field work data has led to inconclusive results; high quality structural analysis may provide new insight into the presence and characteristics of syn-rift growth strata. Analysis of the study area is accomplished using a combination of field observations, Light Detection and Ranging (LiDAR) data with photographs and photogrammetry data. The purpose of the additional photographs and LiDAR data are to collect detailed measurements of the bedding geometries and to assist in determining the absence of growth geometries in a number of selected half-grabens. The acquired LiDAR data were processed and input into Petrel EP Software Platform, used for detail structural analysis of the study areas.

The detailed structural analysis results in the lack of growth geometries in syn-rift packages,

suggesting new criteria requirement for a precise syn-rift strata identification, followed by several possible past geomorphology scenario propositions. Additionally, analogue quality assessment of Norwegian Continental Shelf resulted in a few areas exhibiting similar syn-rift features to GOC and proposing a possibility for lack of growth geometries as a global feature.

# Acknowledgements

I would first like to express gratitude to my supervisor Chris Townsend for providing relevant articles, his continuous support and guidance.

Alejandro Escalona for his feedback, criticism and discussions regarding the thesis and throughout all of the years of studying.

University of Stavanger's staff for their IT help and suggestions regarding the thesis. University itself for providing the necessary software licenses, LiDAR scanner tool and financial support.

Fellow students for help, support and discussions during fieldtrips and thesis writing.

Finally, I must express my profound gratitude to my family and friends for their unfailing support, encouragement, patience and constant help throughout the years of studying, the process of writing this thesis and conducting research.

The completion of this thesis could not have been possible without the assistance and support of many people whose names may not all be enumerated. Their contributions are sincerely appreciated and gratefully acknowledged.

Laura Vaiciulyte

# Contents

# List of Figures

# List of Tables

# Chapter 1

# Introduction

## 1.1 Background

The Gulf of Corinth (GOC) is a region of mainland Greece characterized by intense seismic activity and known as one of the Earth's most active continental rift systems (Ambraseys and Jackson 1997). The Corinth rift is an asymmetric basin formed as a high strain band of north-south extension across mainland Greece induced by extensional plate tectonism (Nixon et al. 2016). The rift is still in its first stage of rifting; therefore, the syn-rift sediments are well preserved and untampered, providing excellent insight into the tectonic and stratigraphic development of the rift. This area is considered to be a classic rift basin.

Growth geometry deposits are syn-rift strata deposited during rifting and associated fault movement, characterized by layer thickening towards faults and increasing dip with age. Hanging-wall of the normal fault is down-thrown, creating free accommodation space which sediments infill simultaneously with the fault movement. The foot-wall is up-thrown and prone to erosion, supplying sediments deposited in the hanging-wall. The layer thickness is generally controlled by available accommodation space, sediment supply and sedimentation rate. In fact, sedimentation rate exceeding sediment supply causes thickness and facies alteration. Displacement and fault rotation events incline the deposited strata generating a change in dip and contribute to layer's thickness increase towards the fault and facies change development (Figure 1.1). Thus, fault movement, accommodation space creation and sediment supply lead to the development of growth geometries. Additionally, fault movement and sediment infilling results in a variety of

facies distributions expected in syn-rift intervals. These characterizations of growth geometries are important for identifying syn-rift strata. However, in some cases, half-graben structures appear where typical growth geometries are absent. This leads to difficulties in identifying syn-rift strata and will be analyzed in detail.

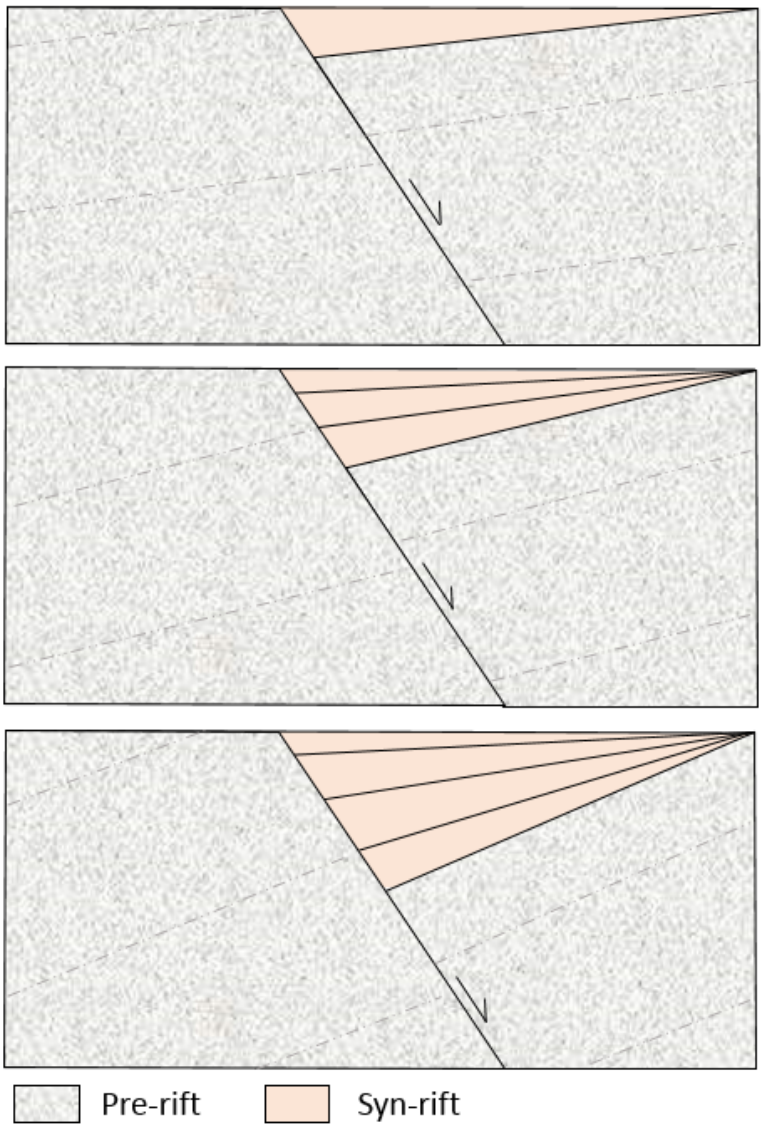


**Figure 1.1:** Schematic cross-section sketch of sequential growth geometry sequence development. Fault movement creates free accommodation space which is infilled with sediments.

## 1.2 Study Area

Detailed research was conducted in the western part of Peloponnese peninsula, in the contrast to the northeastern part, which was analyzed generally. The areas of the study were divided

into Southwestern (SW) and Northeastern (NE), due to the different data quality. The study areas of this research stretches from the Lapanagoi outcrop in the West to Xylocastro town to the East (Figure 1.2). Additionally, a substantial northern GOC onshore area was examined in order to acquire field data of supplementary half-graben outcrops. The analyzed northern part was not used for this research by the reason of lack of outcropping sediments.

### 1.2.1 Study Area A

The study area A consists of several outcrops located onshore south of the GOC, with specific outcrops from SW area selected focusing on half-graben structures (Lapanagoi, Roghi, Vrachni and Monastery outcrops). Several half-graben structures in the Gulf of Corinth area have been studied and mapped in detail by scientists in order to explain the sediment infill history, growth strata and tectonic development of this region (Hemelsdaël et al. 2017; Ford, Hemelsdael, et al. 2016; Nixon et al. 2016; Reilinger et al. 2010; Goldsworthy and Jackson 2001; Gawthorpe and Leeder 2000; Kontopoulos et al. 1993; Le Pichon and Angelier 1979). Numerous researches imply growth strata in syn-rift packages, although, a few generate cross-sections indicating lack of growth geometry characteristics. Therefore, due to the deficiency and disagreement of studies, the past geomorphology including growth strata development in the area is debatable.

### 1.2.2 Study Area B

The study area B is situated in the east, stretching from Ziria town in the south to Xylocastro town in the north. The study area B is dominated by numerous hardly accessible sediment outcrops requiring several months of detailed mapping. The eastern study area has been investigated for four days in the field, consisting of Xylocastro, Amphithea, Evrostini, Mavro, Kyllini and Kefalari East and West outcrops (Figure 1.3). Accessible outcrops in the area were examined generally, collecting field and photograph data (Kyllini, Kefalari East and Kefalari West). The northeastern Peloponnese area has been also investigated by Gawthorpe, Leeder et al. (2018) previously.

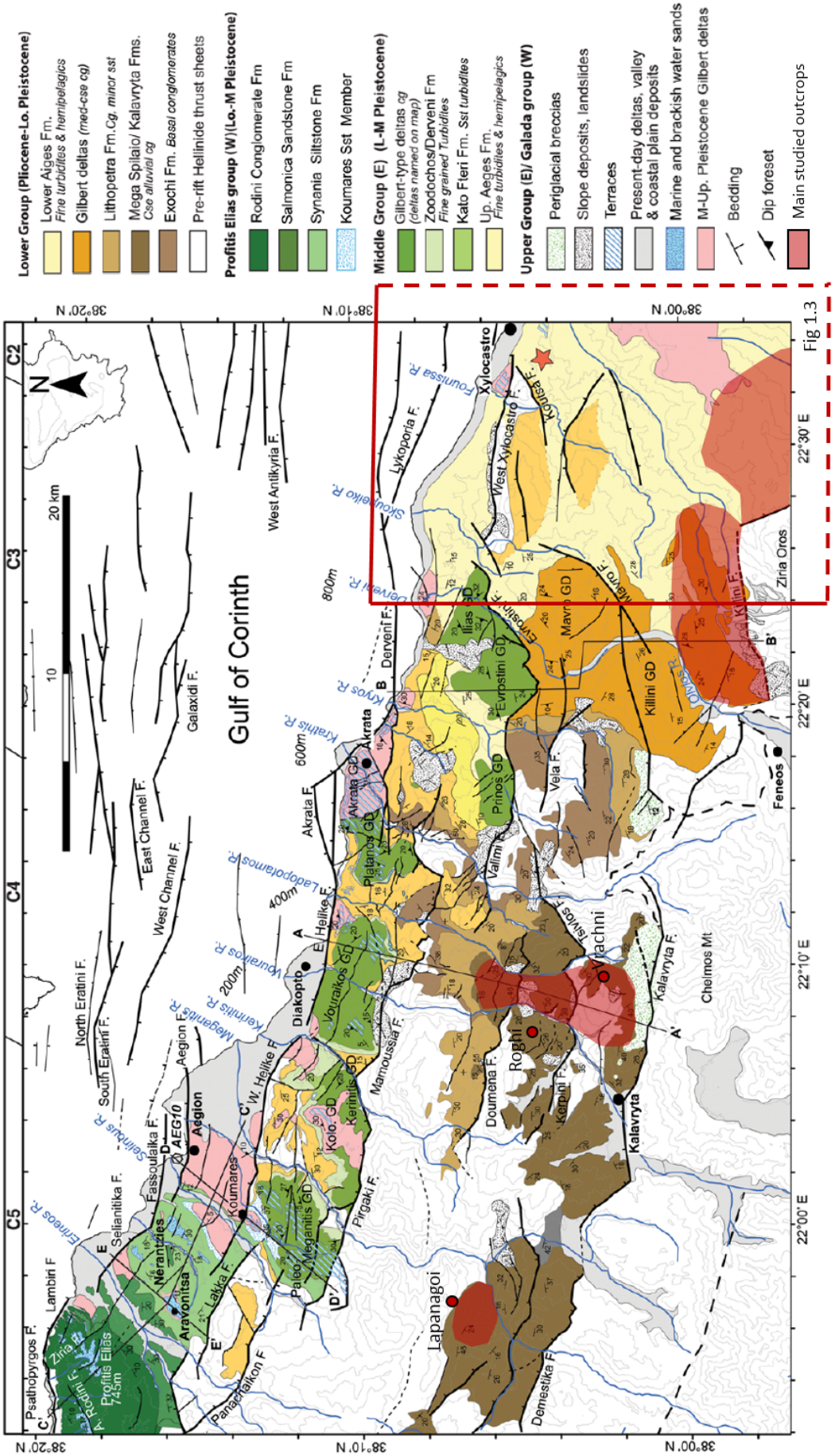


**Figure 1.2:** Geological map of the study area of the northern Peloponnese peninsula. Stretching from Lapanagoi in the West to Xylocastro in the east, from GOC in the north to Feneos in the south. Modified after Ford, Hemelsdael, et al. 2016.

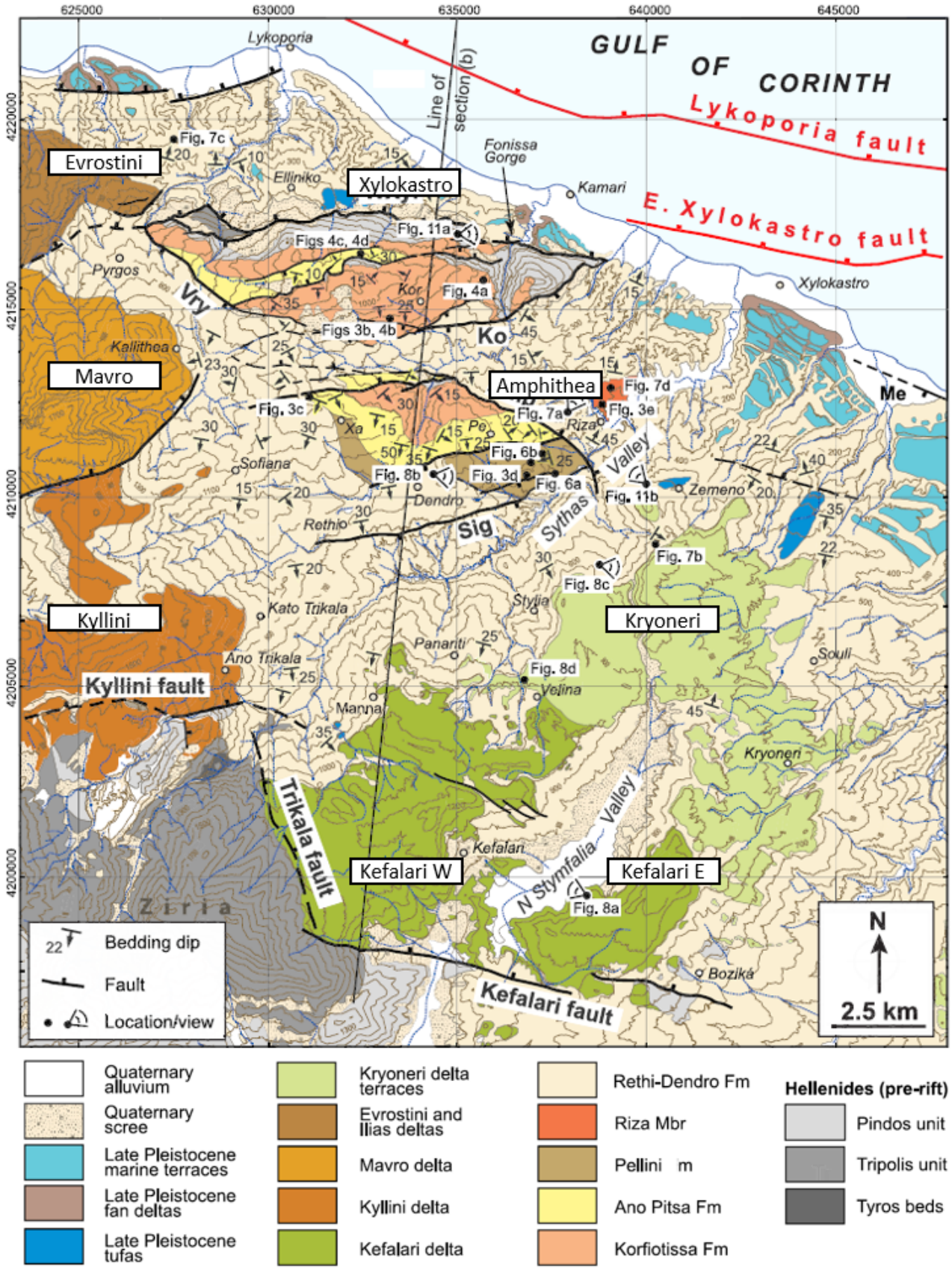


**Figure 1.3:** Study area of the eastern Peloponnese area. Location of the map is marked in Figure 1.2. Modified after Gawthorpe, Leeder, et al. 2018.

## 1.3 Previous Work

The Corinth Rift has been a popular subject of research due to its relatively current development, well preserved sediments and geological features. Over the last several years different rifting models explaining the development of the Corinthian rift system have been proposed and are still debated. Most of the researches propose a model of planar tilted faults, a so called domino block model (Moretti et al. 2003; Westaway 2002; Ford, Rohais, et al. 2013) in contradiction of listric normal fault nature theory (Doutsos and Poulimenos 1992). Some studies suggests an existence of a low-angle detachment fault at deeper crustal levels dipping northward at approximately 20° and obliquely cutting through Hellenide nappes, which initiated 1.5-1.7 Ma (Exadaktylos et al. 2003; Chery 2001; Sorel 2000; Rietbrock et al. 1996). This theory was based on the focal mechanism data from the earthquakes of Galaxidi (1992) and Egion (1995) appearing with north dipping, low-angle (12-20°) nodal planes (Westaway 2002; Sorel 2000). The detachment fault is described as stretching down-dip northwards, observed at approximate depth of 2.5km in the southern part of GOC (Westaway 2002). The theory of detachment fault was built upon by Doutsos and Polimenos (1992) who suggested that normal faults were linked to a low angle fault at deeper crustal levels. Thereafter, steep north dipping faults at approximately 40-50° are believed to have formed successively younging northwards according to Sorel (2000) (Figure 1.4). Moretti et al. (2003) research suggests an alternative theory in which the opening of the Gulf of Corinth initiated as an external phenomenon which evolved during the uplift of the Peloponnese.

All of the proposed rifting models have one thing in common - the fact that a number of normal faults outcrops south of GOC. Normal faults control the formation of syn-tectonic half-graben sub-basins (Benedicto et al. 2008). During the rifting normal fault development progressively migrate northwards (Flotte 2003; Goldsworthy and Jackson 2001; Sorel 2000). Today, the fault activity in Peloponnese area is located either close to the present day shoreline or offshore of Gulf of Corinth (Reilinger et al. 2010).

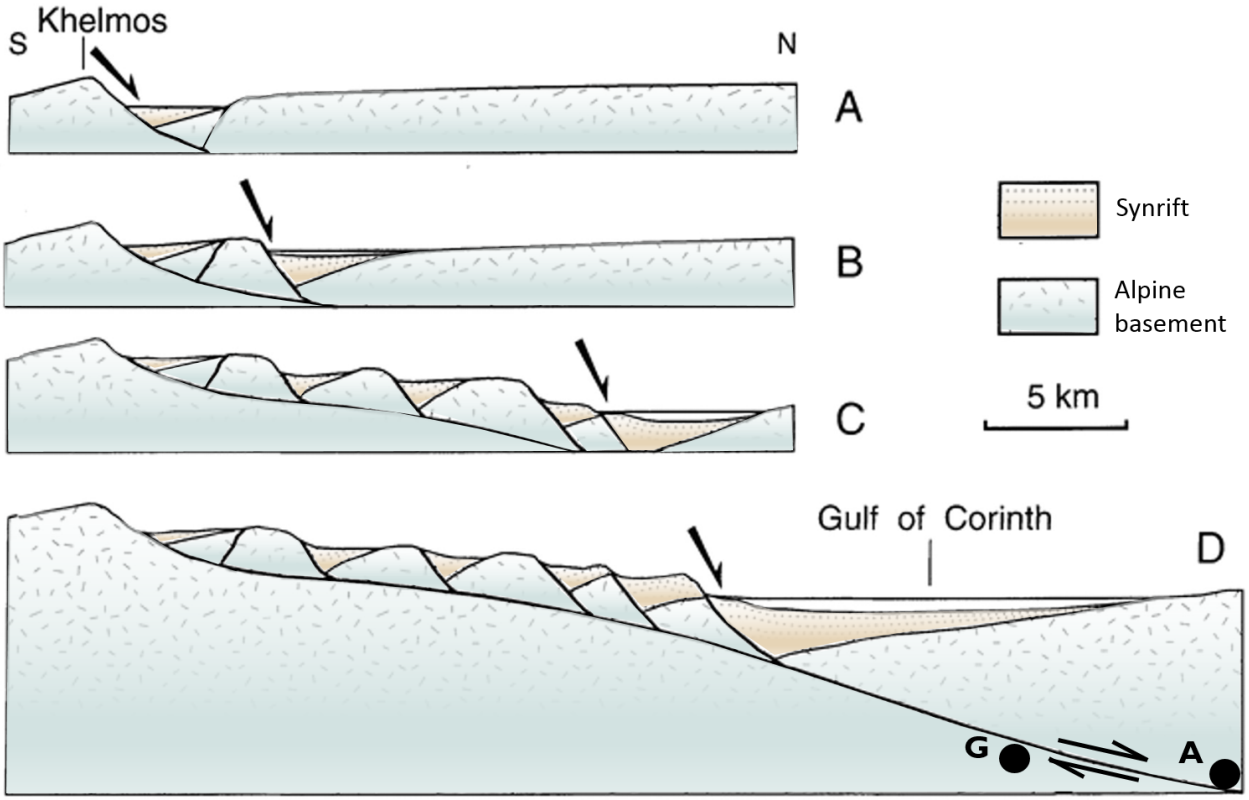


**Figure 1.4:** Schematic cross-section representing the development of the Gulf of Corinth in four steps: A- Initiation of rifting and development of Khelmos fault; B- Rifting continuation and development of steep north dipping fault; C- Further fault evolution D- Present day view of GOC and Khelmos detachment fault stretching under GOC. Black dots represent Aigion (A) and Galaxidi (G) earthquakes projections. Modified after Sorel 2000.

Several researches have been conducted by the University of Stavanger (UiS) in the southern Peloponnese area, focusing on various disciplines of fault displacement, structural mapping, geological development, subsurface investigation and syn-rift deposition. Few researches carried out by UiS students focuses on syn-rift deposition and growth geometry feature investigation in order to better understand the fault evolution and syn-rift geometries, which can be used as an analogue for rift basins all over the world. An investigation conducted in Roghi area, resulted in syn-rift strata lacking growth geometries in some parts of the area (Sigmundstad 2016). Similarly, a case study focusing on fault controlled sedimentation in Roghi area resulted in thick, clearly syn-rift sediments lacking growth geometries. The study attempted to explain past geomorphology for sediments lacking growth strata evolution, suggesting reverse drag theory (Syahrul 2014). Additionally, a research with the main focus on structural mapping of syn-rift successions in Roghi and neighboring area resulted in growth strata existence and

absence in some packages, but the absence was not discussed (Oppedal 2017).

## 1.4 Geological framework

### 1.4.1 Regional geology

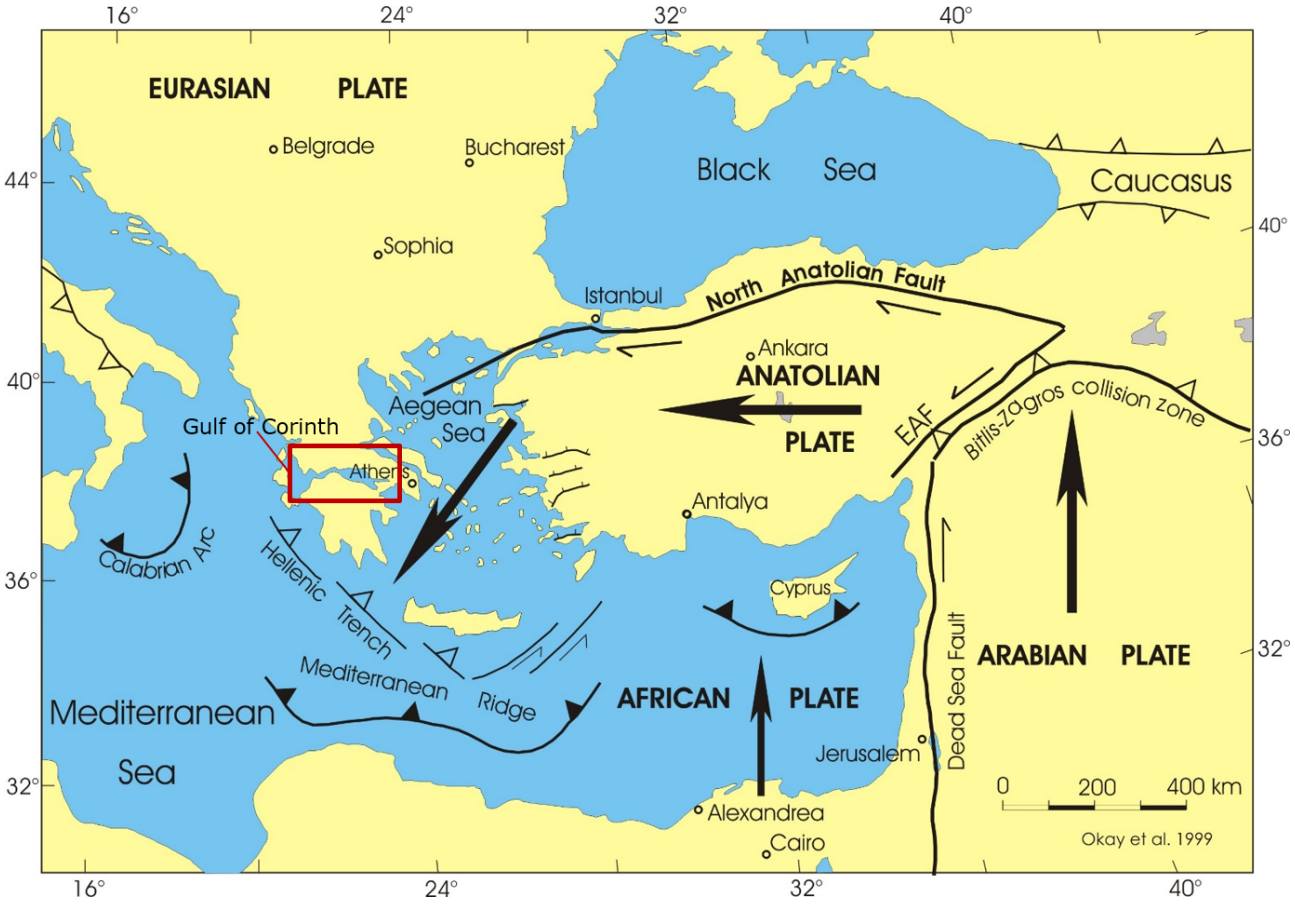


**Figure 1.5:** Map of the Mediterranean showing tectonic plate configuration. The location of Gulf of Corinth is highlighted in a red. Black arrows indicate plate movement directions. Modified after Okay et al. 1999.

The GOC is an active asymmetric system of horsts and grabens striking N110°. The Corinth rift appears in the northwestern part of Anatolian tectonic plate, north from the Mediterranean Sea. The tectonic setting in the area is highly affected by plate interplay between Anatolian, African, Arabian and Eurasian plates. The Anatolian plate encounter major interaction in the southwest where African Plate is subducting below the Anatolian plate generating the Hellenic Subduction Zone (Figure 1.5). The second major plate interaction appears in the east, where the Arabian and Anatolian plates collide initiating the development of North and East

Anatolian Faults. Anatolian plate is bounded by the right lateral North Anatolian Fault in the north and by the left lateral East Anatolian Fault in the east.

Pre-rift of the Corinth comprises a stack of N/NW-S/SE trending thrust sheets originating from its oblique position across the Hellenide mountain belt (Doutsos, Koukouvelas, et al. 2006; Dercourt 1964). The Hellenide mountain belt formed as a result of Alpine orogeny which also created the Aegean Sea due to the back-arc extension and slab rollback (Ford, Hemelsdael, et al. 2016; Armijo et al. 1996). During the Mesozoic Era, African Plate subducted to the north-northeast below the Eurasian plate, generating the Hellenic subduction system and initiating the N-S extension (Jolivet, Brun, et al. 1994; Le Pichon and Angelier 1979). Subsequently, African plate was slowed down by the collision of Arabia and Eurasia plates causing the opening of the Red Sea and slab rollback, simultaneously producing further extension in the Mediterranean Sea approximately 30 Ma ago (Jolivet and Faccenna 2000). These two major continental collisions caused an anti-clockwise rotation of the Anatolian plate resulting in pressure towards the W-SW to Hellenic Subduction zone. The collisions were followed by the rifting of the Aegean Sea in Early Miocene, causing the development of one of the fastest opening rifts - the Gulf of Corinth – in the Late Pliocene (Doutsos and Kokkalas 2001; Armijo et al. 1996). The GOC structures and its surrounding areas started developing at around 5 Ma from east to west - from Gulf of Evia to the east to Kephelonia Fault in the west (Reilinger et al. 2010).

### 1.4.2 Geological overview

The Corinthian Gulf is a 115 km long inlet of the Ionian Sea, stretching from the Strait of Rio in the west to the Corinth Canal in the east and separating the Peloponnese peninsula from mainland Greece. The northern margin of the gulf comprises of south-dipping faults. The southern part is dominated by a normal fault system comprised of more than 2.8 km thick syn-rift successions of Plio-Quaternary deposits and almost equally thick pre-rift successions representing Hellenide nappes (Figure 1.6) (Ford, Hemelsdael, et al. 2016). The fault system is currently active in the offshore and onshore coast of Gulf of Corinth with a present day differential rifting velocity of 10 ± 2mm/year (Reilinger et al. 2010). The metamorphosed

basement rocks of GOC have been uplifted and exposed in the northern Peloponnese area (Ford, Hemelsdael, et al. 2016). The exposed Peloponnese grabens comprise Late Pliocene to Early Pleistocene fluvial and lacustrine-lagoonal deposits unconformably overlain by alluvial-fan and fan-delta deposits (Kontopoulos et al. 1993). Pre-rift packages, locally referred to as basement, are metamorphosed limestone deposited along with the terrestrial sandstone deposits.

Over time, the focus of deformation in the Corinth rift migrated northwards, indicated by present-day extension and seismic activity focused towards the north (Lambotte et al. 2014). Today the southern side of the Gulf, the Peloponnese peninsula, appears at the foot of the staircase of a highly faulted area characterized by parallel north-dipping normal faults along the southern shores and offshore of Gulf of Corinth (Goldsworthy and Jackson 2001). The recent tectonic activity provides excellent exposures of the syn-rift successions allowing a thorough investigation of the evolution of the syn-rift structures and sedimentary successions.

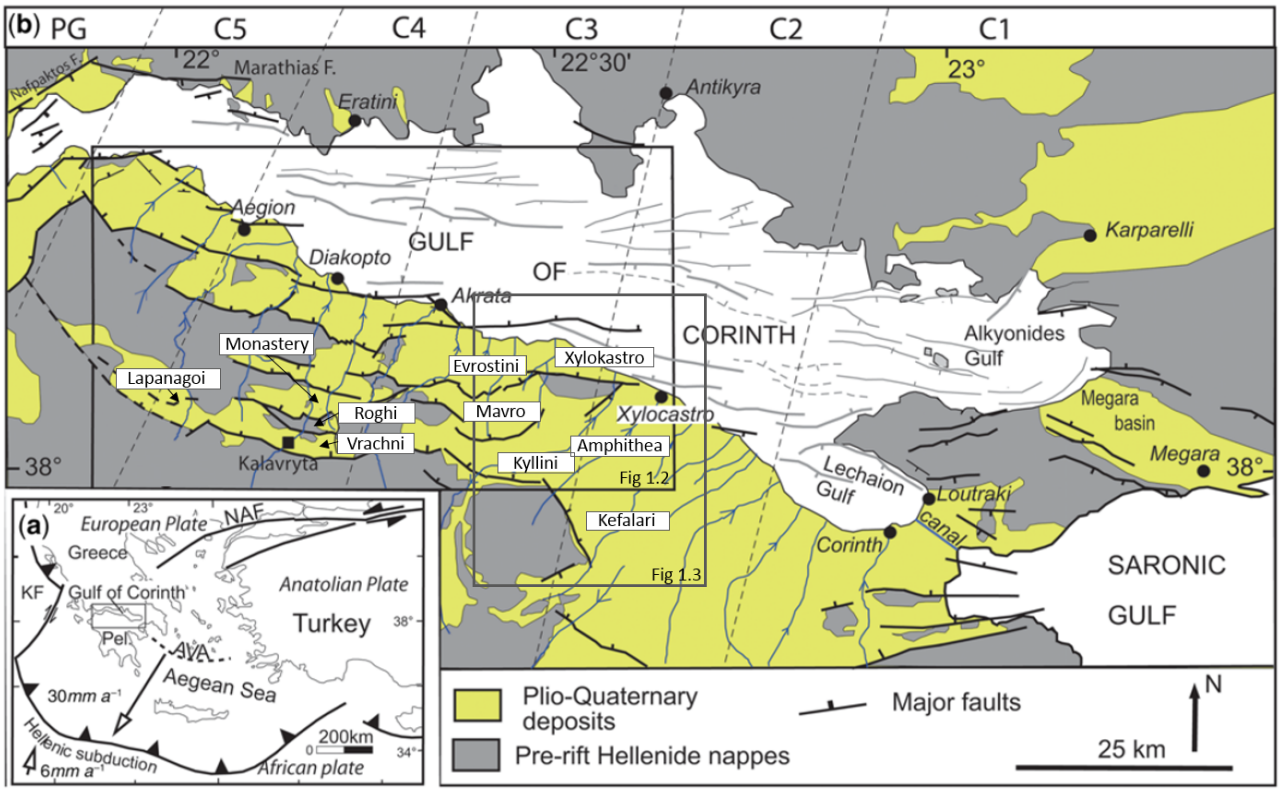


**Figure 1.6:** a) Aegean region's tectonic map displaying main plates and plate boundaries in the area. b) Tectonic map of the GOC displaying main structural elements and the distribution of Syn-rift and Pre-rift deposits. The location the study areas are highlighted with black rectangles. Modified after Ford, Hemelsdael, et al. 2016.

## 1.5 Motivation and Objectives

The results from this research of GOC will serve as an important analogue for other extensional basins including the Norwegian Continental Shelf (NCS) (e.g., North Sea, Norwegian Sea and Barents Sea), where depositional and structural uncertainties of the syn-rift strata growth geometries have become the focus of attention for oil and gas exploration. Reliable methods for the identification of possible syn-rift deposits lacking of growth strata, could help the petroleum industry. However, the observations of Syahrul (2014) indicate possible cases where the conventional growth geometry evidence does not hold true. This study provides novel insight into the interpretation of syn-rift deposits in seismic data, since a majority of reservoirs appear in highly faulted area's syn-rift deposits. If falsely identified, growth geometry structures, would result in highly overestimated reservoir volumes, wrong cap rock placement and structural trap misinterpretation. Therefore, results from this research have potential implications on the syn-rift strata definition.

The primary objective of this research is to investigate growth strata geometries in half-graben deposits by combining field mapping, LiDAR and photogrammetry data in order to define structural geometries of syn-rift deposits. This includes investigating the differences in lateral and vertical facies changes in addition to thickness and dip variations within the different hanging-wall packages. Secondly, field observations combined with LiDAR point-cloud data, photogrammetry and aerial photography will be used for interpretation of the present-day geology at the study area. Using the resulting observations, the differences in various packages will be analyzed to confirm whether or not there is sufficient evidence to support the model for lack of syn-rift deposits. If not, then alternative models need to assess the way half-graben can develop without growth geometries. Followed by detection of fundamental problems with the growth geometry model. The objectives will be accomplished following the tasks:

- Investigate a number of half-graben structures infilled with sediments,
- Acquire field and structural data, supplemented with LiDAR and photogrammetry data,
- Process the data,
- Thoroughly analyze results,

- Observe depositional variations and
- Compare the results with analogues from the NCS.

# Chapter 2

# Background Theory of Half-Graben Growth Geometry Structures

Various rift basins typically exhibit highly faulted areas generating half-grabens, rotated fault blocks and syn-sedimentary infills. The structural style is often dominated by related "domino" fault blocks. The Prince (2018) sandbox model illustrates gradual creation of parallel fault blocks with simultaneous rotation induced by extensional forces (Figure 2.1 A). The rifting results in a central graben surrounded by several normal faults developed on both flanks of the graben (Figures 2.1 B and C). The extensional forces create growth geometry development in syn-rift packages as explained in the following section.

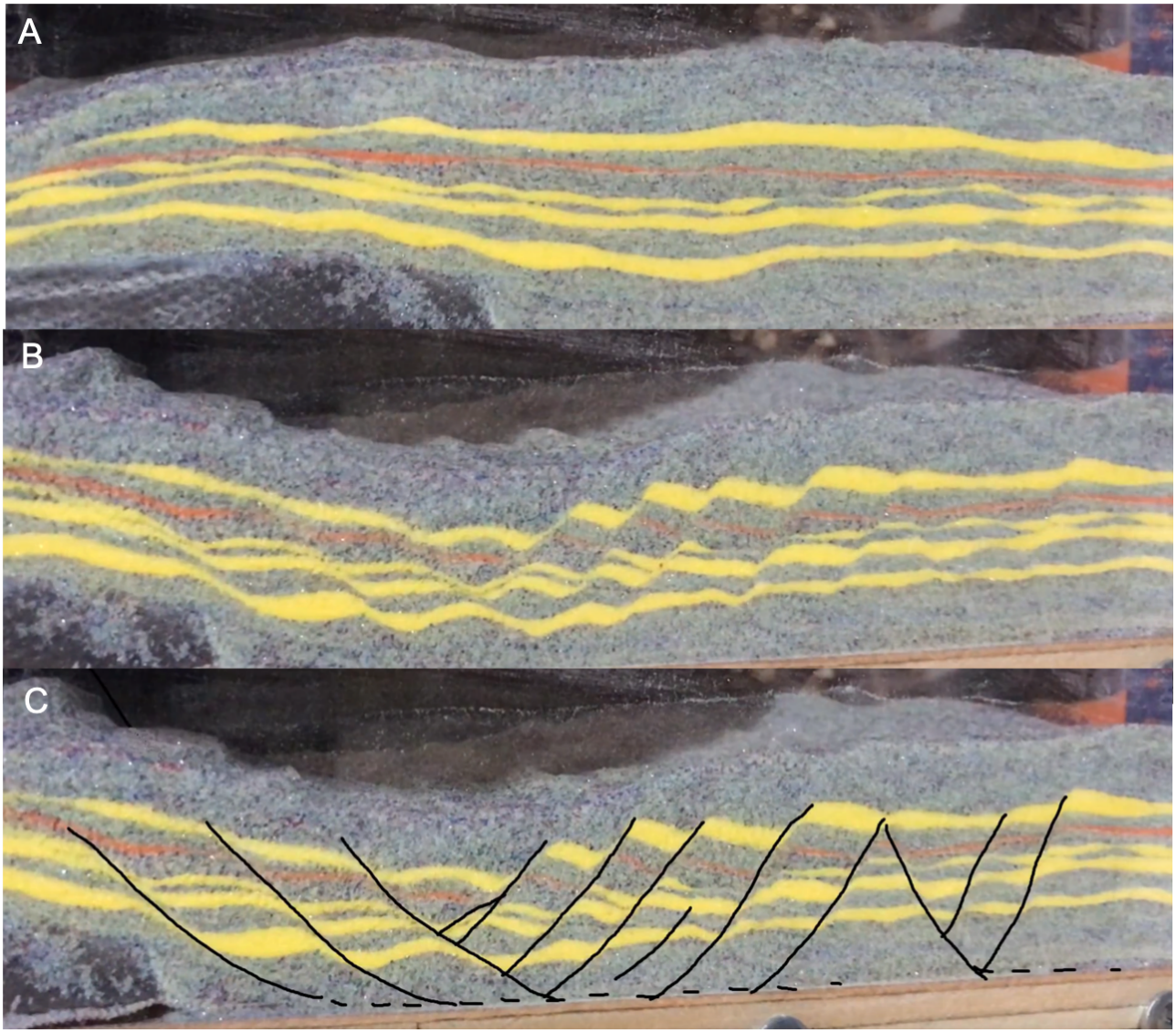


**Figure 2.1:** An illustrative sandbox model representing the formation of normal faults. Figure A represents the initial stage prior to extensional forces; Figure B illustrates the final rifting result; Figure C show an interpretation of the generated faults. Modified after Models and Prince 2018.

## 2.1 Domino Fault Model

Domino fault block model describes the influence from extensional forces on the upper lithospheric crust and the resulting evolution of tilted fault blocks (Figure 2.2). The first phase of extension leads to brittle crust fracture development, followed by the normal fault generation and further extensional forces, inducing the simultaneous tilting of the fault blocks (e.g., like a stack of dominos). Finally, the highly fault-dominated extensional phase is followed by further fault reactivation and large scale rotations (Gibbs 1984). Fault block tilting induces the

development of growth geometry structures in syn-rift packages. This is due to the sequential fault movements and fault block rotation creating accommodation space in the down-thrown hanging-wall and increased sediment supply from the uplifted foot-walls.

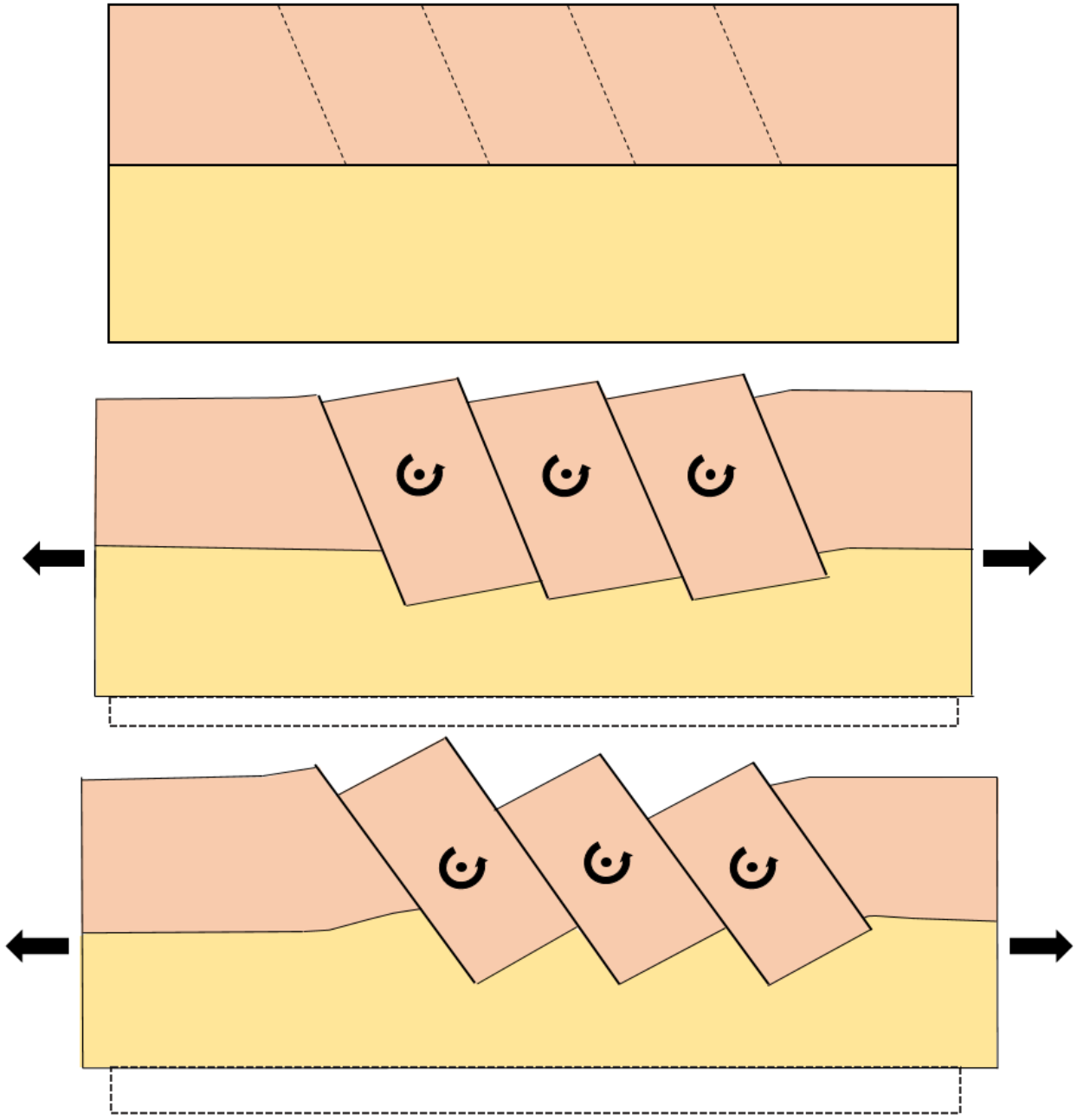

**Figure 2.2:** Graphic sketch illustrating domino fault block creation in three steps. The black side arrows portray extensional forces, oval arrows display rotational forces.

## 2.2 Rift Sequences

Development of a rift basin is induced by extensional plate tectonism. The resultant basins are characterized by linear down-faulted depressions filled with thick layers of sediment. Rift basins are dominated by fault-bounded features known as half-grabens, generated by the extensive normal faulting formed in response to the extensional stress fields. The development of the rift basin can result in various basin sizes, stages of development, sedimentation rates and sediment types (Salveson 1981). The resultant sediment packages are commonly classified as pre-, syn-, and post-rift sequences (Figure 2.3). The pre-rift sequences describe the oldest sediments deposited prior to rifting. The deposition of syn-rift occurs simultaneously with the extensional events and the post-rift sequences define the youngest sediments deposited after ceasing of the rifting.

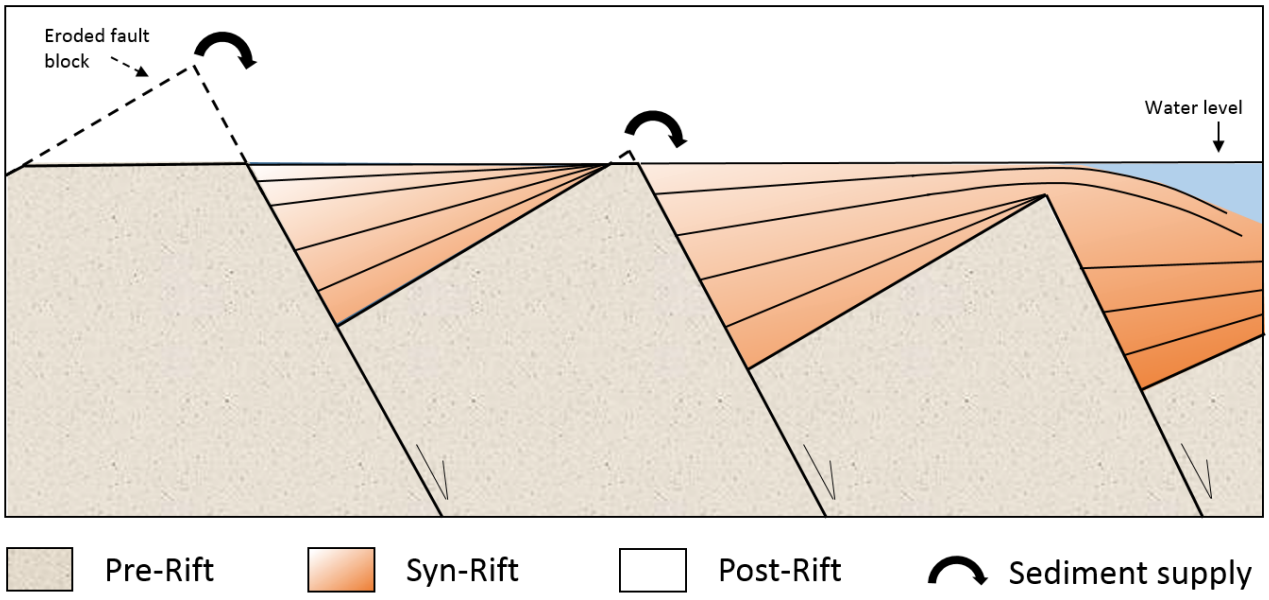


**Figure 2.3:** Schematic sketch illustrating tilted fault blocks and highlighting the distribution of pre-, syn- and post-rift sequences throughout the section. Syn-rift strata display increase in dip downwards and increase of thickness towards the fault. Post-rift sediments are deposited relatively flat, overlaying syn-rift sediments.

Syn-rift sequences can be further subdivided into early syn-rift stage, rift climax and tectonic quiescence appearing in the late syn-rift stage (Figure 2.4). Early syn-rift stage identify the first movement of the fault followed by gravitational sediment deposition. The fault movement induces a topographic depression which causes the initiation of gravity-driven movements

of sediments. The early syn-rift packages are distinguished by relatively thin sedimentary succession filling the recently developed accommodation space. The stage of rift climax is characterized by the maximum rate of fault displacement when sedimentation is outpaced by the subsidence rate. Increase in the fault displacement and initiation of sedimentation leads to rift climax sequences displaying gradual dip increase down-section, thickening towards the active fault in addition to facies changes. In general, syn-rift packages are characterized by growth geometry features. The syn-rift sequences showing growth geometries are deposited on down-thrown hanging-walls, where free accommodation space creation is generated by fault development induced by rifting. Created accommodation space is infilled with sediments eroded from uplifted foot-walls from neighboring fault blocks (Figure 2.3). Once the basins capacity is filled with sediments, the exceeding amount is deposited in the under-filled neighboring basins. Tectonic quiescence describes the stage where creation of accommodation space ceases with the end of active tectonism. The end of active tectonism causes a decrease in regional subsidence and fault block rotation. The late syn-rift sequences are characterized by a relatively thin and flat layer covering packages generated during the rift climax.

The knowledge of the depositional development history of rift strata is crucial for an accurate growth strata interpretation. The extent of growth geometries occurring depends on free accommodation space, sediment supply and eustasy level in the area. Furthermore, rift strata is characterized by different facies stacking pattern induced by various fault kinematics and the order of fault activation (Hemelsdaël et al. 2017), in addition to numerous other factors (e.g., climate, sea-level and sedimentological composition of the rock) (Prosser 2000). Therefore, the development of growth strata is influenced by fault block rotation, fault movement related subsidence, eustasy and sediment supply. On the other hand, the factors causing facies variations might be active or inactive faults, through-going river systems and sediment supply rate in addition to the sediment bypass. Figure 2.5 A displays sediment coarsening towards the active faults with identical facies distributions in each fault block including sequences nearly absent of vertical change. The effect of high sediment supply is portrayed in Figure 2.5 B where facies distribution is continuous through all three fault blocks in contrast to the scenario A. Figures 2.5 C and D exhibit inactive faults, resulting in vertical and lateral facies variations. The com-

bination of active and inactive faults is displayed in Figures 2.5 E and F portraying a complex facies distribution, resulting in lateral and vertical variations within each fault block. Scenario E illustrates an abrupt hanging-wall fault migration, while scenario F shows progressive hanging-wall fault migration with a sudden change in startigraphic sequences. It is important to note that Hemelsdael (2017) facies change model reflect syn-rift sediments dominated by growth geometry features and aspects of this model might not hold true in reality.

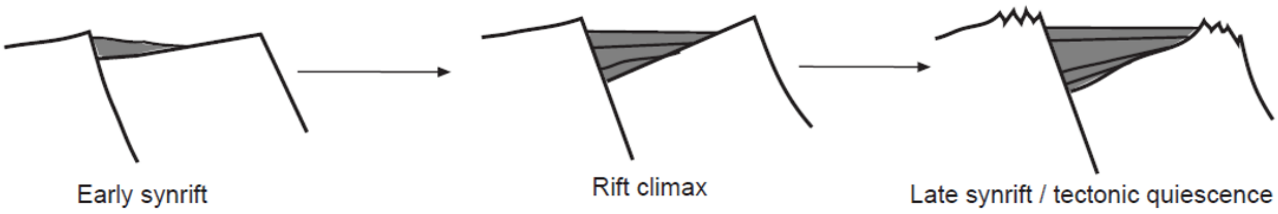


**Figure 2.4:** Schematic cross-sections portraying accommodation space development within rotated fault blocks during early syn-rift, rift climax and late syn-rift during tectonic quiescence. Syn-rift packages are marked with grey and display growth geometry development affected by spatial variation along fault lengths (Ravnas and Steel 1998).

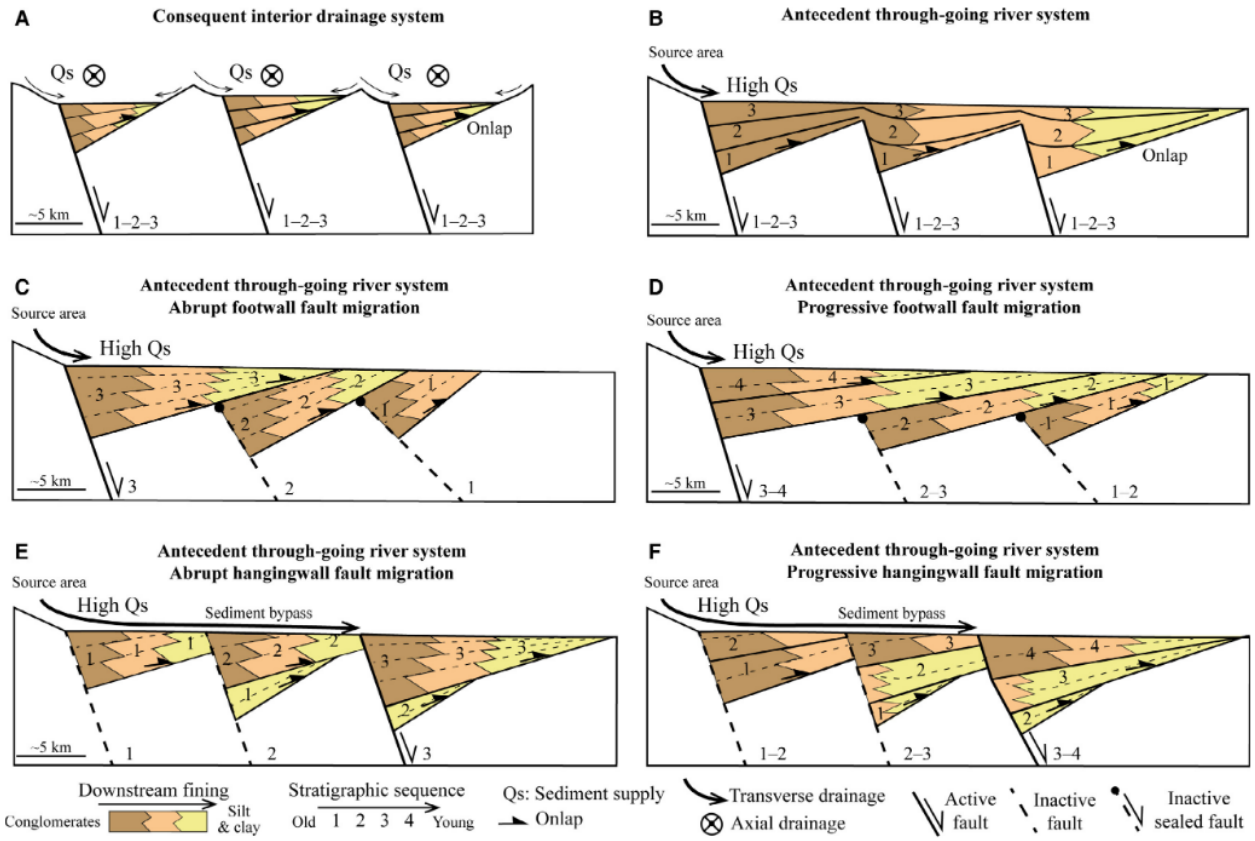


**Figure 2.5:** Conceptual scenarios illustrating the effect of various fault kinematics and the order of fault activation significance on facies distribution. The scenarios are based on results from the Gulf of Corinth. Modified after Hemelsdaël et al. 2017.

## 2.3 Sedimentation and Fault Displacement

Rift zone sedimentation is affected by the sedimentary environment, accommodation space creation and rate of sediment supply in the area (Ravnas and Steel 1998). Sedimentation rate influences the development of syn-rift packages and, therefore, growth strata structures. The ratio between sedimentation rate, fault displacement, basin capacity and water level determines the depositional environment and trend of the rift basins. The basins capacity depends on water level and accommodation space, created during the fault movement. High sedimentation rate, exceeding fault displacement rate results in sediments completely filling the available accommodation space, allowing the excess sediment to infill the neighboring basin (Figure 2.6). The resultant thick sediment packages indicate the fault's growth history (Gawthorpe and Leeder 2000). This is in contrast to moderately low sediment supply rate, where fault

displacement exceeds the sediment supply, resulting in under-filled accommodation space with relatively thin sediments.

The displacement of the faults appear along the strike of the fault planes, consistently decreasing in the direction normal to the fault plane, commonly interpreted as a reverse drag (Barnett et al. 1987). Typically, the tip of the fault exhibits fault displacement values equal to zero in opposition to the maximum displacement value appearing at the center of the fault (Figure 2.7).

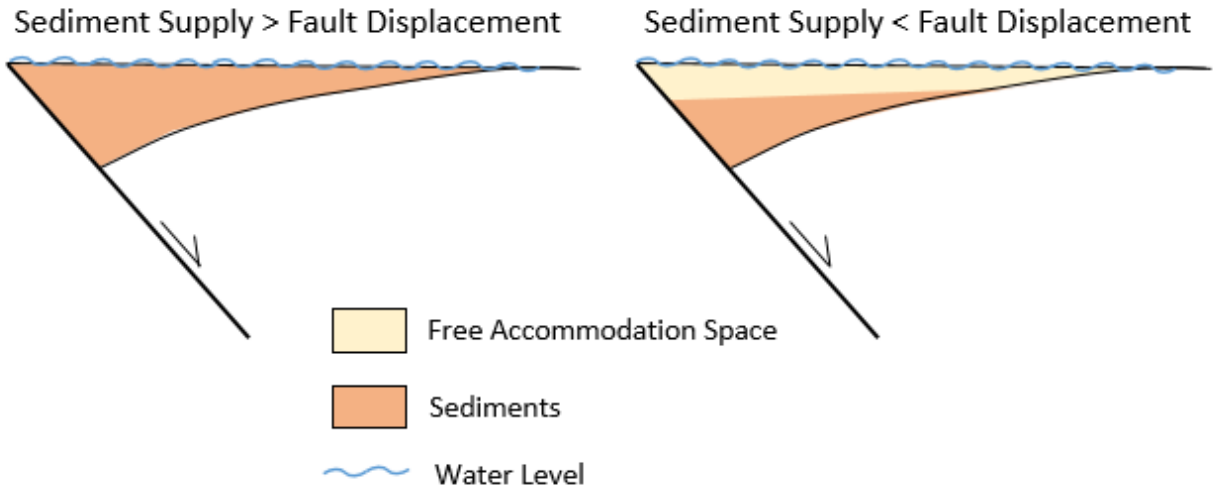


**Figure 2.6:** Conceptual sketch illustrating sedimentation and fault displacement rate relationships. Sedimentation rate exceeding fault displacement fills the accommodation space, in contrast to fault displacement rate exceeding sedimentation and under-filling the basin.

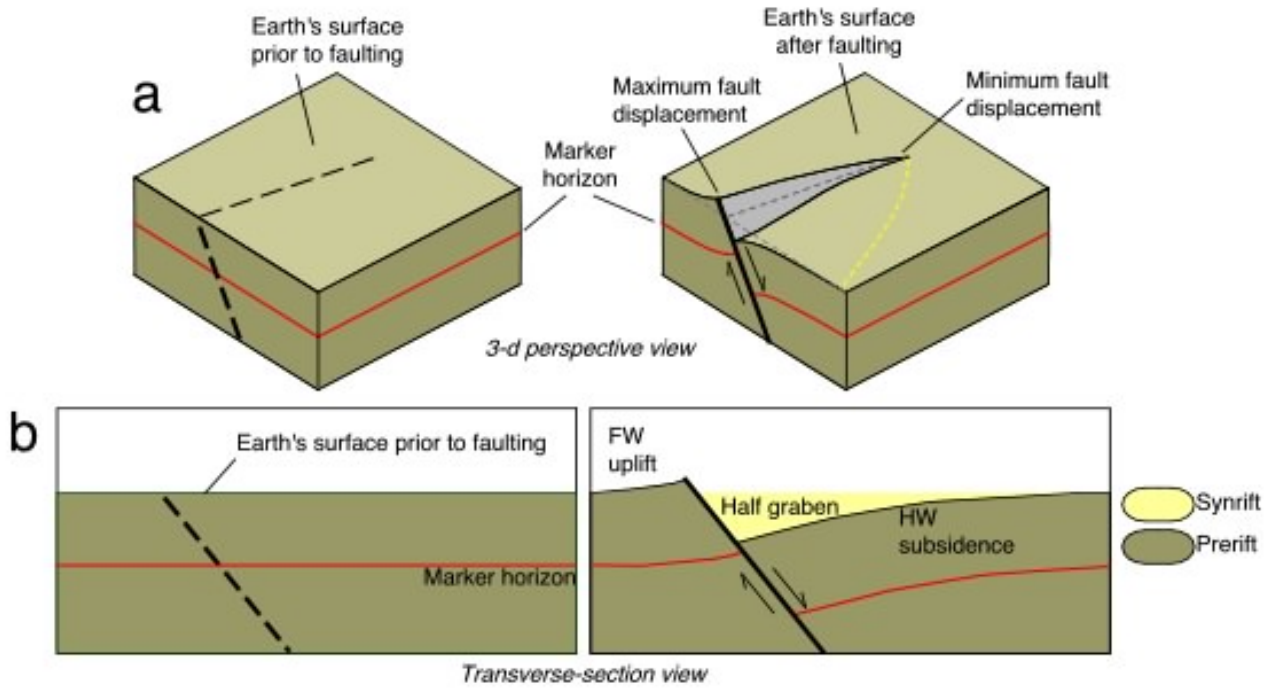


**Figure 2.7:** Schematic sketch illustrating geometry controls on fault displacement in a half-graben. Figure (a) illustrates fault displacement on earth's surface prior and during active faulting. Figure (b) portrays transverse section view of the 3D perspective represented in Figure (a) (Schlische and Withjack 2002).

## 2.4 Growth Geometry Theory

Various 3D geological modeling methods have been utilized in the literature over the years in attempts to assess the influence of external factors on growth geometry development (Einsele 2000; Cunningham 2015). Additionally, numerous geological scenarios experimented with 3D modelling illustrate varying impacts from the different factors highlighting possible geological problems.

The research of Cunningham (2015) focused on modeling various scenarios. One of the scenarios focused on modelling constant fault length, displacement and reverse drag parameters. Scenario resulted in constant accommodation space and syn-rift sedimentation patterns (Figure 2.8). This was followed by an experiment utilizing increasing fault length parameter which resulted in an increase of each in the accommodation space creation and lateral extent of each syn-rift sediment package (Figure 2.9). Additionally, the impact of fault displacement on syn-rift packages were assessed by modelling fault displacement decrease and increase, respectively,

resulting in relatively similar thicknesses of packages (Figure 2.10) and asymmetrical thicknesses (Figure 2.11). Therefore, fault displacement, fault length and accommodation space have a significant impact on the development of growth geometries. Since growth geometries develop relatively proportional to the amount of fault displacement, growth geometries identified in the field should clearly show a magnitude corresponding to the fault displacement.

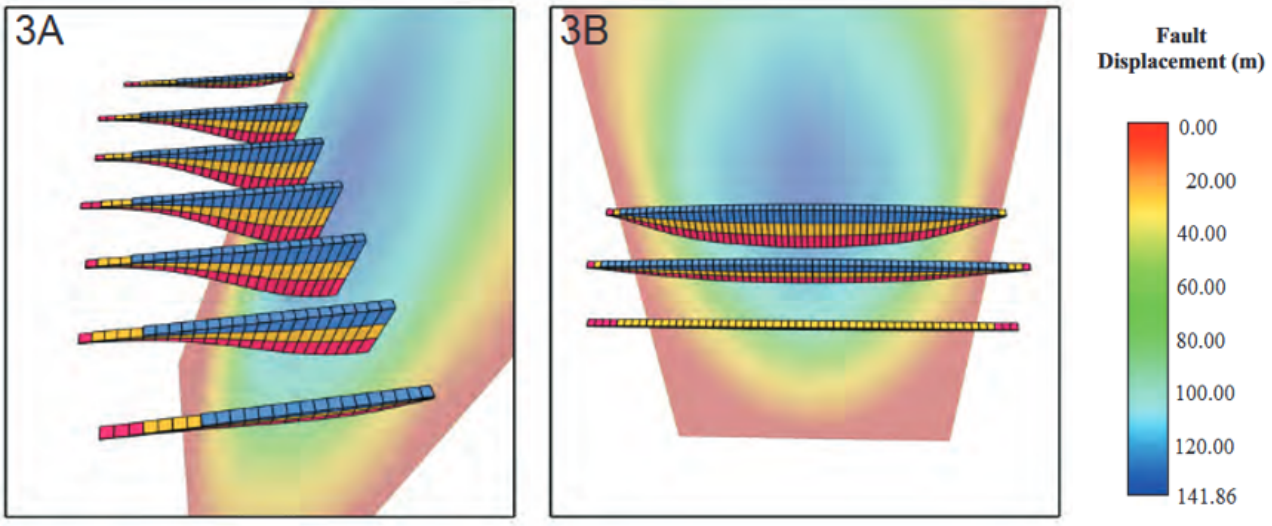


**Figure 2.8:** The results from 3D modeling of syn-rift strata utilizing constant parameters. The model display three phases of displacement highlighted with red, yellow and blue colors. Modified after Cunningham 2015.

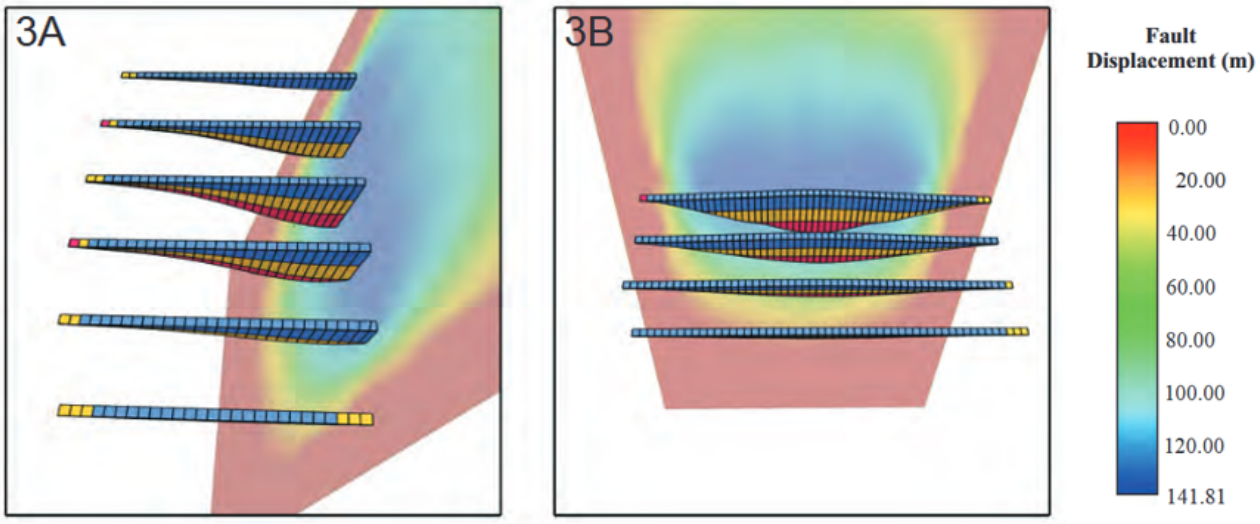


**Figure 2.9:** The results from 3D modeling of syn-rift packages with increasing fault length, displaying three phases of displacement highlighted with red, yellow and blue colors. Modified after Cunningham 2015.

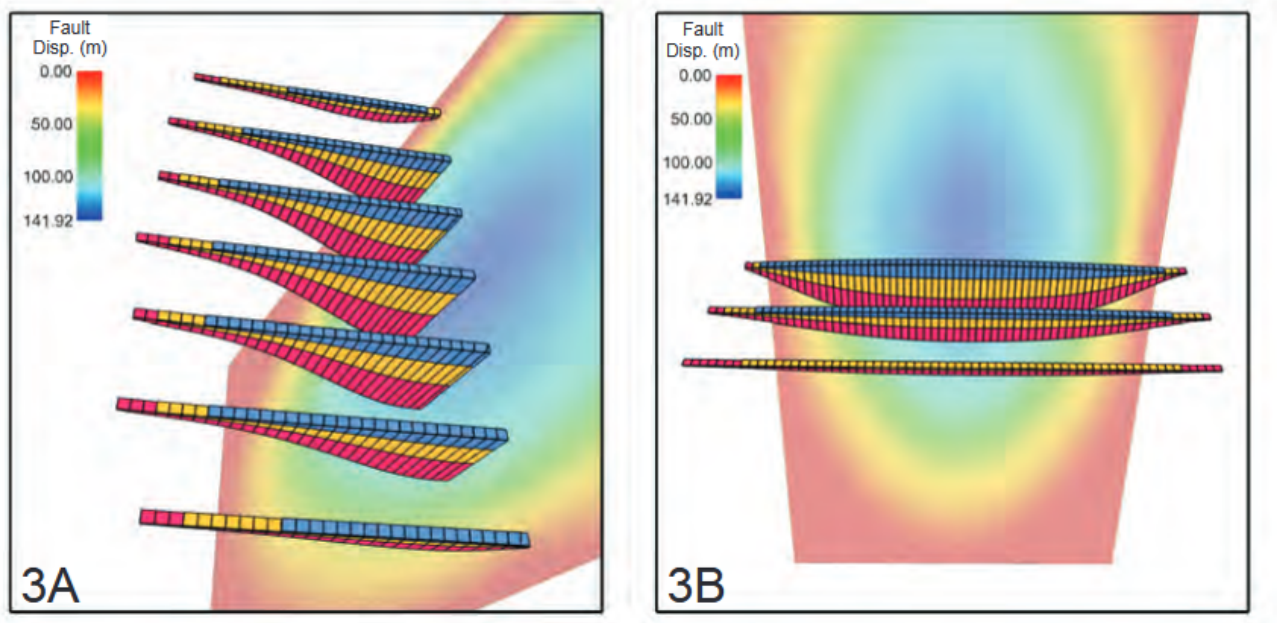


**Figure 2.10:** The results from 3D modeling of syn-rift packages utilizing decreasing fault displacement parameters, displaying three phases of displacement highlighted with red, yellow and blue colors. Modified after Cunningham 2015.

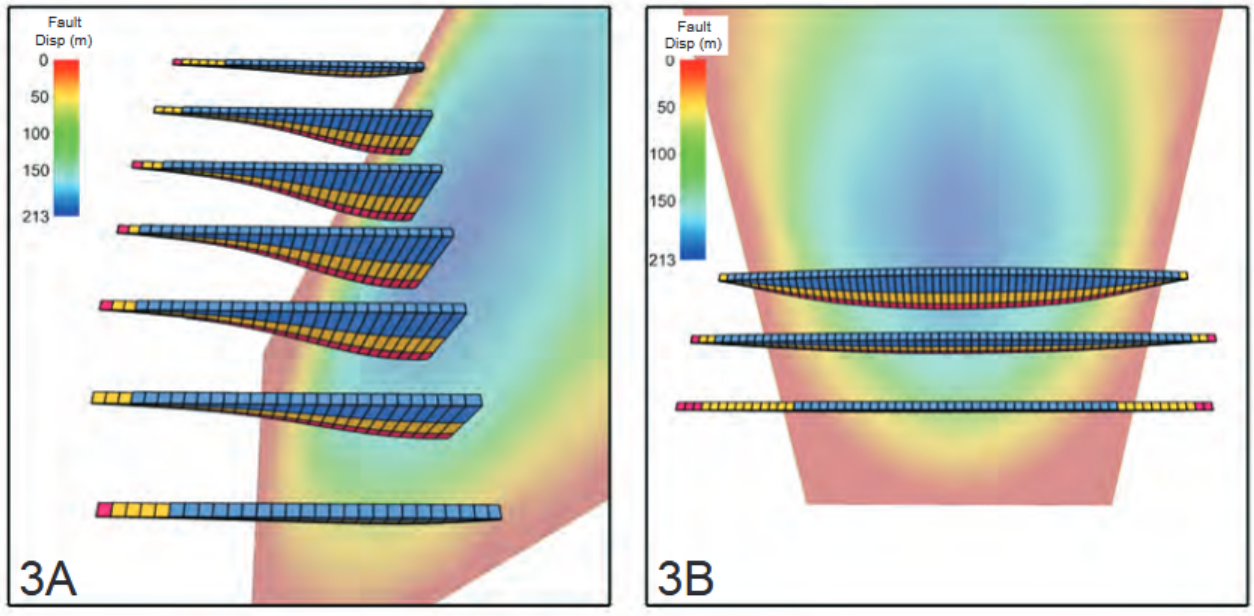


**Figure 2.11:** The results from 3D modeling of syn-rift packages utilizing increasing fault displacement parameters, displaying three phases of displacement highlighted with red, yellow and blue colors. Modified after Cunningham 2015.

# Chapter 3

# Methodology and Data Analysis

## 3.1 Introduction

Two field trips were required for examination of the study areas. A two week-long field trip took place in August 2018 and a second 10-day long field in April 2019. This chapter describes data and methods used in order to execute structural analysis of numerous half-grabens. Various procedures used for this project are subdivided into pre-field work, field work and post-field work (Figure 3.1).

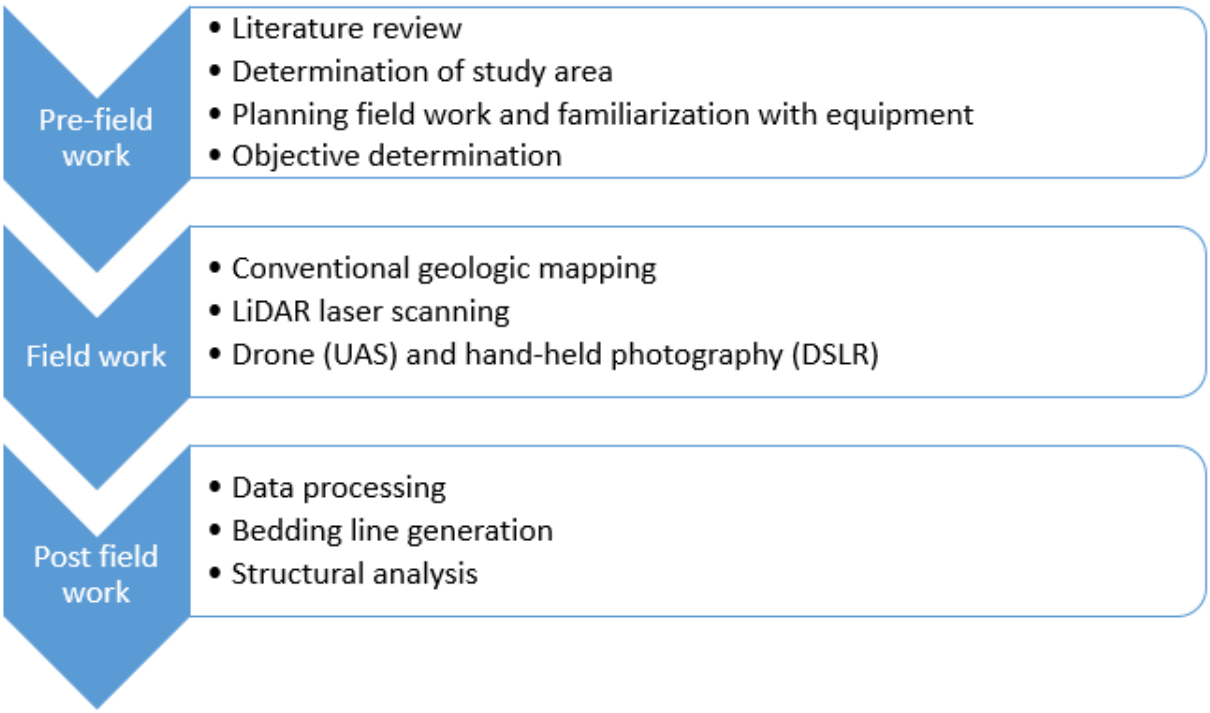


**Figure 3.1:** Workflow of the research including pre-field work, field work and post-field work sub-chapters and its main tasks.

## 3.2 Pre-Field work

Understanding research goals and identifying the knowledge gap for the study was crucial for the field work preparation. Preparation required an extensive literature review, field map creation and determination of the study areas. This preparation allowed for acquisition of general knowledge about the project, acknowledgements of existing work and identification of possible geological challenges. Thereafter, the objectives of the project were determined, and a field work plan was created to ensure efficient field data collection. Additionally, a review of LiDAR's technical and practical concepts was necessary prior to the field work. This included grasping the use of the scanning tool and understanding the technology behind it in order to achieve high resolution, high quality data. Simultaneously, the use of Unmanned Aerial Systems (UAS) and digital single-lens reflex (DSLR) cameras had to be mastered in preparation to obtain high quality images and data. The utilized UAS device was a DJI Mavic Pro drone model. Following the first field trip, the project plan was revised in accordance with areas where data were collected.

## 3.3 Field work

The field work focused on collecting field data in order to fulfill the project objectives. The focus of the field work was investigating half-graben growth geometries by collecting dip measurements, observing lateral and horizontal facies changes and changes in bed thicknesses along the outcrops. Structural geologic elements, lithological contacts and their relationships were noted in addition to captured photographs for all of the outcrops. The locations of geological contacts, photographs and field measurement locations were recorded using a hand-held Global Positioning System (GPS) device.

The main aim with field measurements was to serve as reference observations for all of the outcrops, in addition to supplement the outcrops with acquired LiDAR and photogrammetry data. The measurement data collected during the field work combined with LiDAR and photogrammetry data provides high-quality measurements of syn-rift packages with the additional possibility of quantitative structural analysis of the outcrop. Data acquisition was carried out using a conventional geologic compass for dip measurements; LiDAR RIEGL VZ-6000 3D terrestrial laser scanner for sedimentological and more precise measurement data acquisition; Drone and DSLR cameras for photographing the outcrops (Figure 3.2). The photographs were collected of all outcrops for the purpose of illustration and explanation of geological structures, data quality control, data referencing and outcrop 3D visualization. DSLR camera photographs were supplemented with drone images to achieve coverage of hardly accessible outcrops due to vegetation or extreme lateral height variations, utilized for 3D visualization of Monastery and Kefalari outcrops. The LiDAR scanning tool also photographed the scanned outcrops, allowing for remote field mapping and additional scan quality control.

Challenges encountered during the field work included acquiring correct viewing angle for dip measurements using the geological compass. Poor weather conditions (e.g., rain, fog or snow), vegetation, highly reflective surfaces, extreme temperatures and extreme distance had adverse effects on the LiDAR data. The combination of conventional mapping and LiDAR data collecting methods helps to overcome these challenges and provides an opportunity to quality control each type of data. LiDAR data is the primary data source for this research available for Lapanagoi, Roghi and Vrachni outcrops, providing high detail measurement information

with good area coverage. To ensure full outcrop data coverage, several scanning positions with particular acquisition range angles were required. LiDAR data acquisition is a time consuming method, restricted by maximum 2.5 km scanning range, requiring well outcropping sediments together with possible scanning locations nearby. The criteria for scanning locations was set as high-elevation areas with road access appearing less than 2.5 km away from the desired outcrops wall. Therefore, LiDAR data acquisition was carried out for best fit outcrops only. Once the study areas were defined, the field work plan was updated to acknowledge the present challenges by weighting the importance of each outcrop and the difficulty of the geological setting.


**Figure 3.2:** The image of LiDAR RIEGL VZ-6000 3D terrestrial laser scanner acquiring data of Lapanagoi outcrop.

## 3.4 Post-Field work

The acquired LiDAR scanning data was processed using the RiScan Pro software developed by RIEGL Laser Measurement Systems. The processing focused on eliminating vegetation and generating a high-quality point-cloud dataset. Following processing, the point-cloud data were transferred into the Petrel E&P (Schlumberger, 2018) software platform. The acquired point-cloud data integrated with Petrel software permits structural analysis of the bedding lines of the study area, to determine if the half-graben outcrops show clear growth geometries. The combination of LiDAR data with field mapping is a novel technique for accurate structural analysis, enabling additional data quality checks and the ability to overcome the challenges of using each method individually. In addition to using field mapping observations as quality controls for LiDAR, outcrops without LiDAR data were analyzed based on field mapping observations, photographs and literature. The photographs were utilized in photogrammetry software allowing 3D view of the outcrops lacking LiDAR data (e.g., Monastery and Kefalari). Finally, the results from study area were compared with the analogue areas in NCS in order to determine the likelihood of observing syn-rift packages lacking growth geometries.

## 3.5 Data Set

The most important objective of the field trips was measuring and mapping half-graben infill geometries while checking for the typical indications of syn-rift packages. Various data types were analyzed in contrast to each other in the purpose of error margin assessment for the different data types. The revised data were classified into three categories based on location, data quality and precision (Table 3.1):

1. Outcrops with field observations, photography, LiDAR and literature data;
2. Outcrops comprising field observations, photography and literature data;
3. Outcrops covered in literature only.

The studied outcrops were chosen for investigation based on best outcrops exposures, location near fault features and high preservation of outcrop geological structures and lithologies.

Eight outcrops were investigated from study areas A and B, yet, northern Peloponnese area exhibit potential for a minimum of two half-graben outcrop studies in addition, but the most of the half-graben features fitting the criteria have been investigated.

The focus of the study are the Lapanagoi, Roghi, Vrachni and Monastery Spileo (Monastery) outcrops from study area A (Figure 3.3), in addition to Kefalari East outcrop appearing in study area B. Figure 3.3 highlight outcrops containing high data quality with green color (Lapanagoi, Roghi and Vrachni) and Monastery outcrop lacking LiDAR data represent lower data quality and is, therefore, marked in bright red. The acquired data for various outcrops, resulting in various data quality and data types:

- Field acquired LiDAR data at Lapanagoi, Vrachni and Roghi study areas,
- Photographs collected during the field work at all eight outcrops of located at all study areas,
- Dip and dip-direction measurements collected using conventional geological compass during the field work at all study areas, and
- Field observations of unconformities, facies change and general structural fault details for all outcrops.

| | Data type | | |
|---|---|---|---|
| Outcrop | Field | LiDAR | Literature |
| *Lapanagoi* | X | X | X |
| *Roghi* | X | X | X |
| *Vrachni* | X | X | X |
| *Kefalari East* | X | | X |
| *Monastery* | X | | X |
| *Kefalari West* | X | | X |
| *Kyllini* | X | | X |
| *Roghi West* | X | | X |


**Table 3.1:** Data quality rating of the outcrops based on the available data type. The data quality of outcrops are color coded: high data quality - in green and low data quality - in red. The outcrop locations are displayed in Figure 3.3.

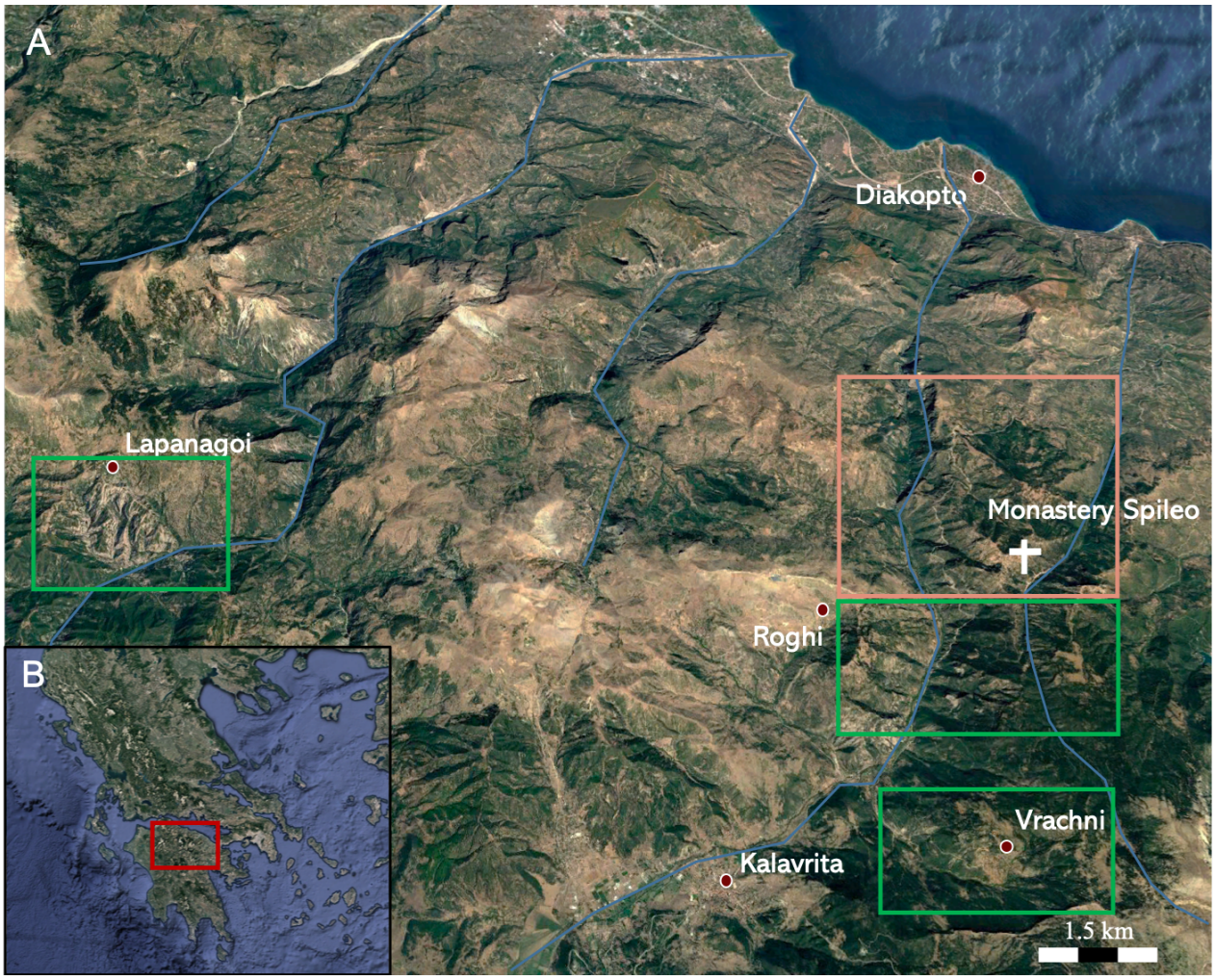


**Figure 3.3:** Map illustrating location of the outcrops. Figure B is an inset map indicating location of Figure A. The outcrop areas are marked with green boxes - indicating high data quality and red boxes - indicating lower data quality, in reference to the Table 3.1. Transverse faults are interpreted according to the final result of Egeland 2018 and are highlighted in blue color. The background maps are retrieved from Google Earth Pro.

## 3.6 Software

Various software were used in data processing and interpretation steps (Table 3.2). The purpose of the majority software use were LiDAR data handling. The processing of the acquired LiDAR point-cloud and bedding line generation was carried out using RIEGL RiScan Pro software. The intended use of Lime software is 3D data visualization and interpretation, which was used for generated bedding line export as a file type compatible with Petrel software. The conventional use of Petrel is within exploration and production sector in petroleum exploration industry, utilized in the project as bedding line modification medium in order to create equal bedding

line point nodes and export the resultant values. The achieved numerical values were inputted into Microsoft Office Excel and MathWorks Matlab software with the purpose of bedding line plot creation, necessary for the structural analysis. The general use of Excel software consist of various calculations utilizing spreadsheets, graphing tools and tables creation. The photogrammetry step was carried out utilizing Agisoft PhotoScan program for photograph assemblage, point-cloud creation and visualization. Additionally, point-clouds were visualized in Cloud Compare software, which also allows point-cloud and mesh processing.

| Software | Generally used for | Utilized for |
|---|---|---|
| Agisoft PhotoScan (Agisoft LLC) | Photogrammetry data assembling, processing and interpretation | Photogrammetry software for 3D point-cloud creation and processing from photographs |
| Cloud Compare (Electricity of France) | 3D point-cloud and mesh processing | Additional software for point-cloud visualization in 3D |
| Excel (Microsoft Office) | Calculation, graphing tools and tables creation | Bedding line data processing and structural analysis plot creation |
| Lime (Simon Buckley) | 3D data visualization and interpretation | Bedding line export as ASCII file |
| Matlab (MathWorks) | Programming, script writing, graphics, analysis and software developing | Bedding line data processing and structural analysis plot creation |
| Petrel E&P (Schlumberger) | Seismic data interpretation, 3D modelling, reservoir model building, simulations, volume calculation, map production and etc. | Equal node creation for bedding lines and XYZ value export |
| RiScan Pro (RIEGL) | 3D laser data processing, visualization and interpretation | LiDAR data processing and bedding line generation |

**Table 3.2:** A table representing various software purposes utilized for this research.

## 3.7 LiDAR Theory

The most novel data type used for this research is the LiDAR data, which is a Terrestrial Laser Scanning (TLS) technique often used for geological and geotechnical field investigations. The emerging technology of TLS is an established and efficient technique for a full outcrop's scan used for quantitative structural analysis and prediction beyond single bedding surfaces in this project. It is more rapid than traditional field techniques, allowing to measure inaccessible out-

crops to compass measurements, producing high resolution data in both vertical and horizontal directions (Laux and Henk 2015). The LiDAR instrument measures light ranges in the form of a scanning pulsed laser (**ParseliunasE.2015**). The emitted powerful light pulse is reflected back to the scanner once the pulse interacts with an object, followed by scanner calculations based on the travel time of the light pulse (ibid.). Each reflection point of the laser pulse are interpreted as spatial coordinates. Utilizing the reflection data, the terrestrial scanner creates an array of data points, referred to as a point-cloud, allowing integration of scans from several localities to describe a single outcrop. Additionally, the scanner includes an inbuilt calibrated camera, which provides photographs of the scanned locations. The photographs contain the Red Green Blue (RGB) filter information which is incorporated into the point-cloud generation for data points coloring. Thus, high data-density LiDAR scanner provides 3D information about surface characteristics and provides a unique opportunity for a high resolution structural analysis and imaging of the outcrops. The reflection points of the laser rely on the accuracy of inbuilt system components - the GPS and Inertial Measurement Unit (IMU) and is critical for quantitative structural analysis (Chen 2017).

## 3.8 LiDAR Data Processing

The acquired LiDAR data must be processed prior to interpretation. Several different processing techniques were utilized in order to achieve the highest data quality and best results. The LiDAR data processing is a lengthy step which required 6 weeks in total. The processing can be subdivided into three main steps of octree generation and mesh creation followed by a few additional steps including bedding line creation. A general workflow was created to provide a guideline for processing (Figure 3.4). The workflow and supplementary parameters for the best processing workflow so far are described in the following sub-chapters.

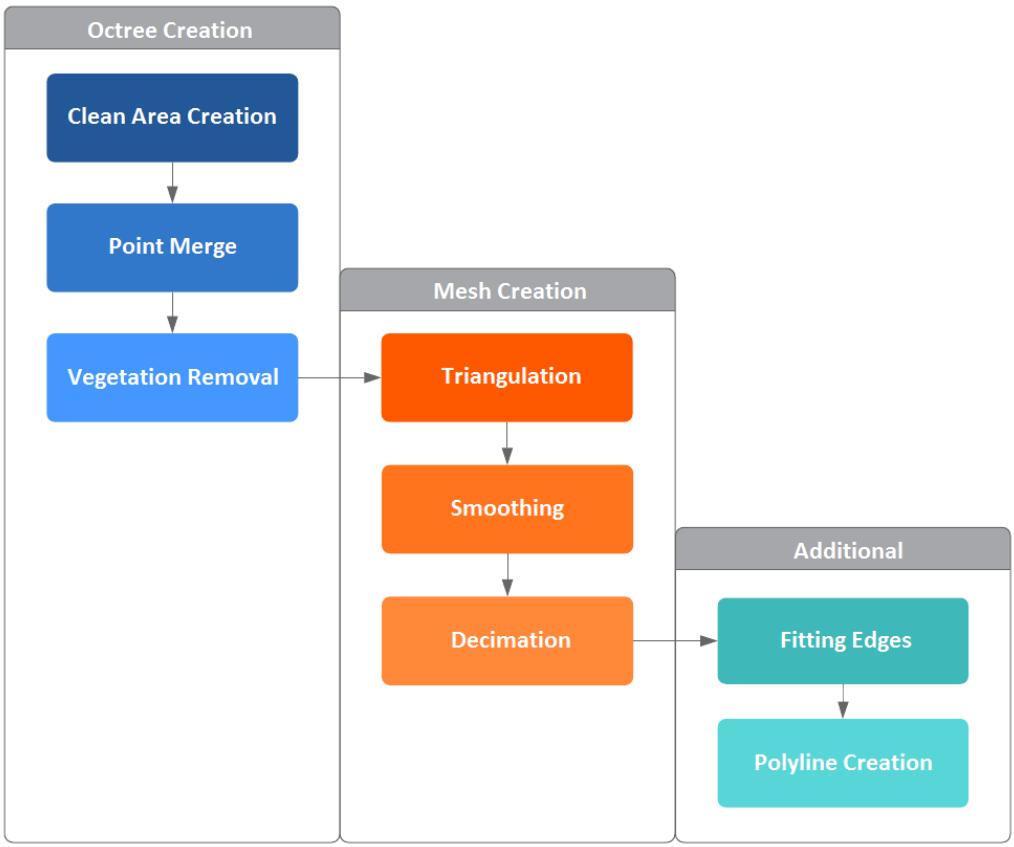


**Figure 3.4:** Workflow representing the steps in LiDAR data's processing.

### 3.8.1 Point-Cloud Processing

The processing of the point-cloud is an essential step for the LiDAR data processing, where the quality of the final point-cloud determines the quality of the structural analysis. The initial step of geo-referencing was completed prior to the point-cloud processing with help from the UiS staff. Point-cloud processing was carried out in Riegel RiScan Pro software, completed in 4 weeks. The processing was prolonged time-wise due to the encountered errors discussed in the Processing Errors 3.8.2 section. The steps of the point-cloud processing are explained as follows:

- The first phase of data processing consisted of octree creation with the purpose of generating a homogeneous point-cloud to make the meshed data cleaner and more manageable. The octree was generated from the point-cloud using an X and Y increment of 0.3 meters and Z increment of 0.1 meters. Furthermore, cells containing only 1 point were isolated out.

- The creation of a clean point-cloud was executed using point merging which evens out the points in the cloud by removing dense data areas. Points appearing closer than 10% of the chosen increment were merged.

- Point merge was followed by data filtering; in this case a partial vegetation removal terrain filter was applied. The vegetation removal runs along the X-Y plane and removes vegetation automatically, with an option for manual changes.

- The second phase of processing was the mesh creation, which consists of triangulation, smoothing and point-cloud decimation steps.

- The triangulation creates a polygonal surface from the point-cloud by generating compact triangles from the data points. Partial plane triangulation was operated using a minimum triangle angle of 10°, tilt angle edge length of 80° and a maximum triangle edge length of 30 meters, as suggested by Setkowicz 2014. Different values for triangulation parameters were tested (listed in sub-chapter 3.8.2). Improper parameters resulted in needle-like triangles.

- The smoothing step smooths the triangles created during the triangulation step, increasing display quality of the model and producing an easier manageable point-cloud. Smoothing was carried out using windowed sync smoothing, with a pass band parameter of 0.086 as suggested by Riegel RiScan Pro software's manual. This was followed by a Laplacian smoothing operation, applying 200 iterations for the dataset with the activated feature edge smoothing feature and a feature angle of 30°.

- The decimation step reduces the number of triangles in the final mesh. A target reduction rate of 0.7 was used. This relatively low reduction rate was applied for the sake of preserving the majority of the data points and producing a high-quality mesh.

- The processing was followed by bedding line interpretation and generation.

### 3.8.2 Processing Errors

Three main pursuing errors occurred during the processing steps of filtering, triangulation and decimation. The errors occurred due to the improper processing values applied or due to the incorrect automated processing step performance. However, the most preferable workflow for point-cloud data processing was carried out as described in the previous section.

1. The first error encountered during point-cloud processing was caused by the vegetation removal terrain filter, which resulted in an unwanted outcome. Part of the outcrop data have been removed along with the vegetation. The partial removal of outcrop was due to the small bushes and grass, appearing very close to the outcrop, making it nearly impossible for RiScan software to differentiate between sediments and vegetation (Figure 3.5). In the workflow, the removal filter step was skipped in order to avoid this error and preserve valuable geological data.

2. Filtering step was followed by triangulation, which resulted in another issue due to the incorrect triangulation parameters. Triangulation using a minimum triangle angle of 0°, tilt angle edge length of 90° and maximum triangle edge length of 50 meters resulted in peaks and several needle-like triangles. Six different sets of parameter values were tested until an acceptable triangulation result was achieved (Figure 3.3). Additionally, partial triangulation was required, rather than whole outcrop triangulation at once, due to the RiScan Pro program crashing as a result of extensive processing requirements and data overload.

3. Another error appeared during the decimation process, which was caused by the use of an improper reduction value (target reduction value of 5). This error resulted in low point-cloud data quality. The decimation process issue was resolved by testing out different parameters for decimation rate and feature angle. Once the mesh creation was completed, the bedding line generation followed.

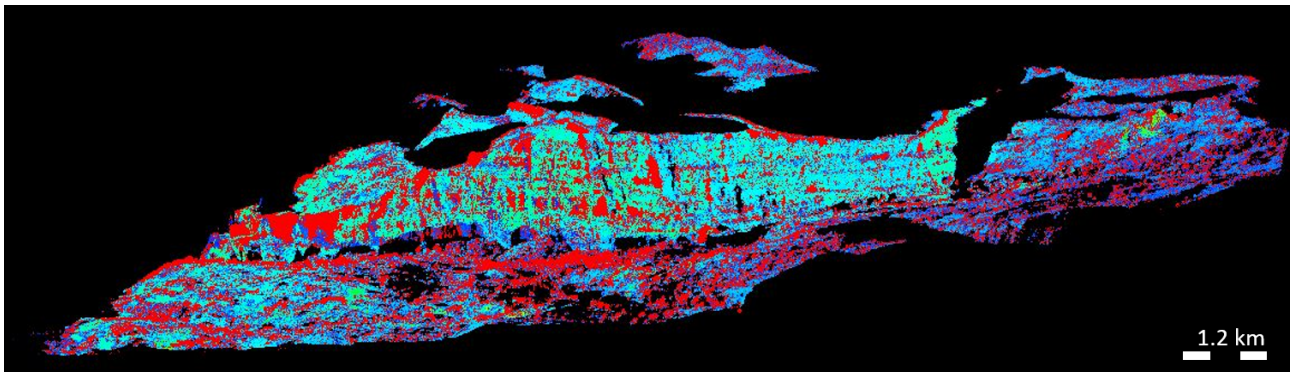


**Figure 3.5:** Example illustrating Vegetation Removal filter application on Lapanagoi outcrop in RiScan Pro software. The filtered areas are marked in red, which include both the unwanted vegetation and parts of outcrops sediments removal.

| | | | | | | |
|---|---|---|---|---|---|---|
| Max Triangle Edgelength (m) | 50 | 10 | 20 | 30 | 30 | 20 |
| Tilt Angle (degrees) | 90 | 10 | 20 | 80 | 80 | 50 |
| Min. Triangle Angle (degrees) | 0 | 0 | 0 | 10 | 0 | 10 |

**Table 3.3:** Table representing the tested triangulation process parameters resulting in errors and inaccurate point-cloud.

## 3.9 Photogrammetry Data Processing

Photogrammetry allows 3D virtual outcrop view by combining field acquired photography data and producing a point-cloud. The photogrammetry processing was carried out using Agisoft PhotoScan software. The resultant point-cloud was utilized as a supplementary data for the generation of bedding lines for structural analysis.

- The selected photographs were imported into the Agisoft PhotoScan software, reviewed and arranged in the initial photograph acquisition order. In total, 12 markers were added per outcrop in order to create more accurate results. The software uses markers as accurate common data points when merging the photographs, which helps the software to find the position of camera and refine parameters of camera calibration. Processing was carried out using highest quality option throughout the steps.

- The imported and properly arranged photographs were firstly aligned using high accuracy, but disabled pair pre-selection.

- The aligned photographs were further used for high quality dense cloud building. The dense cloud is based on the imported pictures and camera positions.

- Dense cloud was used as a source data for mesh creation. High face count and arbitrary surface type were chosen. The arbitrary method is applicable for all kind of objects, in the contrast to the height field method which is best for planar type surfaces only. The resultant mesh displayed a few spots lacking data appearing not on the outcrop surface and, therefore, mesh editing was not necessary.

- Thereafter, texture was built using default texture size in addition to generic mapping and mosaic blend mode, which blends several frequency domains independently using the weighted average value calculated from all picture's pixels.

- Followed by a tiled model built using the suggested reconstruction parameters by software. The suggested parameters are automatically estimated pixel sizes in relation to imported pictures.

- Lastly, orthomosaic was generated for creation and visualization of the final point-cloud of the outcrop.

## 3.10 Data Interpretation

In order to analyze the outcrops for growth geometries, individual beds interpretion was needed, so that bed thickness and dip could be analyzed. Interpretation can be carried out using RiScan Pro software for outcrops comprising LiDAR data, and Petrel for outcrops consisting of field and photograph data. Bedding line generation in Petrel software was a straightforward step, supplemented with photogrammetry data, although, bedding line generation with RiScan Pro software was more complex. RiScan Pro includes two available options of automated and manual bedding line interpretation. Automated bedding line generation in RiScan Pro was not applicable due to the lack of sharp edges bounding sedimentary layers of interest in the outcrops. Therefore, bedding lines were created manually, which produced acceptable results. The manually generated bedding lines were imported into Lime software in order to export

bedding line values as an American Standard Code for Information Interchange (ASCII) file, compatible with Petrel software. The imported values into Petrel software were edited, quality controlled and exported as points used for structural analysis plot creation.

### 3.10.1 RiScan Pro Bedding Line Generation

Automated bedding line generation in RiScan Pro is a time-consuming process, which required two weeks to produce high-quality data with minimal errors for all three LiDAR data containing outcrops. Minor bedding line interpretation errors might occur due to the misinterpretation of erosional surfaces. The executed bedding plane creation step was followed by the line export. Generated bedding lines were imported into Petrel Software in order to edit the nodes and visually quality control the final bedding data. Transferring bedding lines from RiScan Pro into Petrel Software platform encountered several errors. The workflow for bedding line generation is described as follows:

- The generation of the bedding lines was carried out using manual "polyline creation" mode in RiScan Pro software picking the representative point-cloud points of one stratigraphic layer at a time creating a high quality data (Figure 3.6).
- General bedding line import into Petrel Software was necessary for further data interpretation. The import process required various steps and the utilization of three different computer programs (Figure 3.7).
- The foremost step involved import of the final RiScan Pro project into Lime software. The Lime software allowed conversion of the imported bedding lines to ASCII file type. Lime was utilized as a file type conversion tool due to the incompatible ASCII file formats between RiScan Pro and Petrel software.
- The final ASCII bedding line data file was imported into Petrel as general lines/points. Bedding lines were imported as separate lines, and subsequently meshed into one file for the purpose of line editing and node connecting.
- A workflow created in Petrel was used for appending the polygons and combining the

separate lines into a single file. The creation of the workflow is the most efficient way for polygon appending and merging.

- The main goal with the bedding line editing was to achieve extended lines representing continuous stratigraphic horizons along the outcrop.

- Following the bedding line connection step, node intervals were equalized using an interval of 5 meters. Equal node intervals are important for the subsequent interpretation and additional bedding data processing.

- The generated bedding lines were exported as a spreadsheet into Microsoft Office Excel and Matlab software for structural analysis of thickness and dip changes along the sedimentary surfaces.

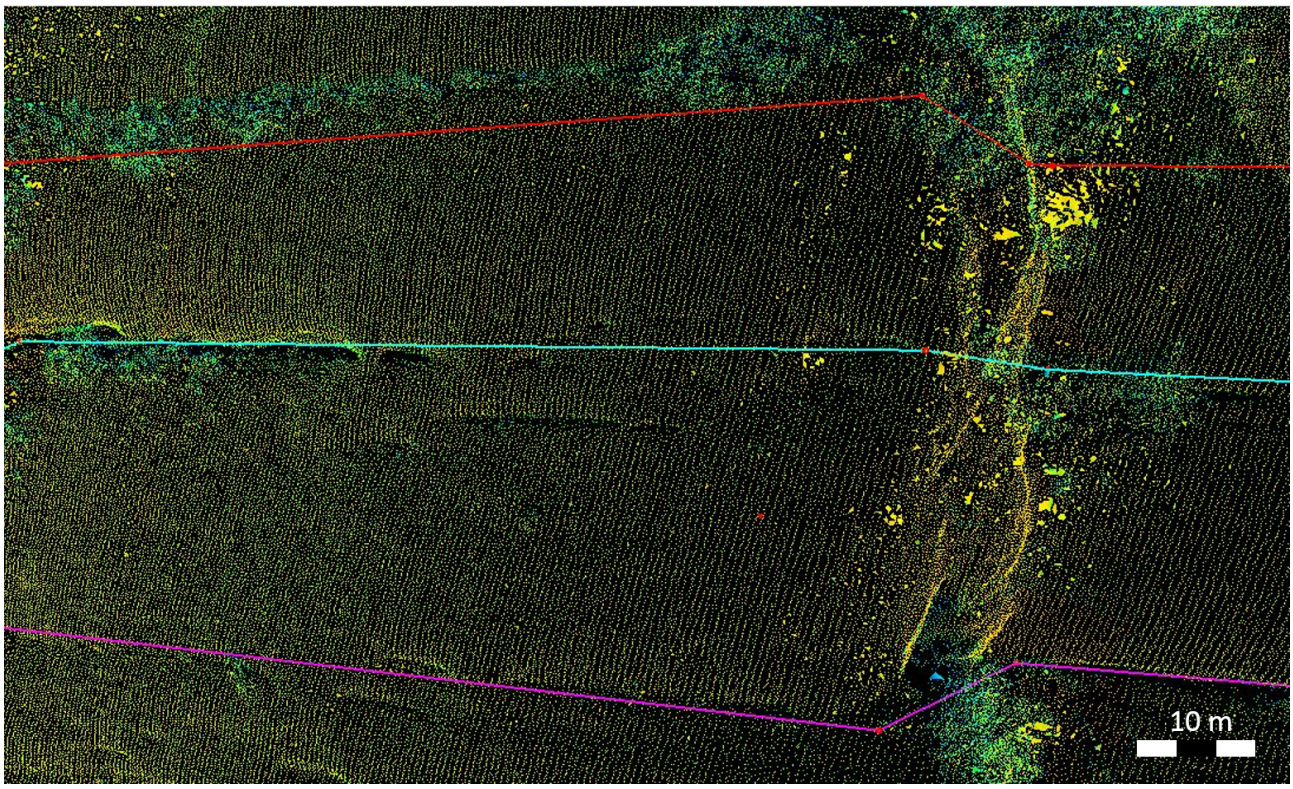


**Figure 3.6:** Example of three bedding line traces along the point-cloud from Lapanagoi outcrop using RiScan Pro software by picking raw point-cloud points resulting in high data quality.

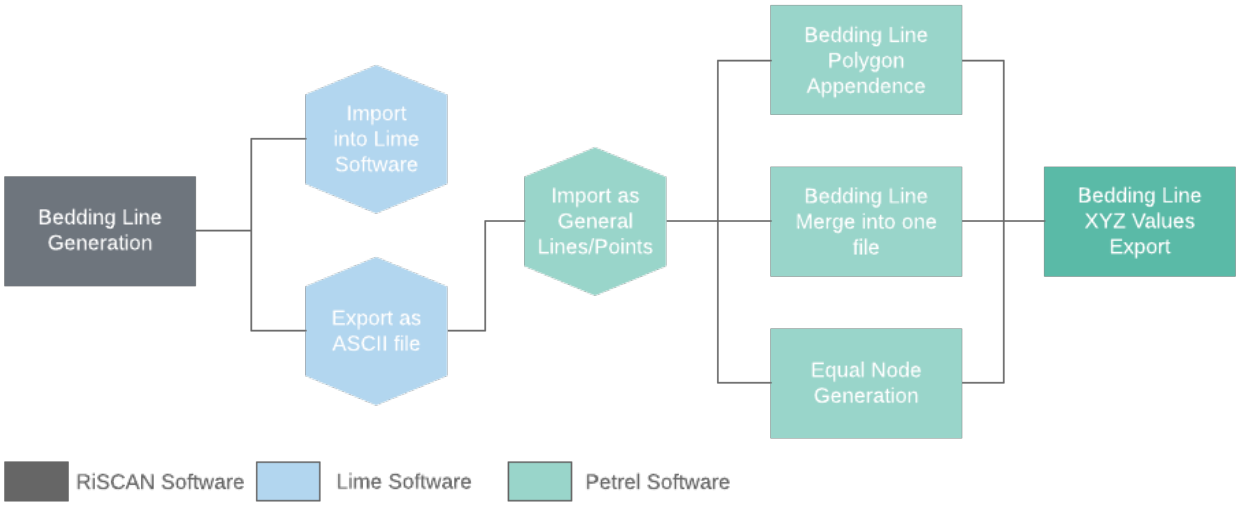


**Figure 3.7:** Workflow chart portraying steps in bedding line processing. The steps are color coded depending on the software used.

### 3.10.2 Petrel Bedding Line Generation

Bedding line generation for the outcrops comprising of field, photography and literature data (Monastery and Kefalari) was carried out in 3 days utilizing Petrel software. This approach is less time consuming and provides relatively good data quality in comparison to LiDAR data bedding line generation using RiScan Pro software. In order to quality control the data and increase its quality, the bedding line generation was supplemented with photogrammetry, allowing to view the outcrop in 3D.

- Foremost step was carried out in the field, where outcrops were photographed in detail.
- The field acquired images were merged into one panorama image accompanied by an automatic view distortion removal, in order to display the most correct view of the outcrop. The photographs were edited and merged using Adobe Photoshop software. Additionally, field data was supplemented with photographs that were used to create a point-cloud allowing 3D display of the outcrop.
- The images were input into Petrel software as a bitmap image file.
- Thereafter, the image was geo-referenced by assigning independent coordinates to all corners of the image. Geographic coordinates were retrieved from Google Earth software and

were not compatible with Petrel, therefore, geographic coordinates had to be transformed into the Cartesian Petrel coordinates.

- The transformation was carried out utilizing GIS ArcCatalog software, where geographic coordinates were exported as a shape file. The shape file inputted in Petrel provided a spreadsheet with corresponding Cartesian coordinates.
- Geo-referencing of the image was followed by bedding line generation, utilizing the polygon editing tools in Petrel. Each bedding surface was traced along the image creating continuous bedding lines.
- The bedding lines were merged into one file for each outcrop using previously created workflow for bedding line appending and editing.
- Merged bedding line nodes were equalized, using a 5 m interval.
- Finally, the generated numerical values of bedding lines were exported for the structural analysis plots creation.

## 3.11 Bedding Line Analysis

Bedding line analysis was carried out via two approaches utilizing Microsoft Office Excel and MathWorks Matlab software. The use of different approaches allows for additional data control, comparison of software and different procedures. Matlab and Excel software were used to create bedding line plots later used for structural and statistical analyses. The creation of plots focused on illustrating the presence or lack of typical growth strata characteristics. Three main plots were created for each outcrop with data plotted relative to the bounding fault: 1) a plot representing horizontal and vertical bedding line variations; 2) a plot displaying the thickness variations of each bed by plotting horizontal distances vs. thickness values; and 3) a plot illustrating variations in dip of each bedding line, plotting horizontal distances vs dip values.

The two approaches applied vary primarily in their complexity. In Excel, the bedding lines were treated as having only analyzed using two dimensions, horizontal and vertical (X and Z). In Matlab, the X and Y coordinates of bedding line nodes were considered together to more

accurately determine the distance along the outcrop surface, which was plotted against the vertical coordinates. In addition to this difference, different smoothing procedures were applied in Excel and Matlab.

### 3.11.1 Excel Analysis

The first bedding line analysis approach was completed in Excel software, which is a lengthy step requiring 2-3 weeks of work. The numerical values of generated bedding lines were imported into the software and modified. First, bedding line values were calculated in order to be displayed relative to the coordinates of the fault's position ($F_x$). Coordinates of each bedding line node were calculated relative to the fault's position by subtracting each of the bedding line node X-values (Series $X_s$) from the interpreted X-Value of the fault's position ($X_f$), described by equation (3.5). The ($X_s$) values were determined manually for each outcrop based on the interpreted locations of the bounding faults.

$$F_x = X_f - X_s \tag{3.1}$$

### 3.11.2 Bedding Line Plot

The bedding line plot allows for data quality control and visual investigation of bedding line length, thickness and dip changes. The bedding line plot was created by plotting representative bedding line node X and Z values against each other. X and Z values were exponentially smoothed in the interest of diminishing the distortion caused by the irregular outcrop's wall due to the recent erosion (Figure 3.8) which generates X and Z value fluctuations and incorrect bedding line peaks in the plot (Figure 3.9). The resultant line fluctuations serve as an undesired noise in the data, causing difficulty for statistical analysis and interpretation of bedding line results. Exponential smoothing normalizes the bedding line data and allows a detailed result examination by removing the irregular peaks and troughs (Figure 3.10). Exponential smoothing is a technique designed for smoothing data belonging to a series. The additive exponential smoothing technique assigns exponentially decreasing weights over the series in contrast to the other general smoothing techniques which weight observations equally (Figure 3.11) (Hyndman

et al. 2008). Exponential smoothing was performed using the Data Analysis Toolpak in Excel program applying the formula (3.2),

$$S_t = \alpha \times X_n + (1 - \alpha) \times S_{t-1} \tag{3.2}$$

where $(\alpha)$ represents a smoothing factor, $(X_n)$ is the non-smoothed X, Y or Z numerical values and $(S_{t-1})$ serve as previously smoothed statistic value. A smoothing factor of 0.1 was found to give optimum results.

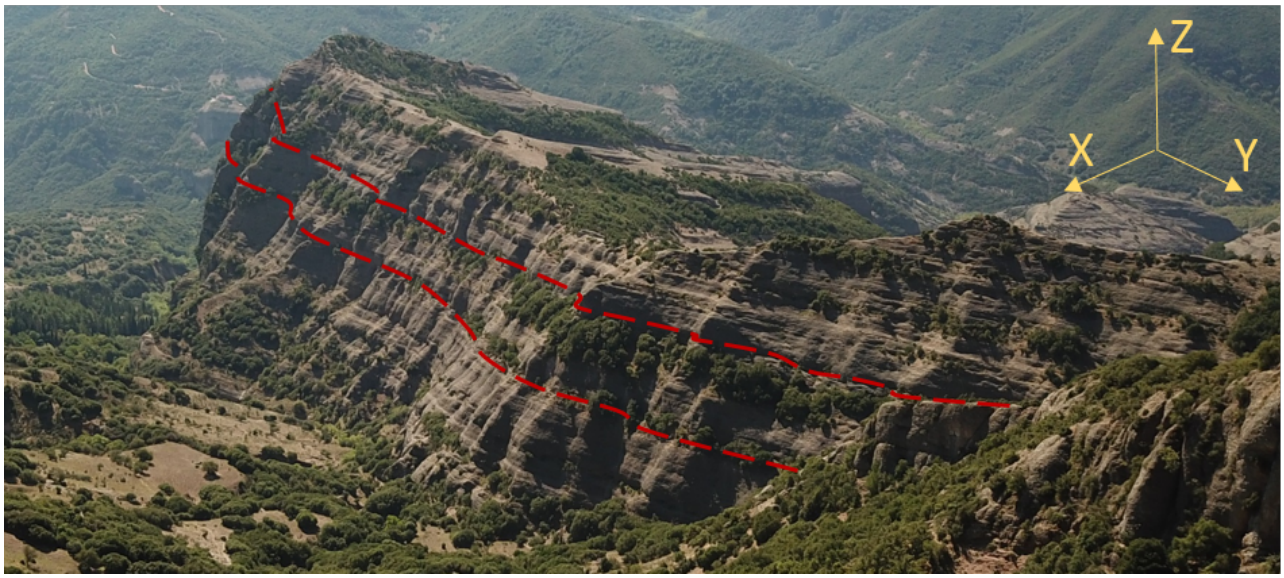


**Figure 3.8:** Illustration of unevenly eroded outcrop wall causing fluctuations of bedding line X and Z values in 2D. The irregularities of the outcrop are highlighted in red on the Lapanagoi outcrop.

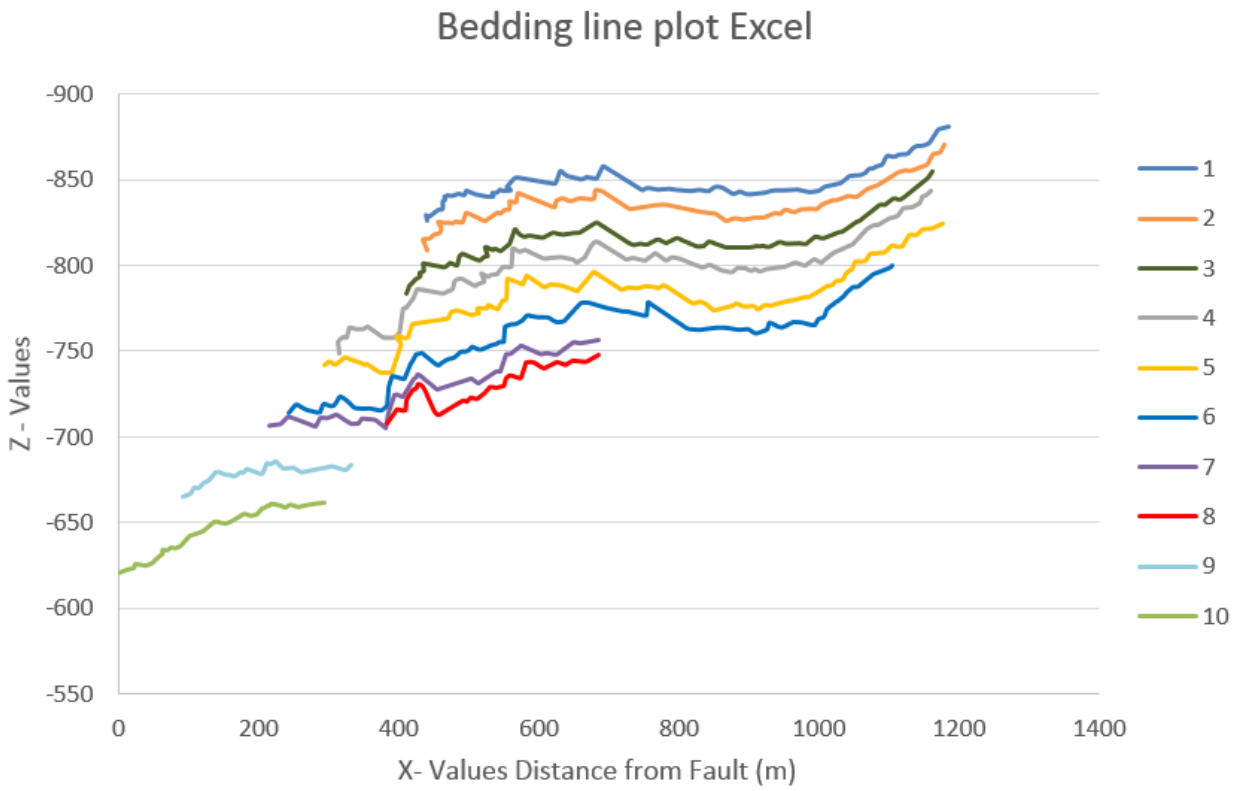


**Figure 3.9:** Raw bedding line plot displaying bedding lines affected by fluctuations. The plot displays unsmoothed $F_x$and Z values. The bedding line are color-coded.

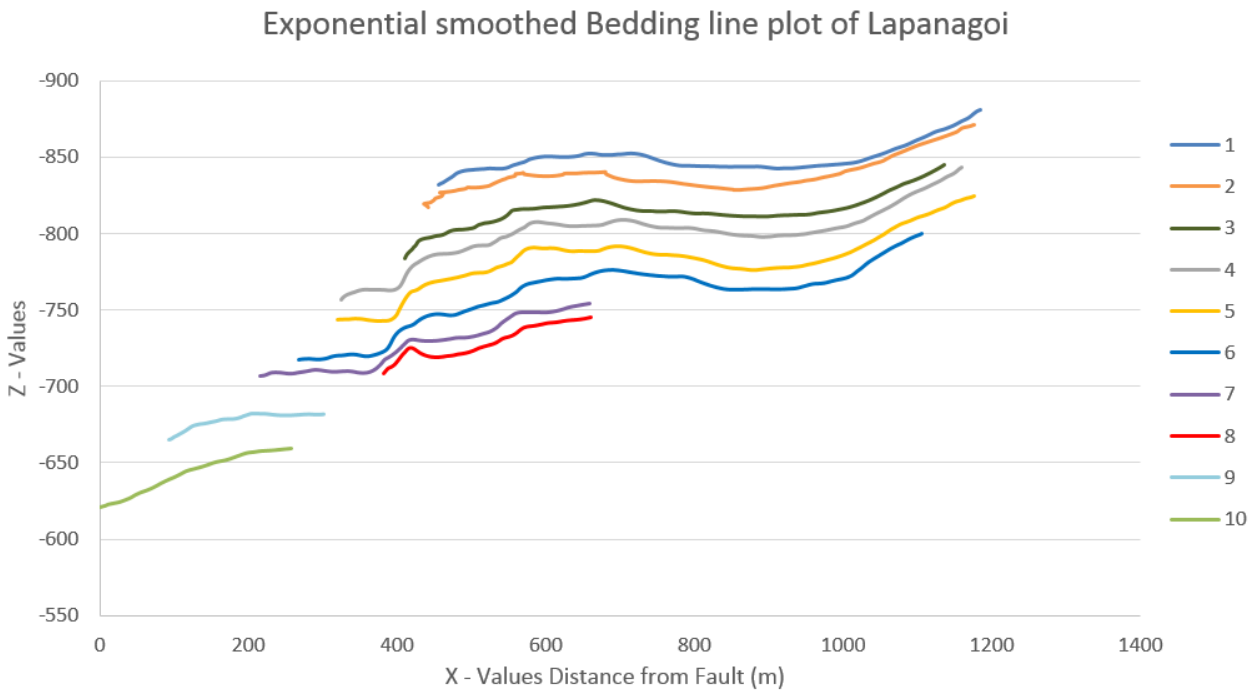


**Figure 3.10:** Bedding line plots displaying the reduction of data fluctuations following exponential smoothing. Exponentially smoothed Z- and $F_x$- values are plotted as Y- and X-axes respectively

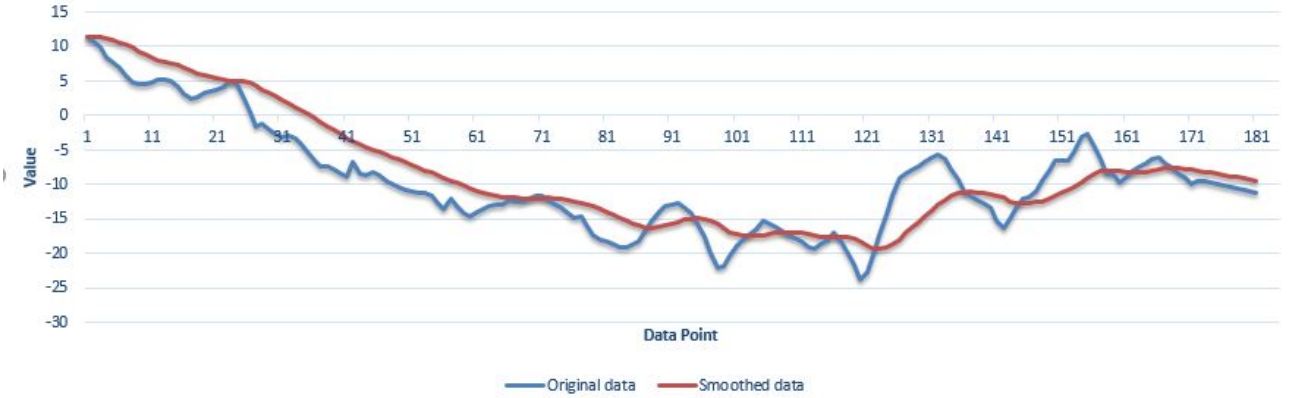


**Figure 3.11:** Illustration of exponential smoothing effect on one bedding line. The original line data is displayed in blue, while the smoothed data is displayed in red. Exponential smoothing evens out fluctuations in the original data using data by applying smoothing along the bedding line.

### 3.11.3 Thickness Plot

Thickness plots changes will be observed in relation to an adjacent fault and provide evidence of growth geometries. The bed thickness (T) was calculated by taking the difference of Z values between two bedding lines defining a single bed underlaying ($P_u$) and overlaying ($P_o$) (Equation 3.3). An important step is to ensure that the X values of the points being compared line up.

$$T = P_u - P_o \tag{3.3}$$

Bedding lines comprise of irregularly spaced points, producing false thickness values if not corrected. Therefore, bedding line data points were interpolated for the purpose of achieving equal point increments (Figure 3.12). Interpolation of the bedding line points evens out the increment between nodes yet still generating precise results. The interpolation was carried out using the Excel software executed by two bedding line datasets input that were used to create constant spacing and pairing of bedding line points. In order to achieve best results, underlying lines were interpolated with the overlaying ones.

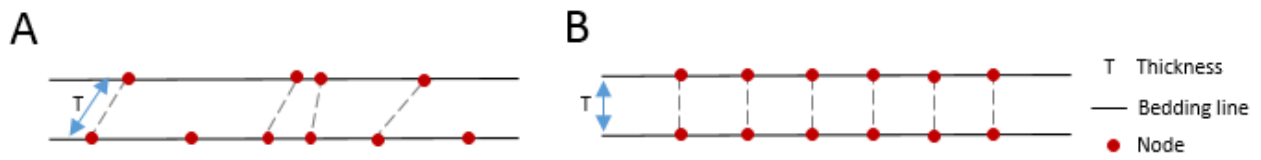


**Figure 3.12:** Graphic illustration of interpolation importance for thickness calculations of sedimentary beds represented by irregular bedding lines. Figure A displays the incorrect thickness values achieved by irregular node increment; Figure B represents interpolated nodes with regular intervals resulting in correct thickness values.

### Thickness Plot Errors

Early interpolation attempts resulted in a few data inaccuracies. Interpolated data results for bedding lines were generated plotting interpolated X values against the interpolated thickness values. In order to quality control interpolation results, the interpolated bedding line plot was compared with the previously generated, non-interpolated plot. The comparison of two plots resulted in the misplacement of several bedding lines. In Figure 3.13, bedding lines 2, 4 and 5 were misplaced, while bedding lines 6 and 7 were overlapping with 5. This error was corrected by interpolating underlaying bedding lines with the overlaying ones, except bedding lines 11 and 12 which were interpolated with each other (Figure 3.14). The interpolation of bedding lines 8 and 12 caused errors due to the dissimilar line shapes and absence of overlap. Additionally, slight errors occurred interpolating partly overlapping bedding lines. This was corrected by interpolation of underlaying lines with previously interpolated values of overlaying bedding lines.

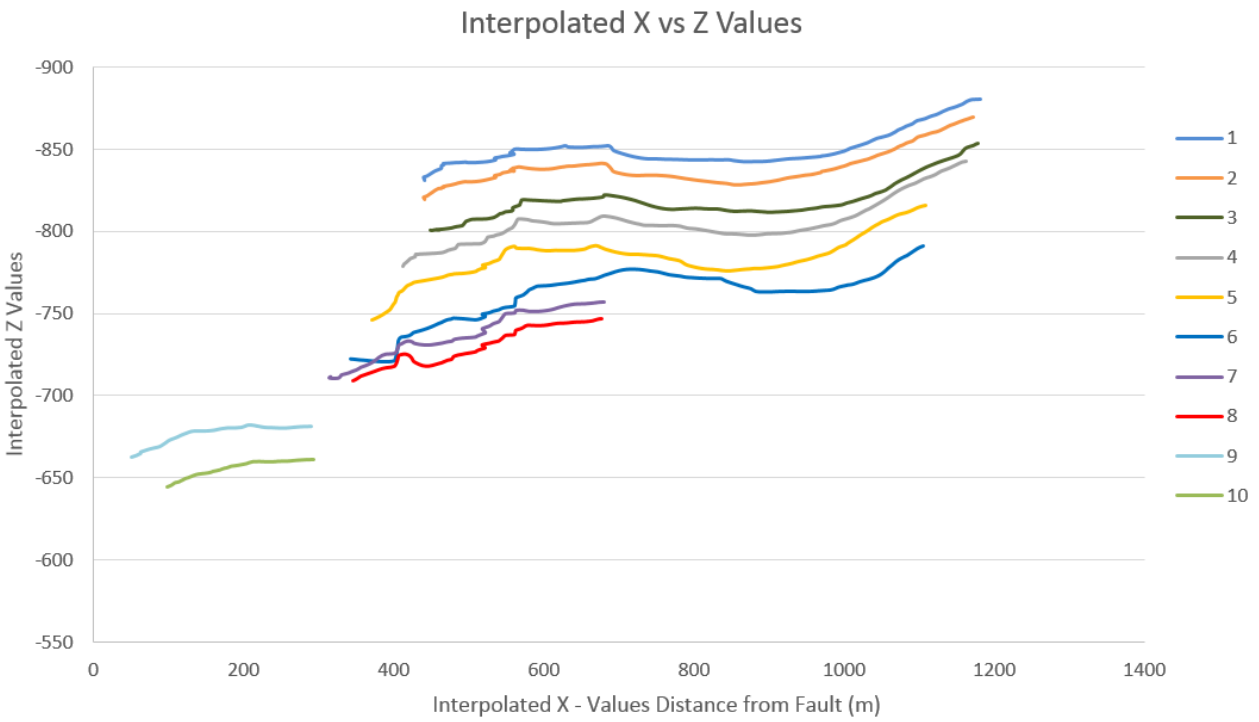


**Figure 3.13:** Plot representing errors encountered during bedding line interpolation. Plot A displays the first interpolation attempt, which resulted in several misplaced bedding lines. The plotted X-values are relative to the faults location. Bedding lines are color-coded.

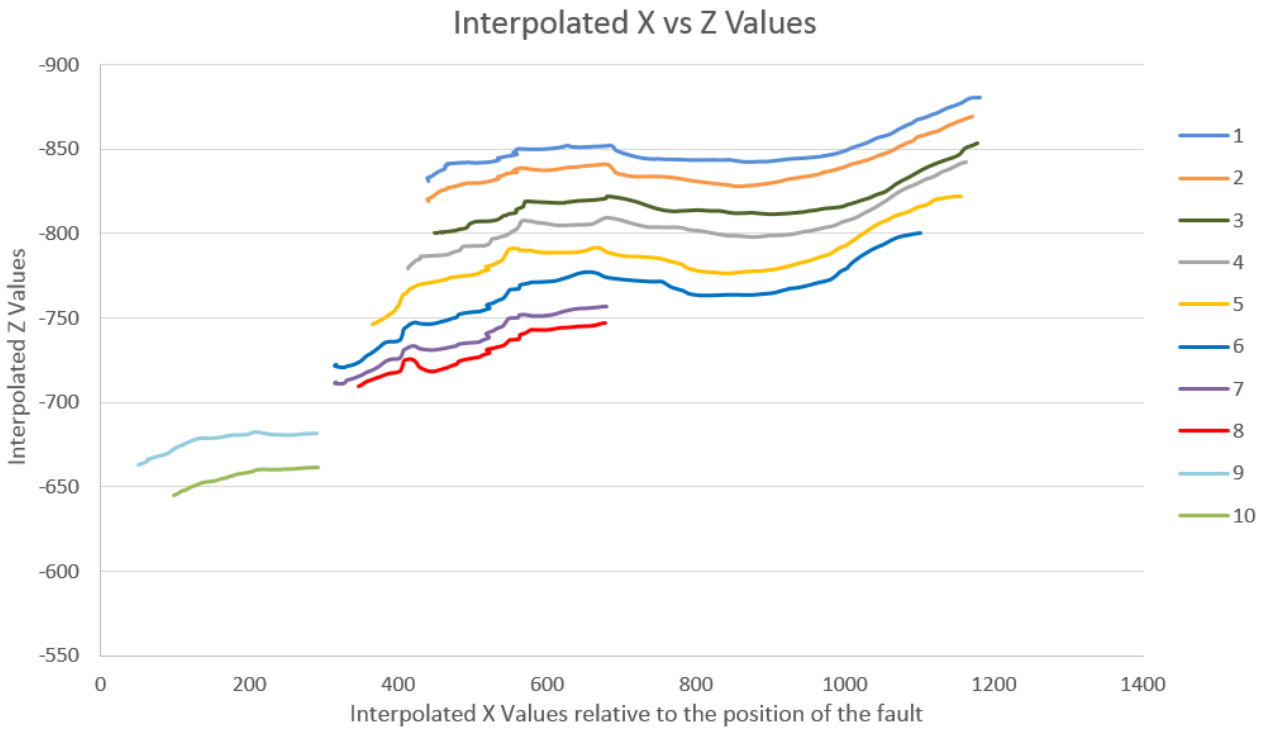


**Figure 3.14:** Plot representing the final interpolation of bedding lines, after correction for errors seen in Figure 3.13. The X-axis displays interpolated X-values relative to the fault's location; Y-axis display interpolated Z- values. Bedding line are color-coded.

### 3.11.4 Dip Plot

The main goal for creation of the dip plots, was to visualize variations in bedding line's dip values in order to assess growth strata geometry existence. First, dip values were calculated using trigonometry to estimate the dip angle ($\theta$) using equation 3.4,

$$\theta = tan^{-1}(\frac{Z_2 - Z_1}{X_2 - X_1}) \tag{3.4}$$

where $\theta$ is computed by calculating inverse tangent value ($tan^{-1}$) for the difference between Z values ($Z_2 - Z_1$), divided by differences between X values ($X_2 - X_1$) (Figure 3.15). Dip of a bedding line in an outcrop can be computed in this way by using distance measured laterally and vertically along the outcrop as X and Z values in equation 3.4, respectively. Initially, the dip values were calculated directly from the raw X and Z bedding line data. This initial dip plot was unsuitable for structural analysis due to severe bedding line dip value fluctuations generating excessive dip data trends due to the very fine data resolution and noise (Figure 3.16). In order to reduce the large peaks and troughs, exponentially smoothed values were used for dip calculations and plotted thereafter. The exponentially smoothed values resulted in significantly smoother values, whilst keeping the general data trends (Figure 3.17). Nonetheless, exponentially smoothed dip plot still required further improvements in order to display dip data trends more evidently for structural analysis. Therefore, additional dip calculation approach was tested out, calculating dip values using various intervals (3, 5, 10, 15, 20, 25, 30 and 50). These results were plotted for evaluation. The evaluation criteria were defined as smooth dip appearance and preservation of the original data trends. Increments lower than 15 resulted in near-recreation of original bedding line; dip values greater than 20 were highly smoothed with general trends removed (Figure 3.18). Dip value intervals of 15 and 20 gave good indicators of the dip data trends. Increment of 15 was determined to be the most appropriate, displaying slight peaks and troughs in addition to a modest value adjustment compared to the original dip data.

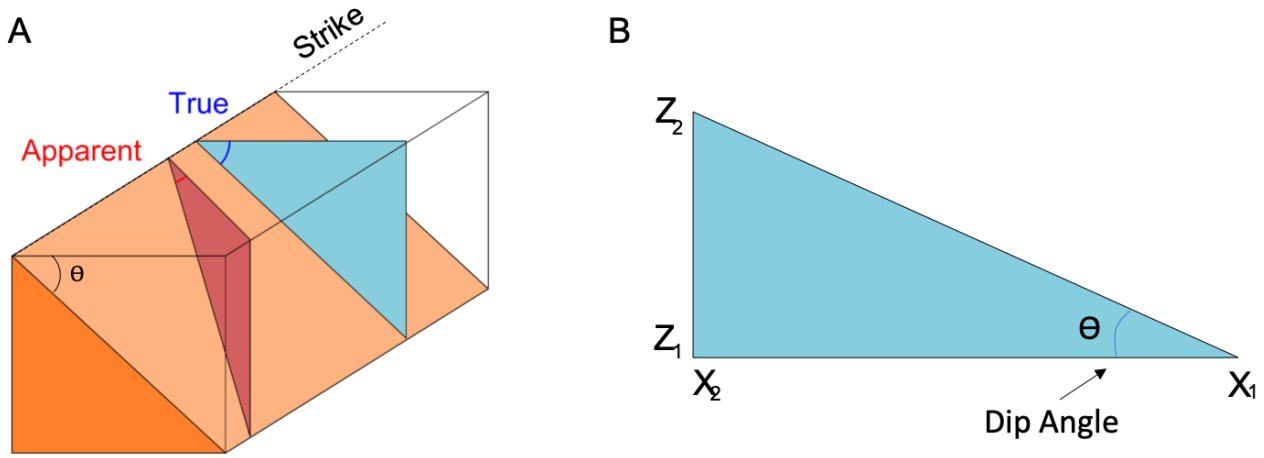


**Figure 3.15:** Schematic illustration of apparent and true dip angles. Red triangle represents apparent dip; Blue triangle - true dip. Figure B represents X and Z values used for true dip calculations.

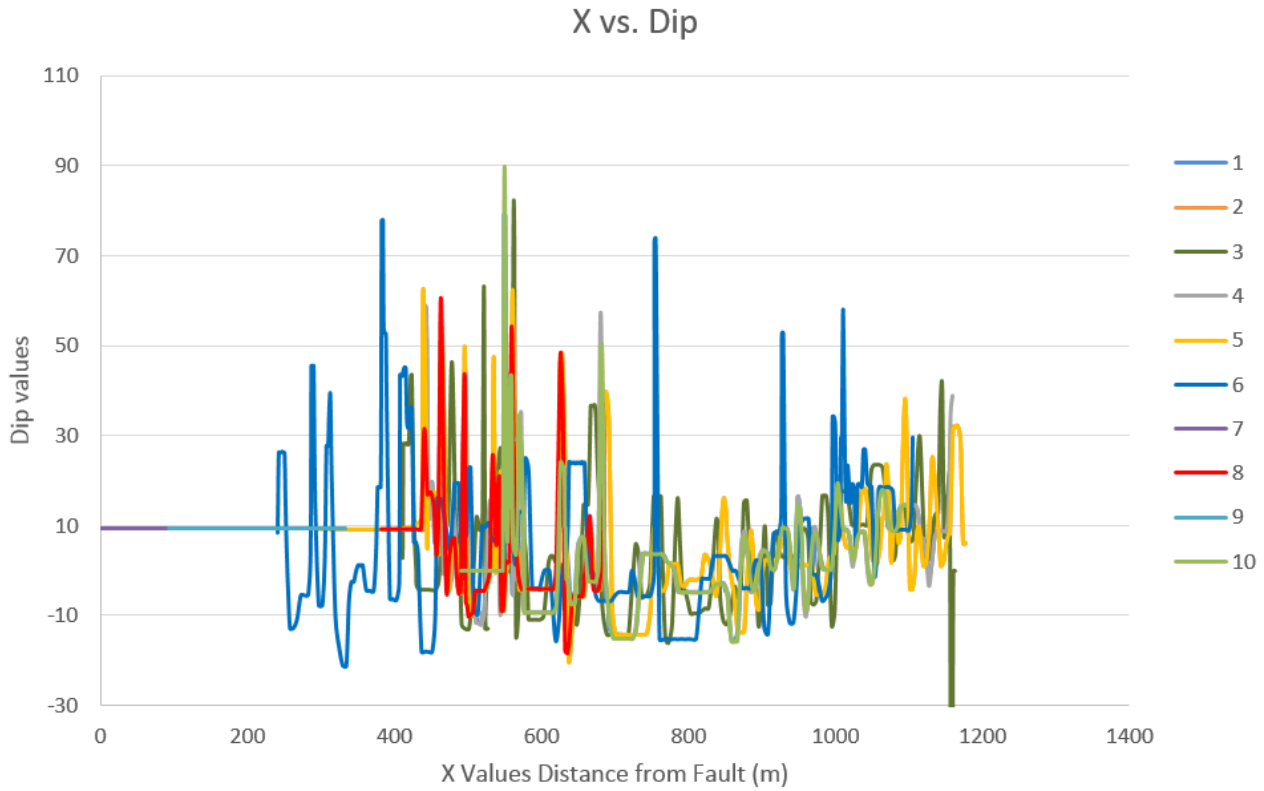


**Figure 3.16:** First generated dip variation plot displaying messy patterns dominated with peaks and troughs. The results were unsuitable for growth geometry interpretation. Dip values are plotted as Y-axis and X- values relative to the fault location are plotted as X-axis. Bedding lines are color-coded.

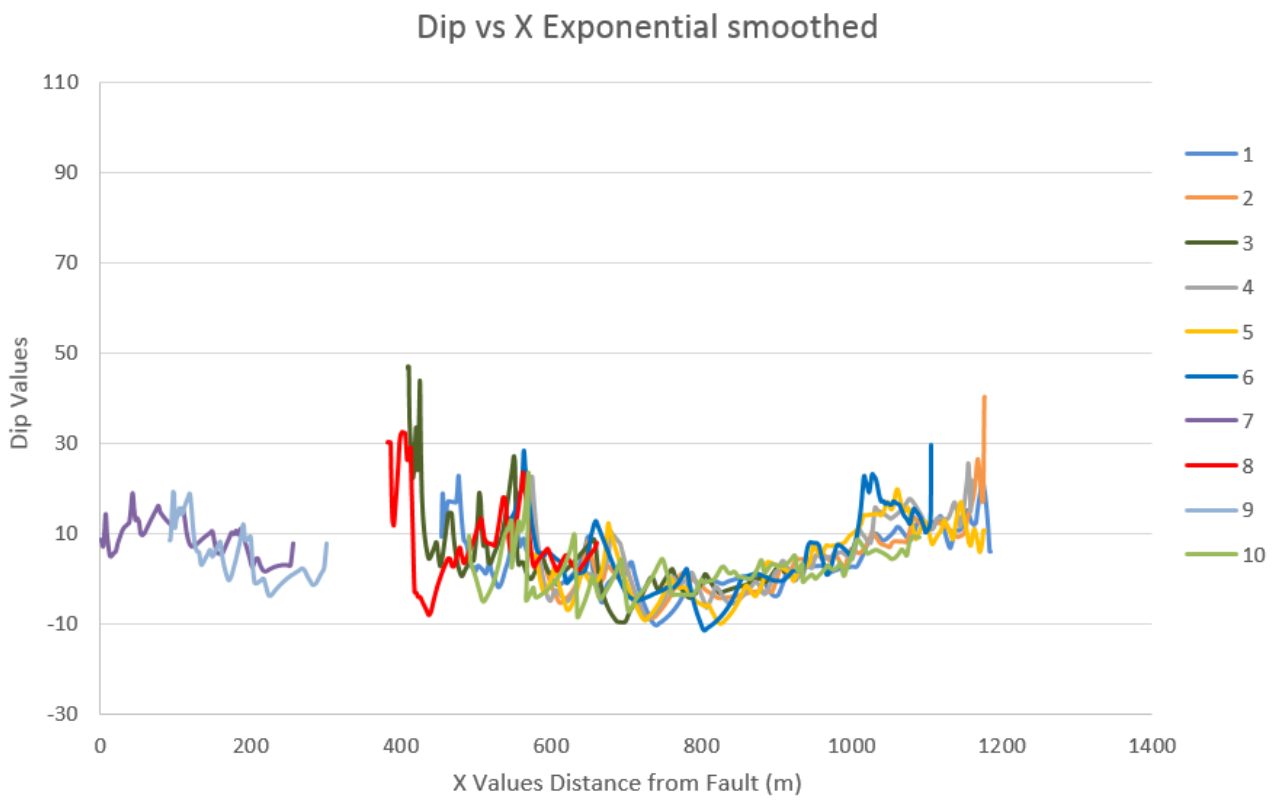


**Figure 3.17:** Exponentially smoothed dip variation plot resulted in slightly clearer dip data trend patterns and an absence of excessive peaks and troughs. Exponentially smoothed dip values are plotted as Y-axis and exponentially smoothed X- values relative to the fault location are plotted as X-axis. Bedding lines are color-coded.

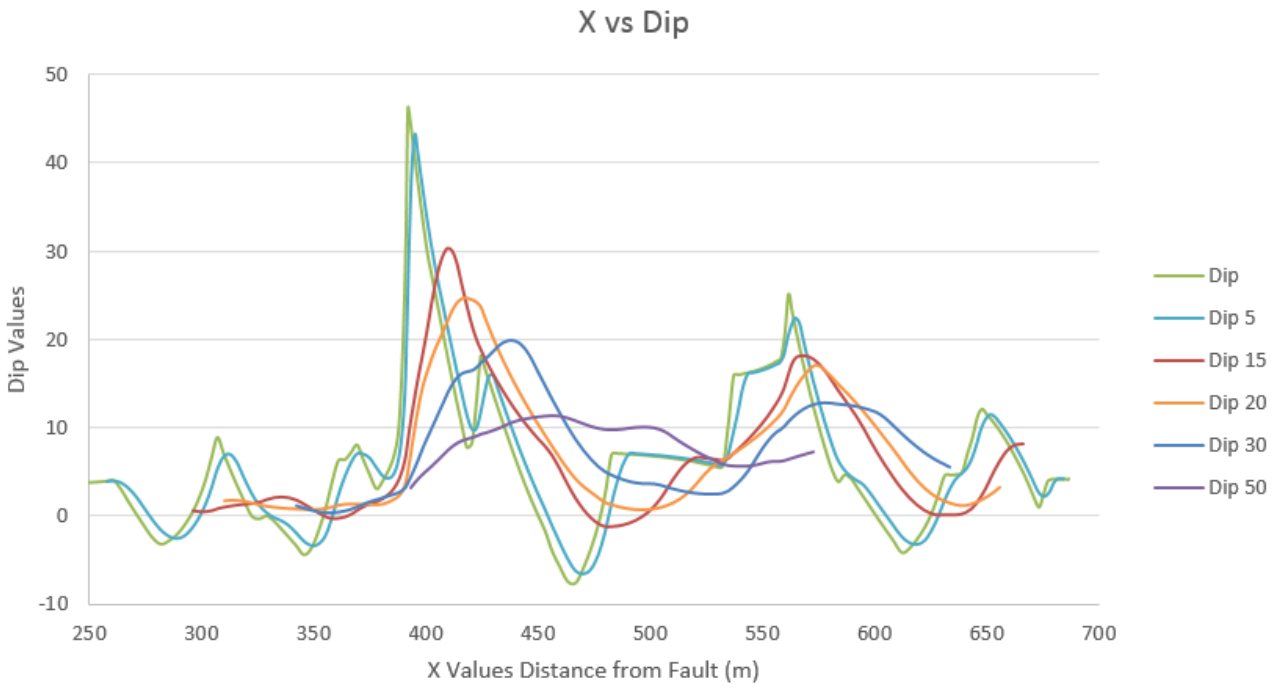


**Figure 3.18:** Example of the results for bedding line 11 using dip calculation technique using every n-th value intervals. The plot illustrates results from original dip data (Dip), with increments of 5 (Dip 5), 15 (Dip 15), 20 (Dip 20), 30 (Dip 30) and 50 (Dip 50). The most appropriate calculation is marked as Dip 15, preserving important yet smoothed fluctuations. Dip values are plotted relative to the fault's location. Bedding lines are color-coded.

### 3.11.5 Matlab Analysis

Bedding line analysis utilizing excel was followed by an additional analysis using Matlab software. The main aim of Matlab analysis was to 1) improve Excel analysis results; 2) develop a more efficient analysis technique; and 3) quality control results and analysis. The overall Matlab analysis is similar to the Excel analysis, with main differences being in $F_x$ estimation and data smoothing procedure.

#### $F_x$ Calculation

The calculation of $F_x$ was performed in Matlab to determine the lateral distance along the surface of the outcrop. When the outcrop is aligned parallel to the X axis, $F_x$ is equivalent to the X coordinate. However, when the outcrop is aligned at an angle between the X and Y axes, $F_x$ becomes a function of both X and Y coordinates (Figure 3.19). By plotting the data in 3D, the true position of the outcrop with respect to the X and Y axes can be determined, allowing

for more precise illustration of 3D data in 2D. Figure 3.19 A shows polylines from the Roghi outcrop in 3D, highlighting how the outcrop surface is aligned at an angle between the X and Y axes; the interpreted fault location is shown with the dashed like $X_O$ and $Y_O$. Figure 3.19 B shows the calculation of $F_x$ coordinates vs. raw X coordinates – note how the two points shown have similar $F_x$ values while their X coordinates are very different. As opposed to the X coordinates alone, $F_x$ values accurately represent the distance along the outcrop.

The numerical values for initial X ($X_O$) and Y ($Y_O$) coordinates determined based on the interpreted location of the bounding fault. From the bounding fault, distance along the outcrop is calculated as $F_x$ using the Pythagorean theorem by measuring the distance between subsequent bedding line points, $\Delta X$ and $\Delta Y$ (Equation 3.5).

$$F_x = \sqrt{(X_o)^2 + (Y_o)^2} + \sqrt{(\Delta X)^2 + (\Delta Y)^2} \tag{3.5}$$

**Smoothing**

The smoothing of the data was carried out using a Savitzky-Golay smoothing filter, which is generally used to smooth out the noise from data and to increase the data precision without distorting the raw data.

The filter utilizes convolution method to fit a regression equation based on a moving average with a given window size (Figure 3.20). The filter used was compared to simpler linear, cubic, and exponential smoothing filters and was most effective at handling erratic peaks and troughs in the data while preserving overall trends. An optimal window size of 30 points was chosen for the data based on trial and error and visual assessment of the resulting smoothed datasets.

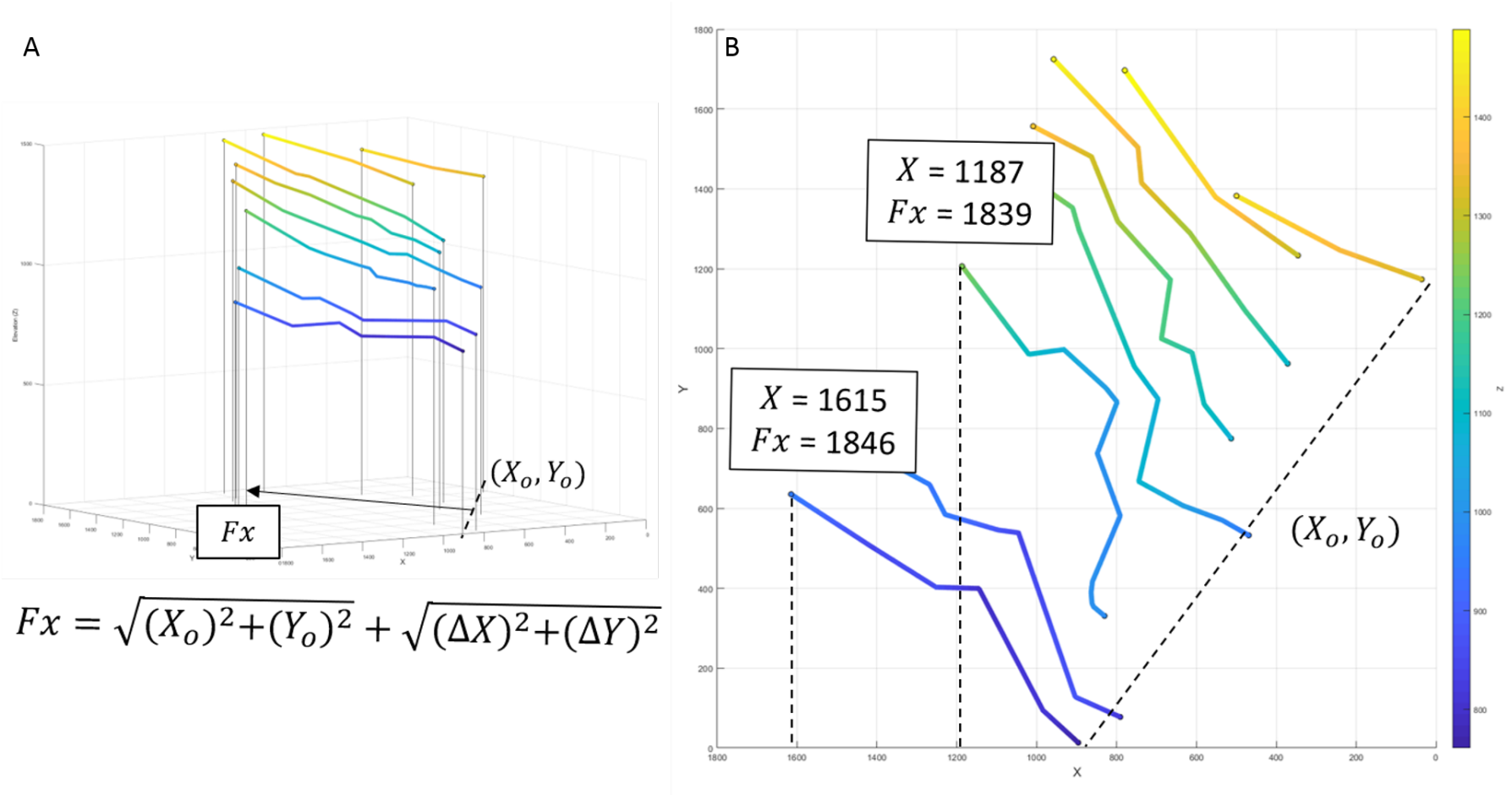


**Figure 3.19:** Conceptual sketch illustrating calculations techniques utilized for Matlab analysis using Roghi bedding line data as an example. (A) shows the outcrop in 3D, highlighting how the outcrop surface is aligned at an angle between the X and Y axes. (B) shows the difference in $F_x$ values calculated using Equation 3.5 and the use of raw X coordinates. For the two points shown, $F_x$ values are similar, as expected based on the 3D view in A, while X coordinates are very different.

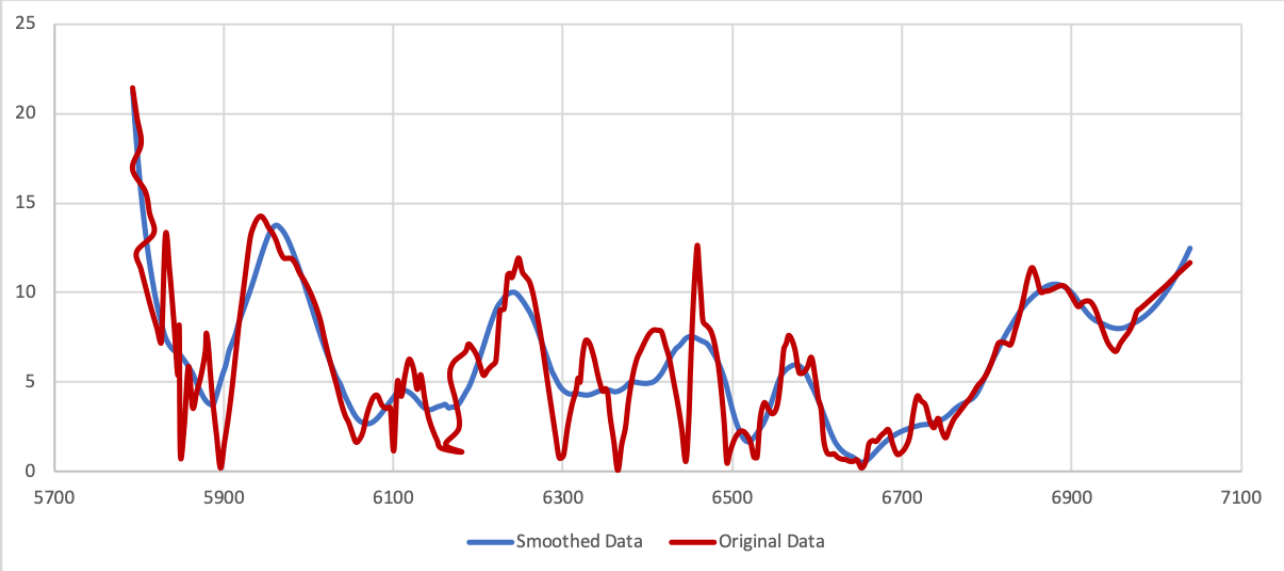


**Figure 3.20:** Plot representing smoothing effect utilizing Savitzky-Golay filter in comparison to the original bedding line data.

### Dip Calculation

Dip calculation in Matlab followed the same general method as in Excel, where the inverse tangent was used. The primary difference is that $F_x$ measurements are used to accurately view the outcrop from the strike line, thereby computing true dip (Equation 3.6) as opposed to apparent dip (Equation 3.7). Figure 3.21 illustrates the difference in dip values calculated in each manner, highlighting the importance of calculating dip from $F_x$ rather than X.

$$True\ Dip = tan^{-1}(\frac{\Delta Z}{\Delta F_x}) \tag{3.6}$$

$$Apparent\ Dip = tan^{-1}(\frac{\Delta X}{\Delta Y}) \tag{3.7}$$

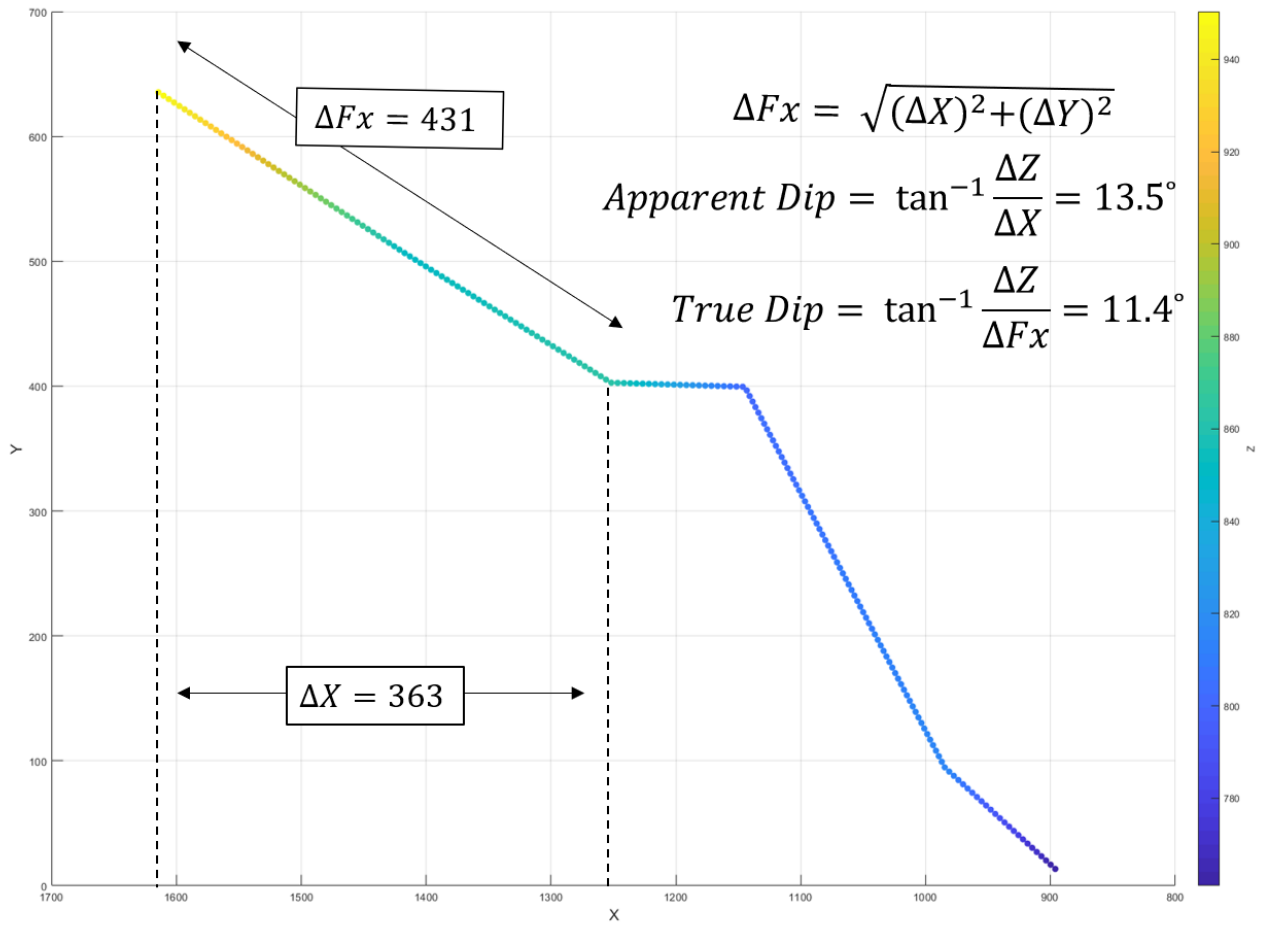


**Figure 3.21:** Conceptual sketch illustrating the difference of apparent dip (Excel analysis) and true dip (Matlab analysis) calculations. The displayed bedding lines represent Roghi outcrop.

## 3.12 Geological Challenges

The field and LiDAR data acquisition and half-graben syn-rift strata structural interpretation encountered several geological and technical challenges in the study areas. The main geological challenge was the apparent lack of typical growth strata geometry characteristics in syn-rift sequences in the outcrops, which has not been investigated in many researches before. The second challenge encountered was poor accessibility of certain outcrops due to the steep slopes and vegetation, leading to possible errors and misinterpretation due to measuring from extreme distances and poor LiDAR data coverage over vegetated portions of the outcrops. Furthermore, the weather, visibility range and presence of highly reflective surfaces contribute significant adverse effects to the quality and resolution of the data.

### 3.12.1 Viewing Angles

In addition to geological challenges some technical difficulties occurred concerning the acquisition of photographs and measurement data from the correct viewing angle (i.e., along the strike line of the dipping beds) in order to portray true dip.

The dip of the bedding lines can be expressed as an acute inclination perpendicular to the strike line. The apparent dip represents the angle between the geologic beds and any vertical plane non-perpendicular to the strike line (Figure 3.15). The bedding lines are commonly observed from various viewing angles, portraying apparent dip and depicting inaccurate bed thicknesses (Figure 3.22 and 3.23). True dip of the bedding line in the field is represented only when the viewing angle is along the strike line. Therefore, in order to determine the existence of growth geometries in addition to dip ant thickness variations assessment, the correct viewing angle is necessary. Distinguishing between true and apparent dip is important for calculating appropriate dip value result.

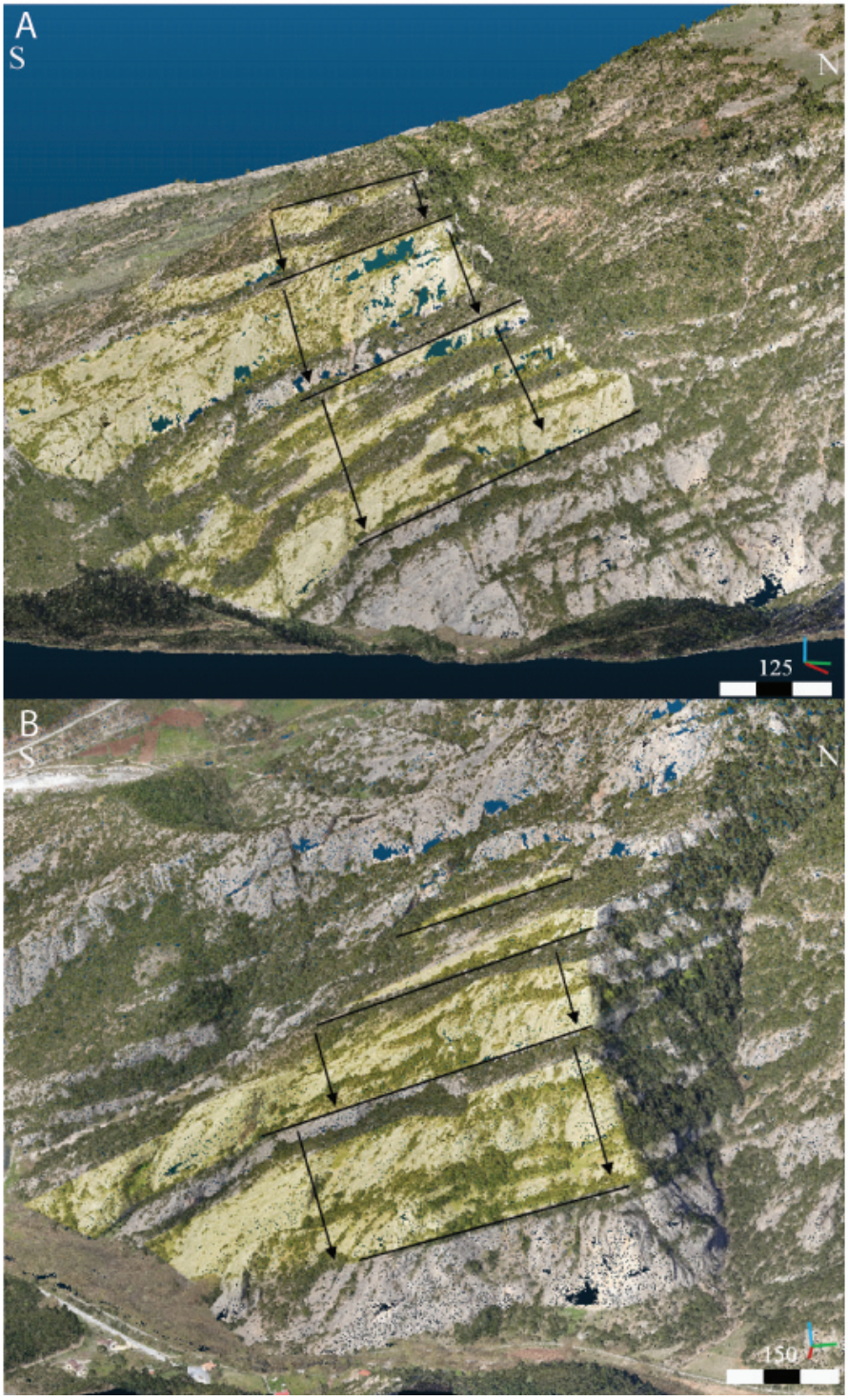


**Figure 3.22:** Two LiDAR images accentuating the importance of viewing angle, displaying Roghi West outcrop. Image A displays beds thickening towards southeast and slightly increasing dip angle down-section, while Image B displays relatively constant dip and thickness. The images view the same section of outcrop at different angles. The bedding lines are highlighted in black; bed thicknesses are highlighted with arrows; continuous beds are highlighted in yellow. The point-cloud is visualized using CloudCompare software.

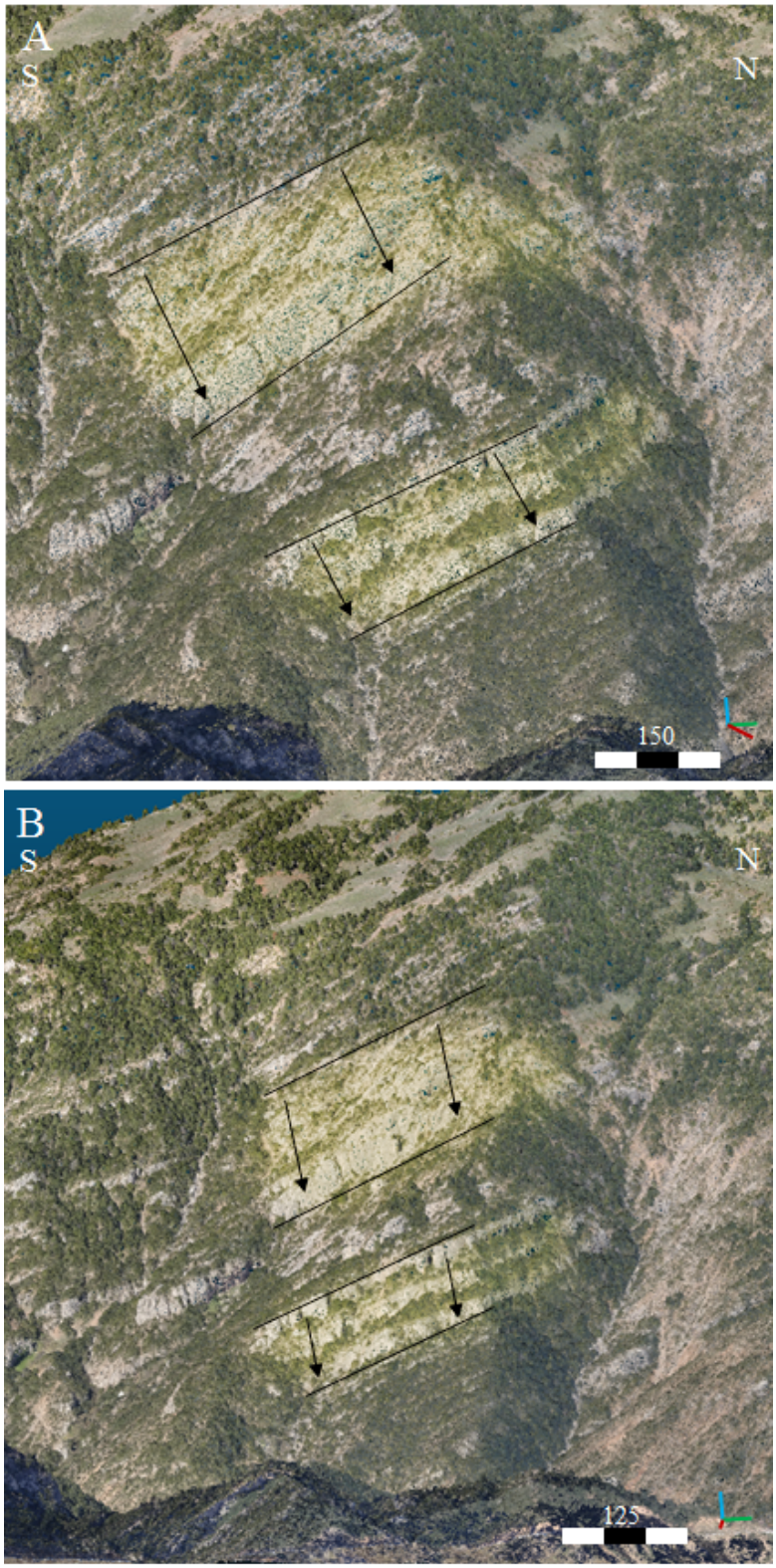


**Figure 3.23:** Two LiDAR images accentuating the importance of viewing angle, displaying Roghi West outcrop. Image A displays beds thickening towards southeast and slightly increasing dip angle down-section, while Image B displays relatively constant dip and thickness. The images view the same section of outcrop at different angles. The bedding lines are highlighted in black; bed thicknesses are highlighted with arrows; continuous beds are highlighted in yellow. The point-cloud is visualized using CloudCompare software

## 3.13 Structural Analysis Data Comparison

Structural analysis of the outcrops was carried out using two different approaches. One of the approaches was done in Excel software for all of eight investigated outcrops, while the Matlab approach was completed for outcrops with LiDAR data (Lapanagoi, Roghi and Vrachni). Several errors occurred operating with Excel software, inducing high value fluctuations and generating difficulties for data trend observations. Numerous fluctuations were removed with exponential smoothing for the Excel approach. Therefore, an additional data analysis approach was conducted in order to correct the fluctuations without excessive data smoothing.

Matlab approach corrected for angle distortion induced in data plots due to the steep outcrops angle with respect to the LiDAR instrument. Additionally, this mitigated errors occurring when 3D data is plotted in 2D. The correction allowed bedding lines to appear in their appropriate positions (i.e., stacked under each other) with nearly equal increments between data points which improved the dataset and made the interpolation process unnecessary. The interpolation step used in Excel approach re-positions the interpolated bedding line and, therefore, might distort the real data results.

The data achieved with Excel was appropriate for the structural analysis plot interpretation, once the data was smoothed. Furthermore, the approach include dip data smoothing by calculating every $15^{th}$ value. The Matlab approach is more effective, preserving the most raw data and producing correct dip results with minimal additional smoothing. Furthermore, the automatic calculation and data import/export provides a quicker way to achieve higher quality results by minimizing the occurrence of common errors due to manual calculations.

The Matlab results from Lapanagoi outcrop display main changes of positive dip values, while Excel results contained negative values between 700-1000 $F_x$ (Figure 3.24). The most distinctive effect of different approaches can be spotted in the Roghi outcrop's results (Figure 3.25). The improvements were 1) bedding lines positioned realistically; 2) dip values preserved a general trend; and 3) lower thickness values matching the field interpretation more accurately. A review of Vrachni dip plot indicates well preserved data value trends using Matlab's approach, while Excel dip values indicate highly smoothed and slightly altered trends (Figure 3.26). Both approaches display negative thickness values of bedding lines, although, only Matlab approach

exhibit bedding line fluctuations and bedding line inter-crossing, explaining the negative results, while Excel does not. The Matlab approach displays bedding line crossing due to the projection of 3D data into a 2D plot being an inherently limited calculation due to irregular roughness of the outcrop surface. Ultimately, the Matlab approach is better, as it preserves field data better. However, smoothed Excel result represent similar data trends in the majority of cases. The Excel approach is therefore useful for a preliminary assessment of data, and the Matlab approach can be used subsequently to improve quality of results as needed (e.g., the Roghi outcrop).

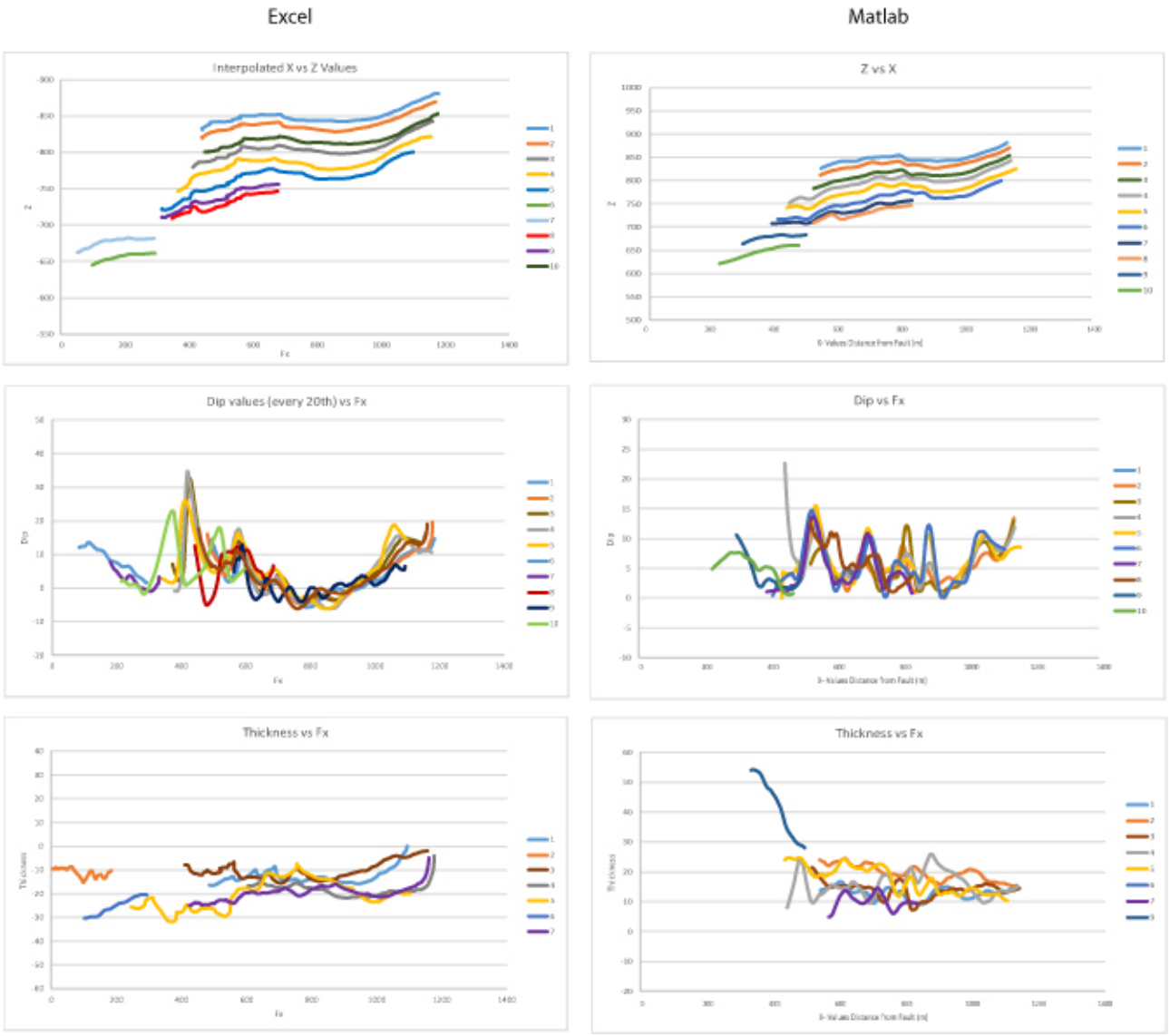


**Figure 3.24:** Structural analysis of Lapanagoi outcrop displaying bedding line, dip and thickness plots achieved applying two approaches utilizing Excel and Matlab software.

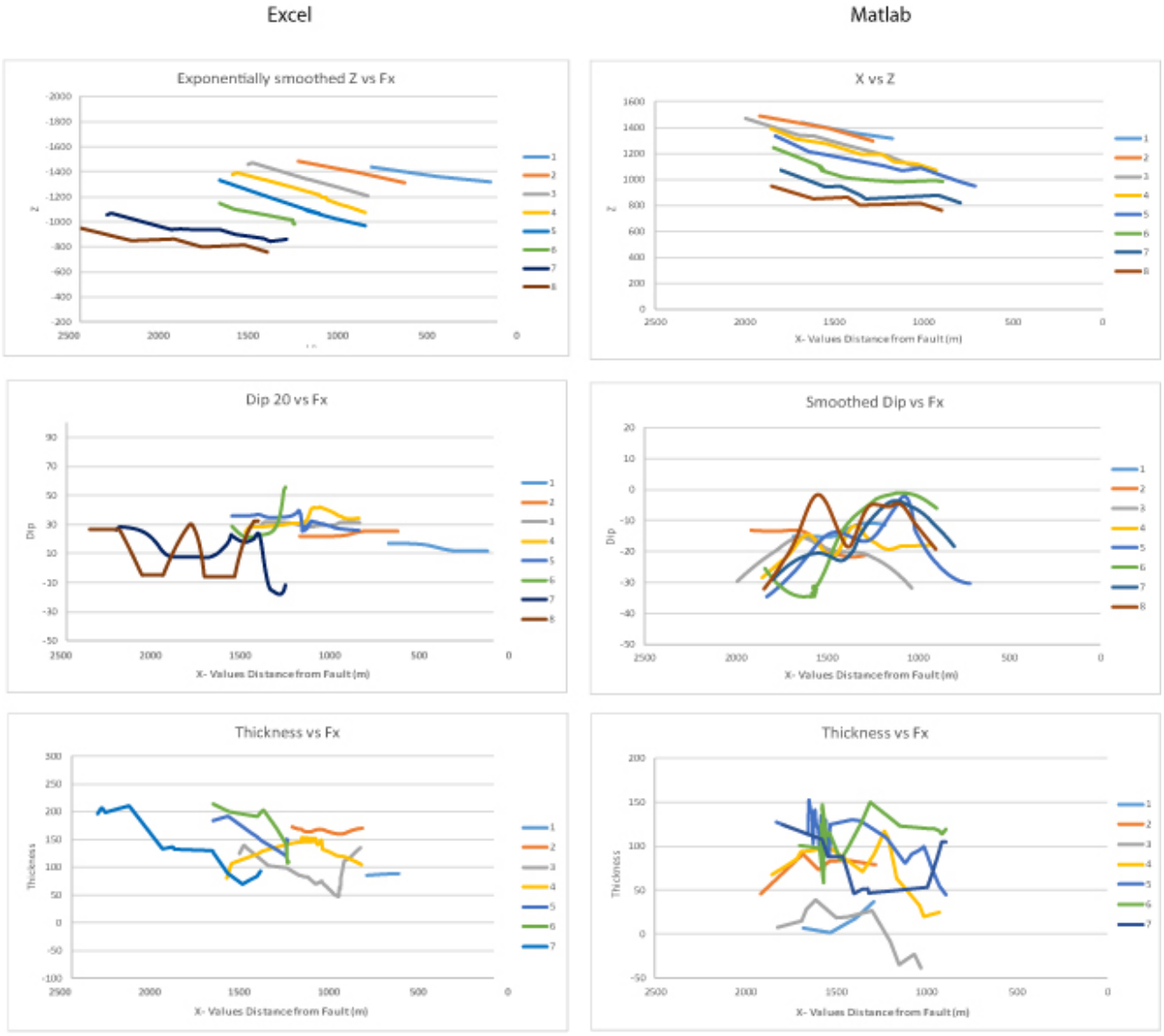


**Figure 3.25:** Structural analysis of Roghi outcrop displaying bedding line, dip and thickness plots achieved applying two approaches utilizing Excel and Matlab software.

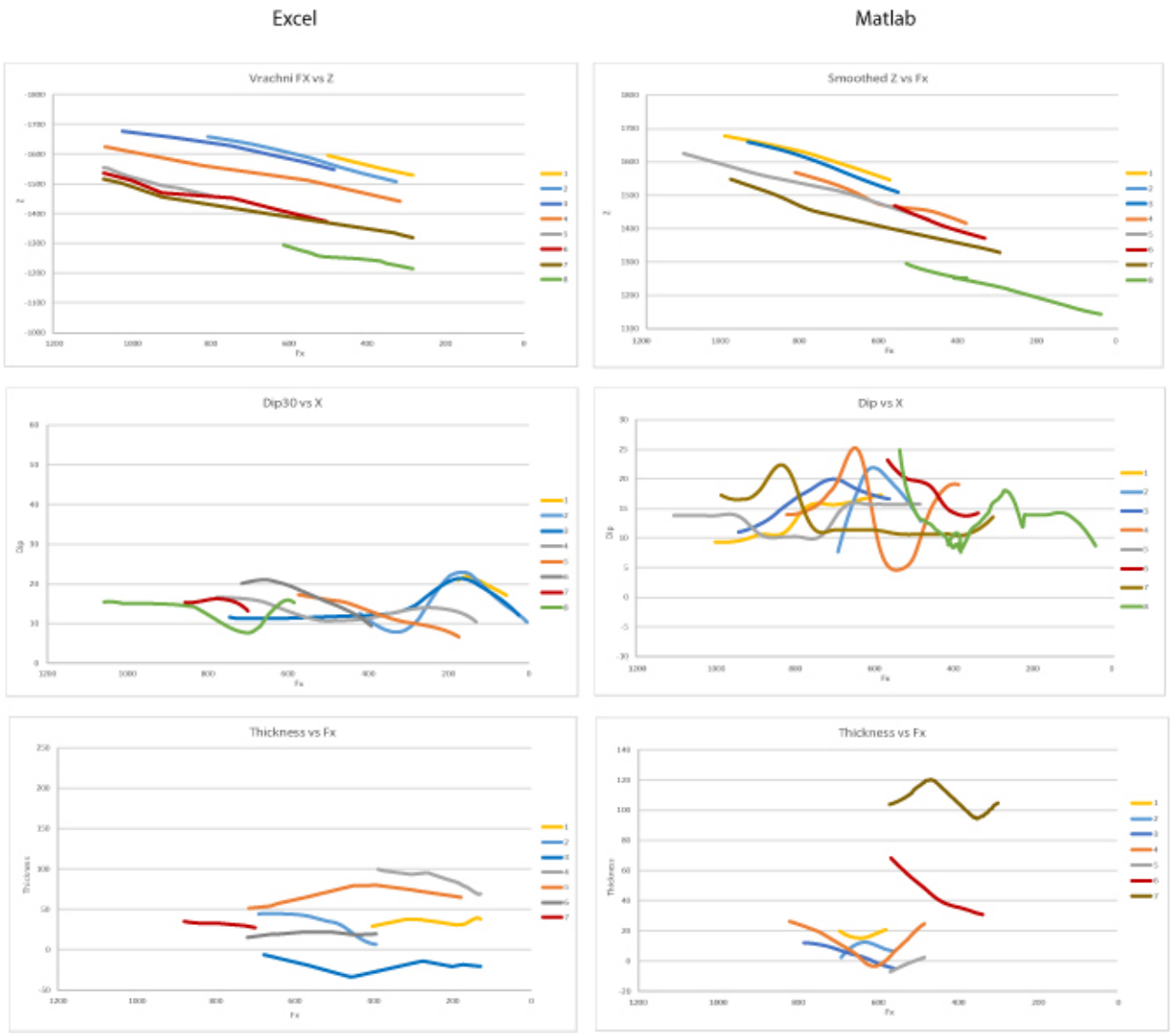


**Figure 3.26:** Structural analysis of Vrachni outcrop displaying bedding line, dip and thickness plots achieved applying two approaches utilizing Excel and Matlab software.

# Chapter 4

# Structural Analysis

Structural analysis was performed for the acquired field data in order to assess the existence of growth geometry structures in the syn-rift packages. The analysis included two approaches with various structural and integrated statistical methods, as mentioned in the Methodology chapter (Chapter 3). The methods performed on data include filtering, smoothing and highlighting of the desired bedding line data features. Structural analysis chapter provides general overview of the outcrops geological and structural features and its structural analysis, LiDAR data acquisition explanation provided for Lapanagoi, Roghi and Vrachni outcrops in addition to bedding line standard deviation assessment. Standard deviation was calculated for dip and thickness values in order to assess numerical value variations providing additional input for data quality control. Analyzed outcrops are ordered from highest to lowest data quality in the chapter, respectively, based on the outcrops field exposure, result quality and interpreted bedding line quantity of the outcrop. The spreadsheets containing structural analysis results are located at UiS shared drive at location Q:*Greece*\Greece2019\.

## 4.1 Lapanagoi

### 4.1.1 General Information

The Lapanagoi outcrop was named after the nearest village, stretching from the Makelarias Monastery in the south to the Leontio village in the north (Figure 4.1). The outcrop appears

36 km northwest from the Kalavryta town. The Lapanagoi comprise of massive conglomerate beds displaying constant thickness and no dip variations (Figure 4.2). Lapanagoi area display a sudden drop in elevation inducing a contact between the outcropping conglomerates and the pre-rift basement packages to the northwest from the outcrop, as highlighted in Figure 4.2. The high elevation decrease could be caused by a transverse fault or erosional unconformity. The outcrop of Lapanagoi continues until the Makelarias Monastery in the southeast, with a gap created by a river incision.

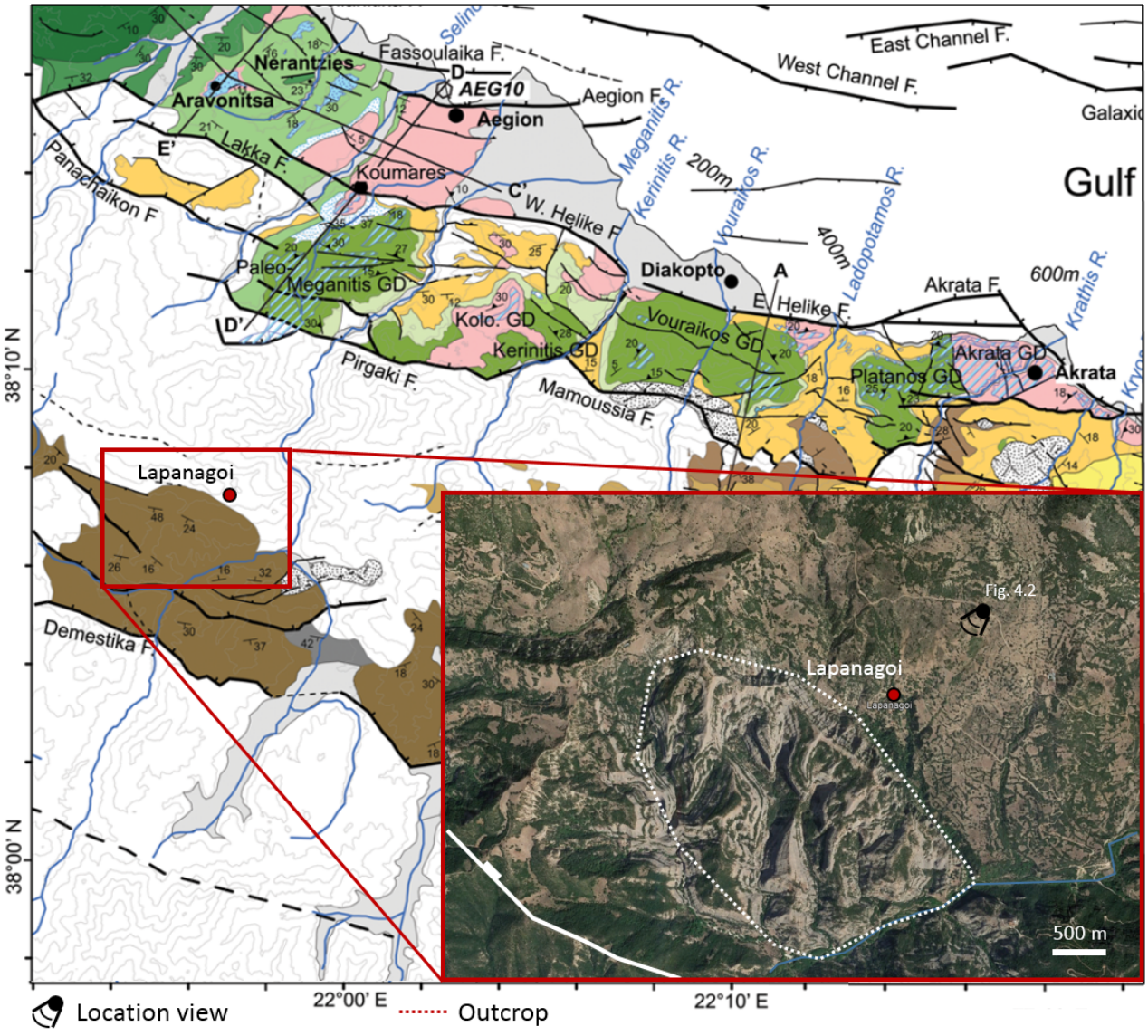


**Figure 4.1:** Map representing Lapanagoi outcrops location illustrating rivers highlighted in blue and faults in white. The top-view of the outcrop is displayed in a red rectangle. Location view of Figure 4.2 is indicated. Satellite imagery was retrieved from Google Earth Pro. Map is modified after Ford, Hemelsdael, et al. 2016.

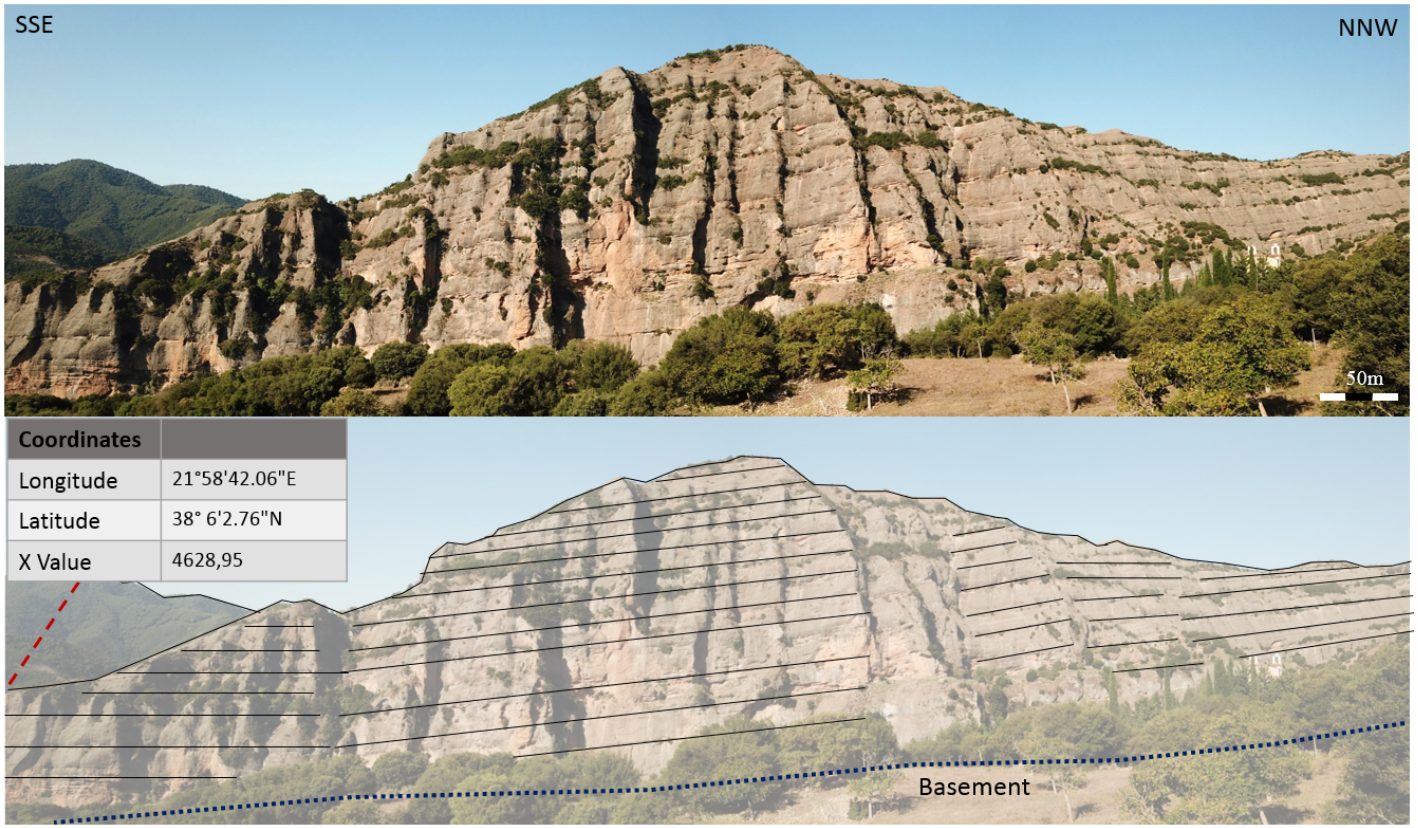


**Figure 4.2:** Photographs portraying Lapanagoi outcrop's structural features and bedding alignment. Additional inset table indicate coordinates and X values representing approximate geographic fault location. The boundary between basement and conglomerate is highlighted with dark blue dashed line.

### 4.1.2 LiDAR Data

LiDAR data of Lapanagoi outcrop was acquired using six different locations and various acquisition range angles, comprising small amount of vegetation and resulting in a high quality point-cloud (Figure 4.3). The generated point-cloud consists of 133 385 695 points, covering an area of 16 $km^2$. The bedding lines were interpreted from the point-cloud, used for structural analysis plot generation.

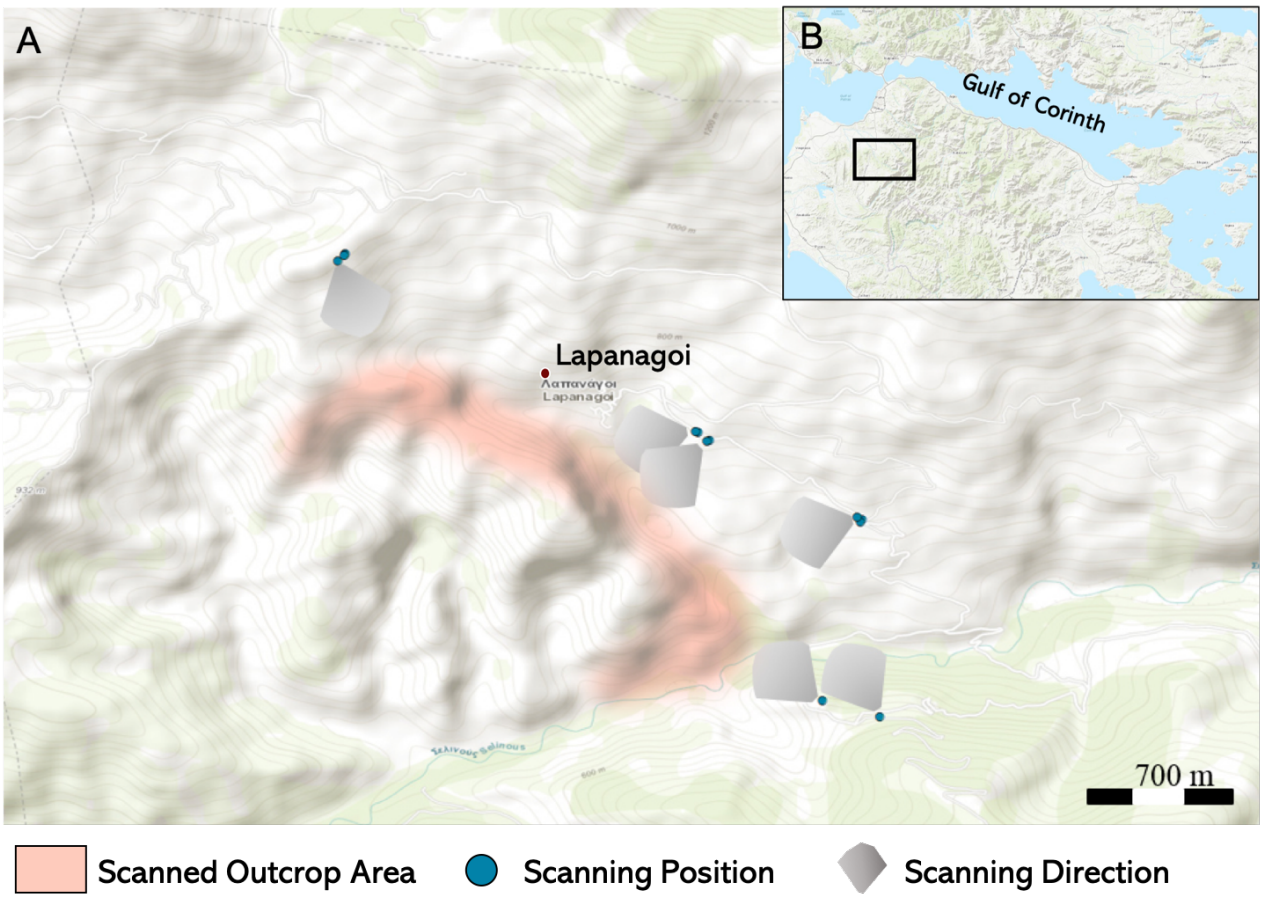


**Figure 4.3:** Map illustrating LiDAR data acquisition locations with scanning angle and range for Lapanagoi outcrop. The scanned outcrop's wall is highlighted in red. The inset map of Figure B display location of the map in Figure A.

### 4.1.3 Structural Analysis

Lapanagoi is one of the highest quality exhibiting outcrops, consisting of ten bedding lines. Bedding line plot of Lapanagoi outcrop display nearly identical bedding lines to the lines generated utilizing point-cloud data (Figure 4.4). Therefore, the created bedding line plot is of high quality, visualizing data appropriate for further analysis. The generated bedding line plot

exhibit a few modest bumps empathizing the sections exhibiting abrupt change in the outcrop wall marked as locations a, b and c in Figure 4.4.

The bedding line plot examination demonstrate relatively constant trends with value fluctuations appearing at $F_x$ values 5900, 6250, 6400, 6500 and 6850. In order to validate dip trends from bedding line plot, dip plot was inspected. The overall dip variations are minor in the most of the bedding lines, exposing peaks in five different areas induced by the largest outcrop walls irregularities and corresponding to the bedding line fluctuations in the bedding line plot (Figure 4.5). A slight bedding line deviation is represented by the dip results of bedding line 10, exhibiting contrasting trend, due to the location of the bedding line appearing on the outcrops eastern edge, in area of lower elevation.

Thickness plot results represent 8 out of 10 bedding lines due to lack of the overlap between overlaying and underlaying lines. Further analysis of thickness plot, presented fluctuating thickness values induced by bedding line fluctuations (Figure 4.6). Thickness variation plot indicate uniform bedding line thickness values, non-indicative of thickness increase towards the west, except for bedding line 9 illustrating a substantial thickness increase towards the east. The thickness increase is partially induced by angle distortion, although, the bedding line appearing on the most eroded side of the outcrop, display dip increase towards the east. Thickness change of the bedding line 9 represents contrasting results and uncertain data, based on singular bedding line result, which in consequence is not reliable.

Furthermore, standard deviation results of Lapanagoi outcrop indicate relatively uniform dip and thickness values except for the bedding line 9 with standard deviation of 14.57 (Table 4.1). The low quality bedding line displays immense thickness increase of approximately 25 meters. Standard deviation dip results display slightly lower standard deviation values compared with thickness, resulting in high quality bedding line dip and thickness calculation results with slight value deviations.

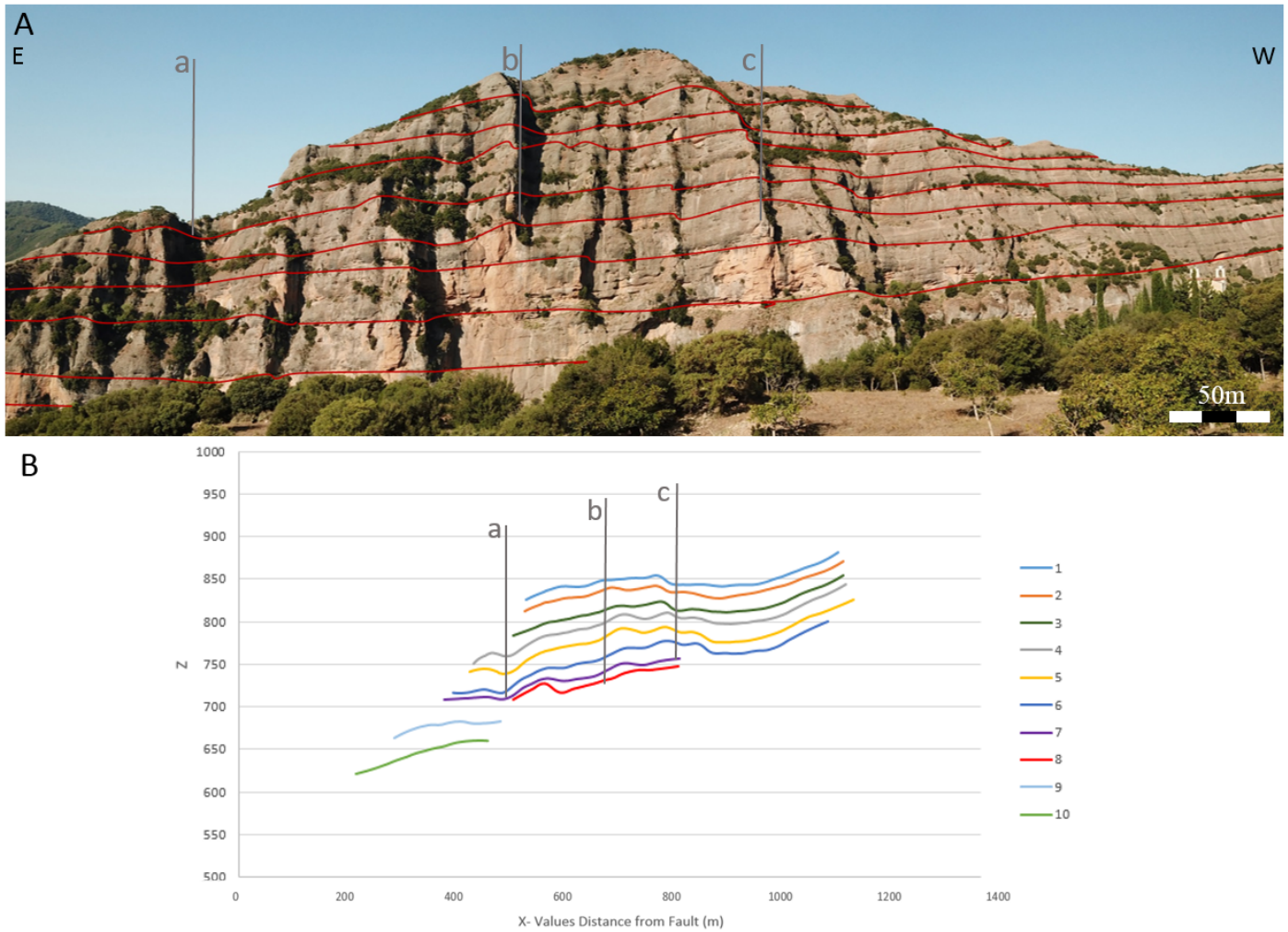


**Figure 4.4:** Figure A displays interpreted bedding lines of the Lapanagoi outcrop. Figure B represents the corresponding bedding lines plotted in 2D plot.

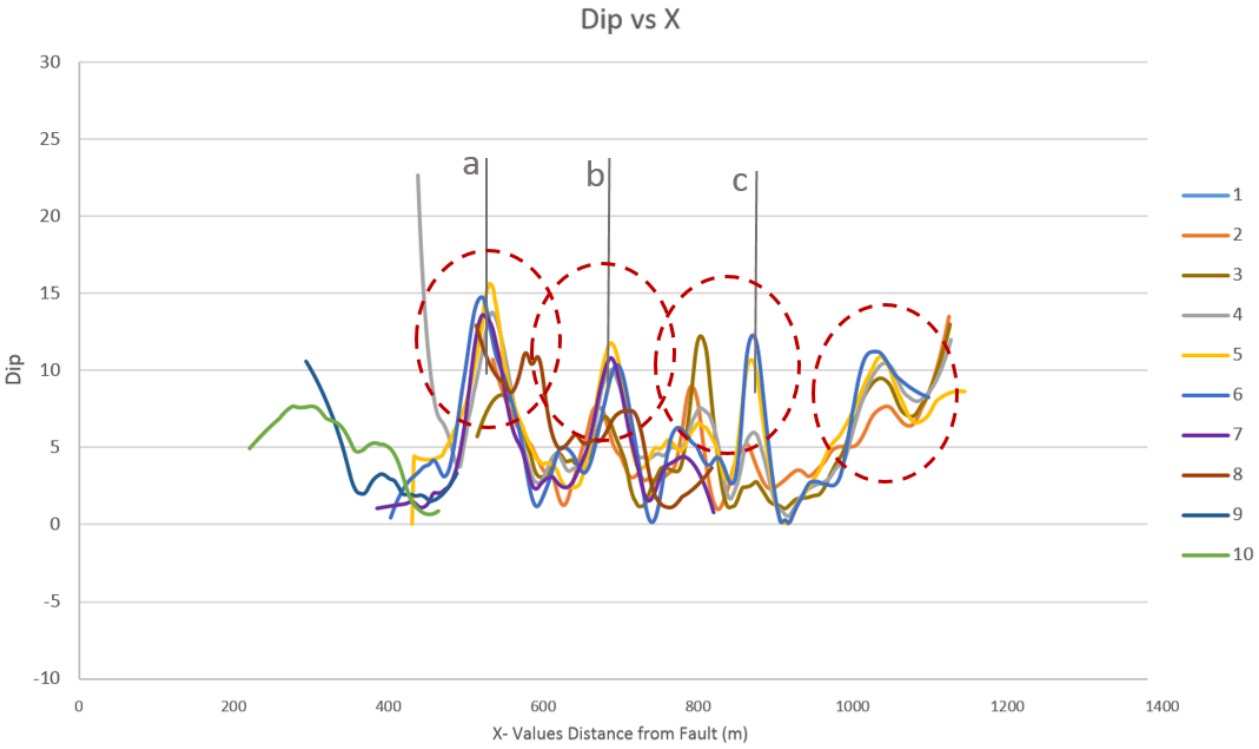


**Figure 4.5:** Dip variation plot of Lapanagoi outcrop illustrating dip value fluctuations. Four areas marked with red circles represent the highest peaks marking the largest irregularities of the outcrop surface.

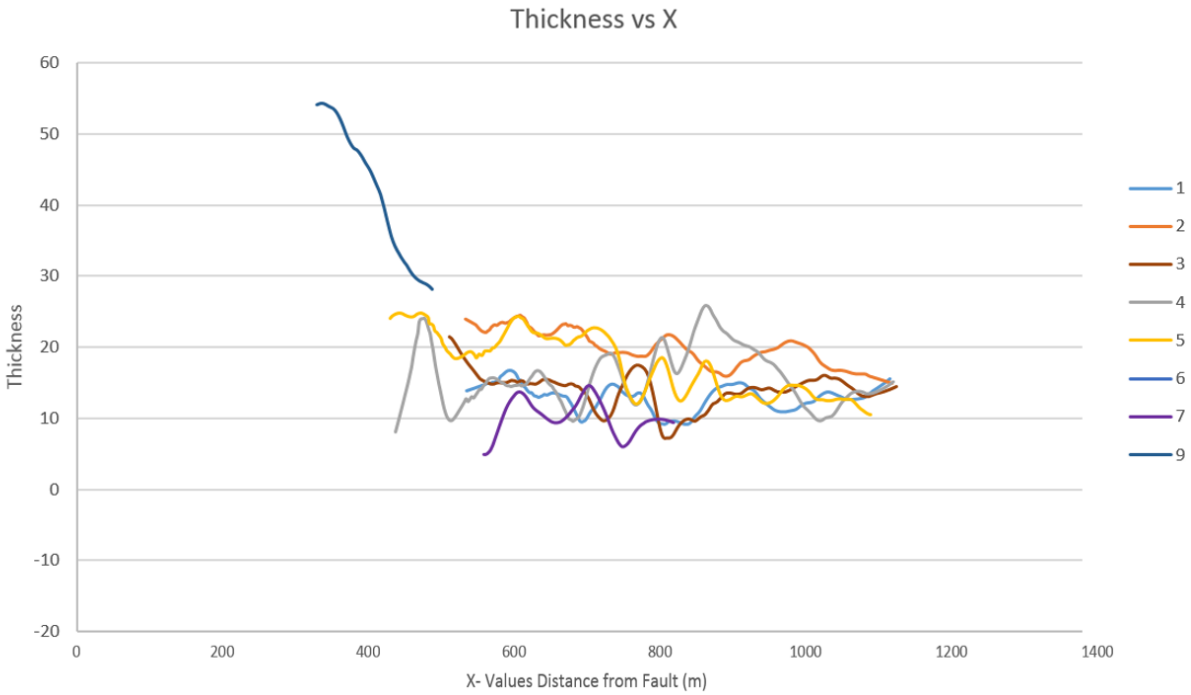


**Figure 4.6:** Thickness variation plot illustrating thickness value fluctuations of the Lapanagoi outcrop.

| | Bedding Line nr. | Standard Deviation | |
|---|---|---|---|
| | | Dip | Thickness |
| Lapanagoi | 1 | 3.45 | 1.83 |
| | 2 | 2.47 | 2.52 |
| | 3 | 3.06 | 4.92 |
| | 4 | 3.57 | 4.14 |
| | 5 | 3.22 | 4.31 |
| | 6 | 3.70 | 4.73 |
| | 7 | 3.54 | 2.45 |
| | 8 | 3.23 | N/A |
| | 9 | 2.61 | 14.57 |
| | 10 | 2.21 | N/A |

**Table 4.1:** Standard deviation of bedding line dip and thickness values for Lapanagoi structural analysis.

## 4.2 Roghi

### 4.2.1 General Information

Roghi outcrop was named after the nearest Roghi village, situated approximately 10 km north-east from the Kalavryta town (Figure 4.7). The outcrop comprises of rotated syn-rift conglomerate deposits overlaying the limestone basement. The outcrop is dominated by the beds dipping at high angle, terminated by a fault to the northeast (Figure 4.8). The lower part of the outcrop exhibit two geological contacts between syn-rift conglomeratic deposits and limestone basement (Figure 4.9). Figure 4.9 display field observations of the area matching interpretation of Ford et al. (2013). Although, big scale field observations are contrasting Ford et al. (2013) results, due to the dissimilar bedding line interpretations.

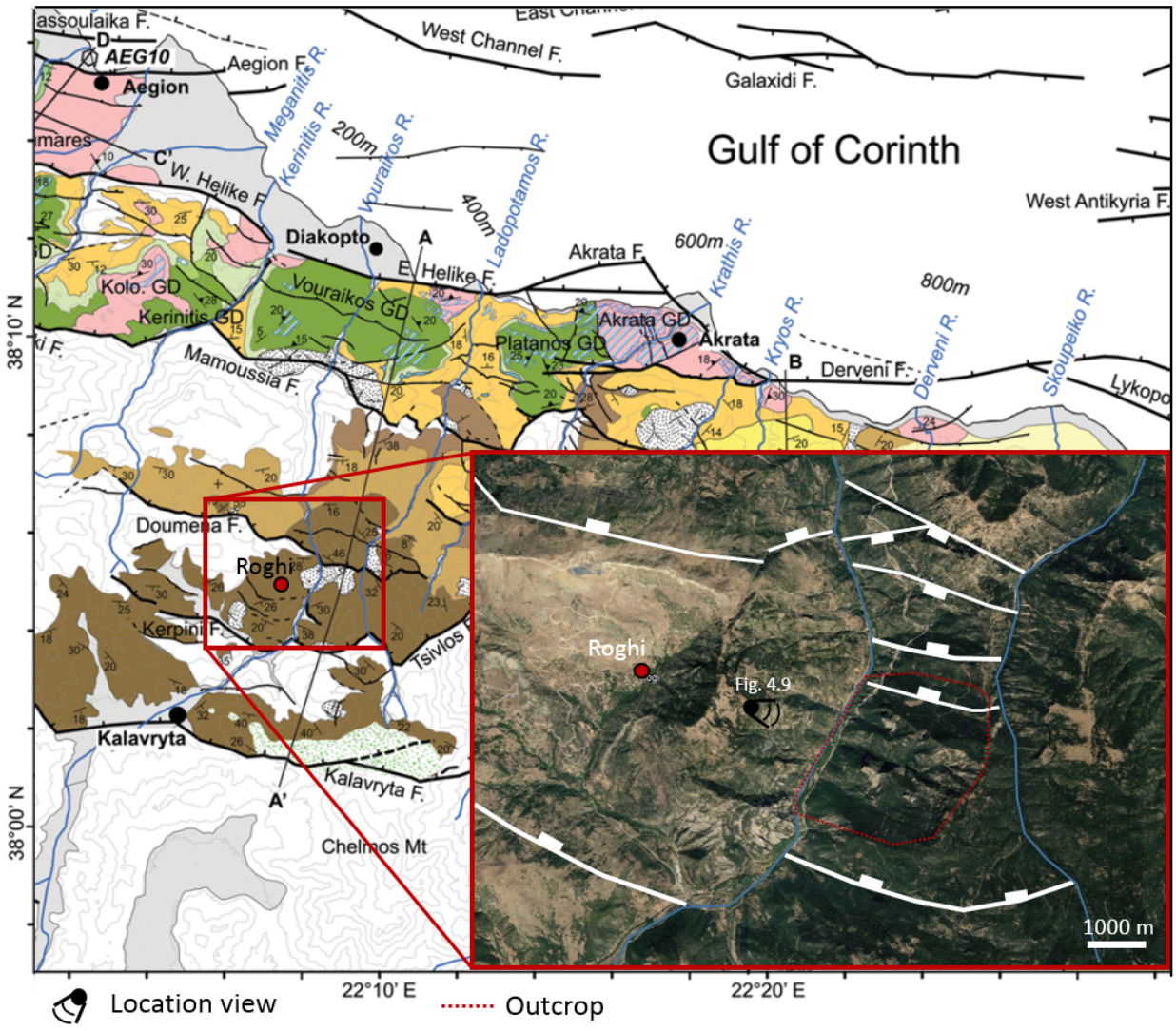


**Figure 4.7:** Map displaying location of Roghi outcrop illustrating rivers highlighted in blue and faults in white. The top-view of the outcrop is displayed in a red rectangle. Location view of Figure 4.8 is indicated. Satellite imagery was retrieved from Google Earth Pro. Map is modified after Ford, Hemelsdael, et al. 2016.

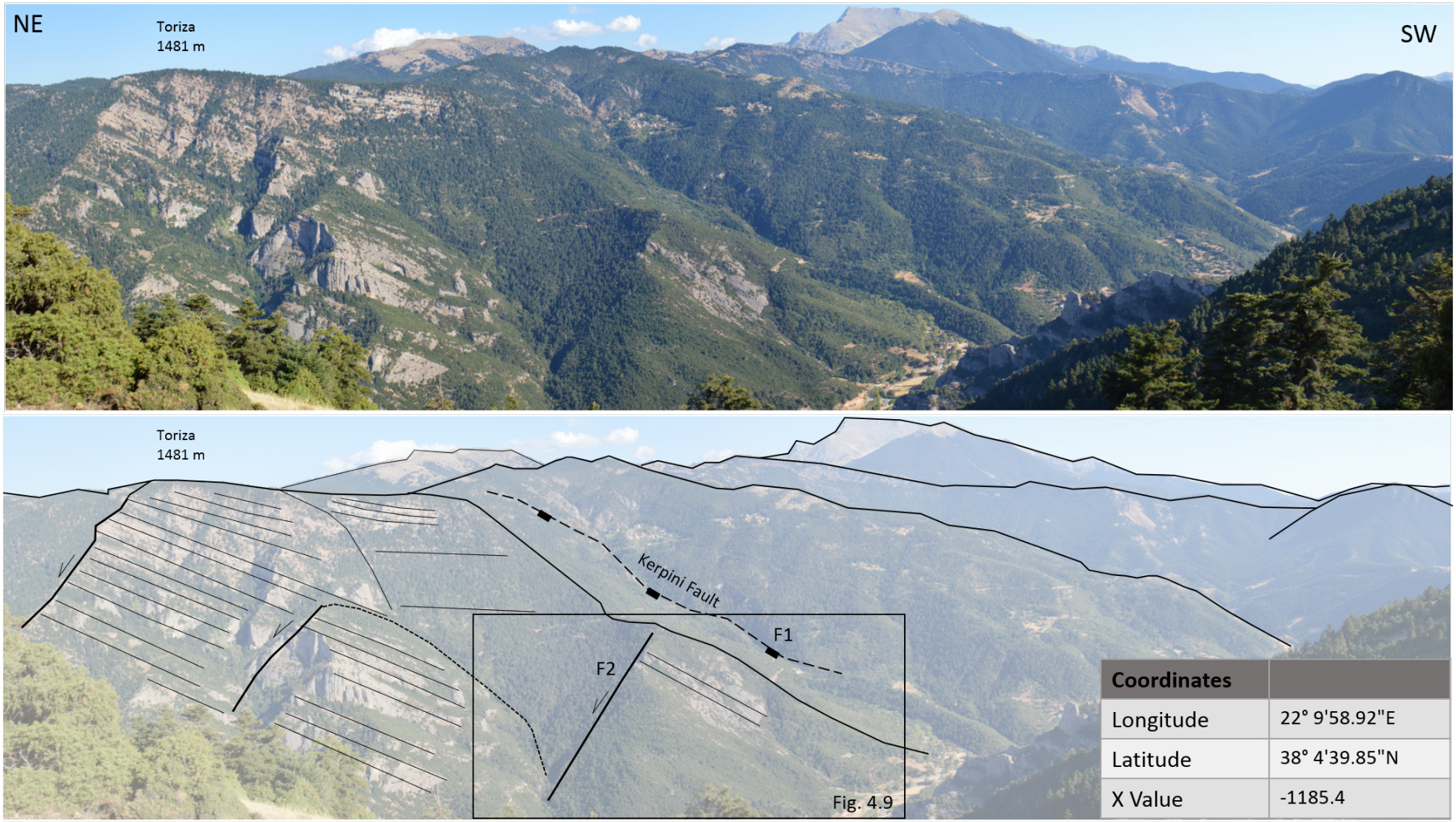


**Figure 4.8:** Field interpretation of the bedding in the Roghi outcrop. Kerpini fault (F1) is highlighted as a dashed line. The coordinate table indicates fault's location used as a reference point for structural analysis plot creation.

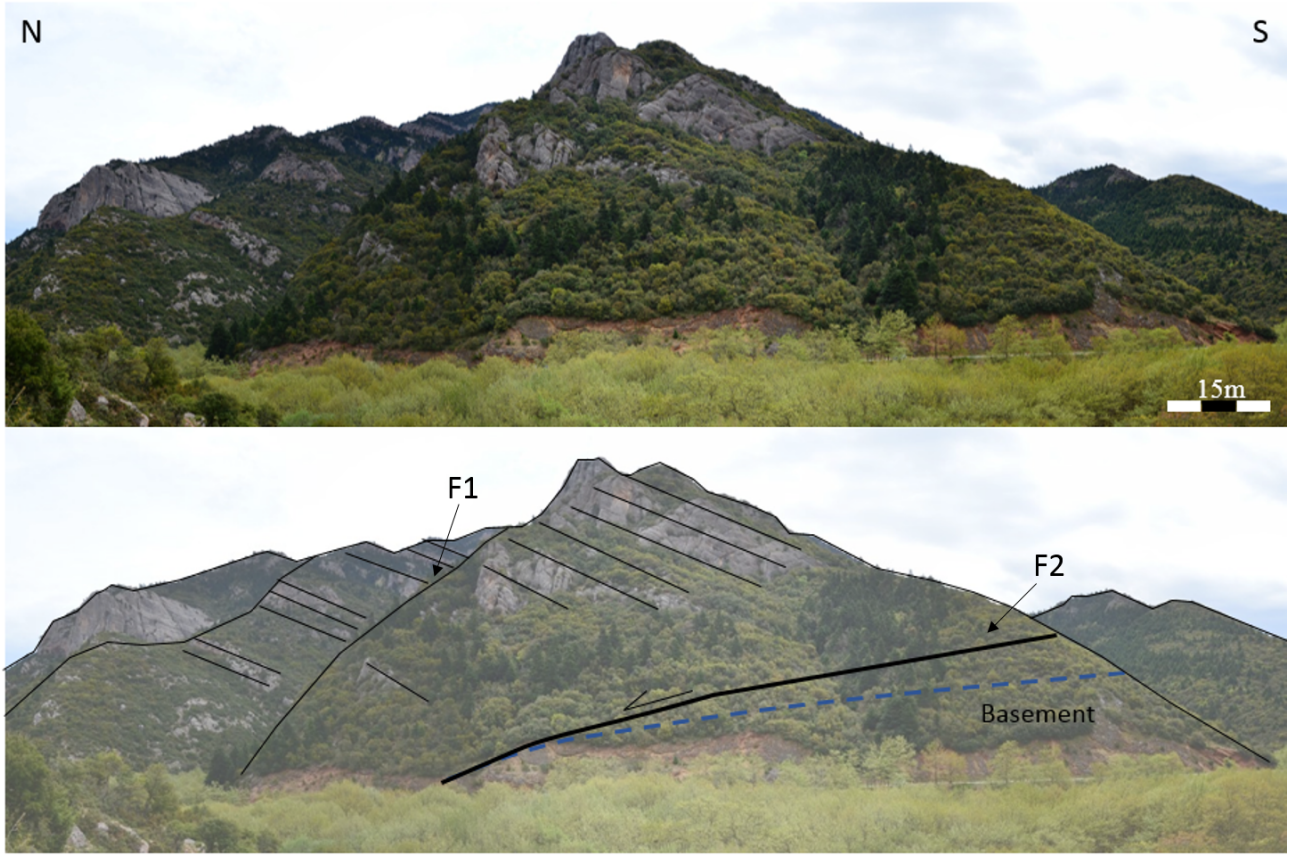


**Figure 4.9:** Field interpretation of the bedding, unconformity (highlighted in blue) and fault (highlighted in black) in the Roghi outcrop. Location of the image is marked in Figure 4.8.

### 4.2.2 LiDAR Data

The Roghi outcrop's terrestrial LiDAR data was assembled from five acquisition locations comprising of various acquisition angles (Figure 4.10). The resultant point-cloud encompass 135 064 354 points, covering an area of 12 $km^2$. The outcrop exposure is adequate, absent of vegetation covering the sediments and, therefore, exhibiting good data quality.

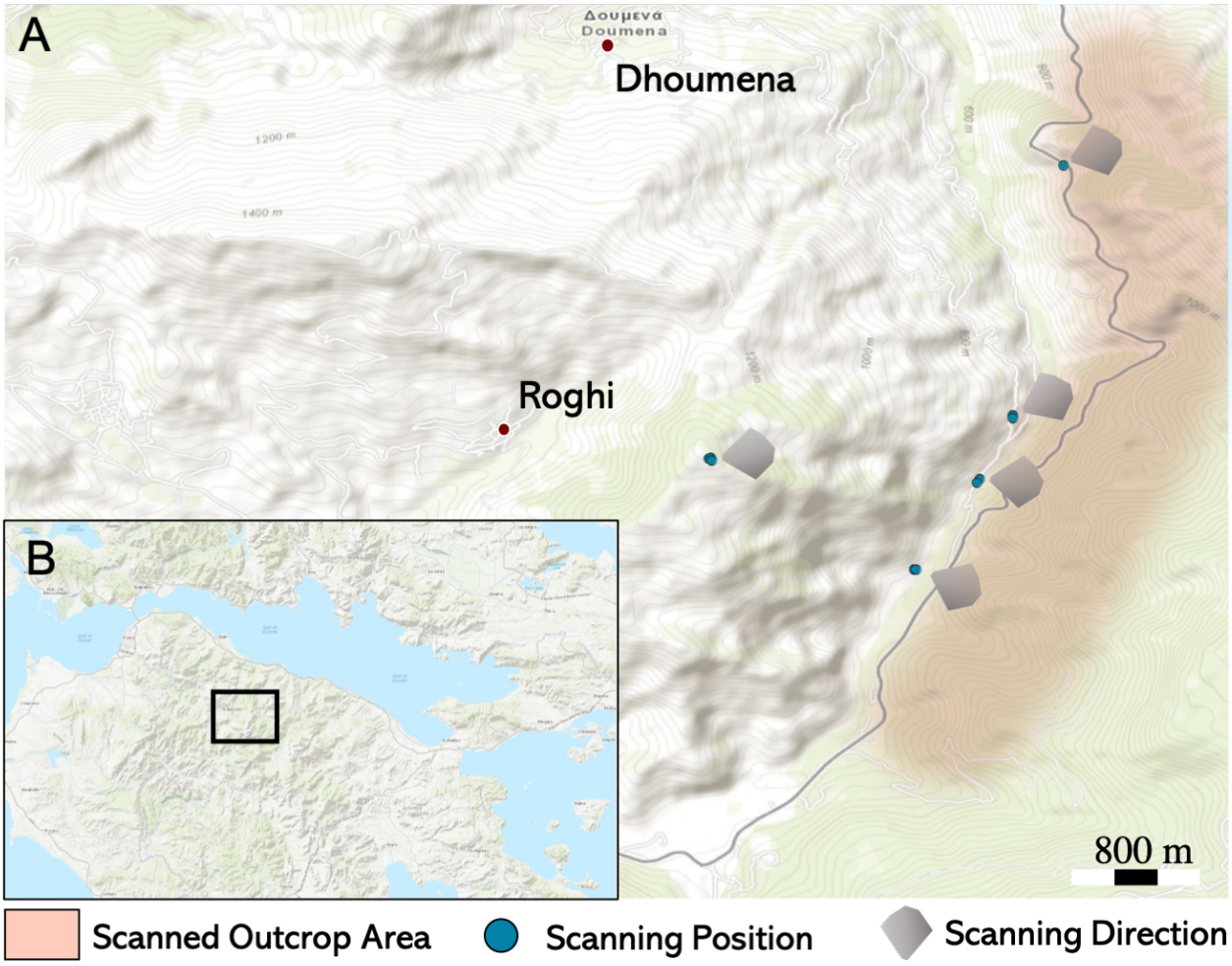


**Figure 4.10:** Map representation of LiDAR scanning positions and directions for Roghi outcrop. The final scanned outcrop area is highlighted in red. Figure B is an inset map indicating the location of Figure A.

### 4.2.3 Structural Analysis

In total, eight bedding lines were interpreted in Roghi outcrop. The bedding line plot of the outcrop represents bedding lines well, displaying minor data aberrations (Figure 4.11). Bedding line plot indicate slight changes in bedding line thicknesses with relatively constant dip.

In order to assess dip variations, bedding line dip variation plot was examined (Figure 4.12). The structural analysis dip plot display general anticlinal data trend of increasing ($F_x = 1000$), followed by decreasing towards the Kerpini fault ($F_x = 1500$) and subsequent increase in dip. The anticlinal feature displayed by dip values is due to the bedding line value fluctuation induced by overlap and nonparallel line trend. Furthermore, dip value decrease towards the southeastern part of the outcrop reveals lack of growth strata. A contrasting trend is indicated by the bedding

line 6 illustrating dip value decrease, displaying small interval of value fluctuations approaching the lowest thickness value.

Thickness variations were reviewed utilizing bedding line thickness plot, resulting in high value fluctuations in bedding lines 5 and 6 and moderate variations in the rest of the bedding lines (Figure 4.13). Bedding line 3 display negative thickness values due to the bedding line overlap, exhibited in the bedding line plot. Generally, bedding line thicknesses are decreasing towards the southwest (towards the fault), despite the fluctuations. Regardless of bedding line value fluctuations, general bedding line trend indicate syn-rift packages absent of growth geometries.

Standard deviation analysis of the bedding line dip and thickness value calculations display higher deviations compared to Lapanagoi outcrop. Standard dip deviation values for bedding lines 5, 6, 7 and 8 indicate moderate dip quality values displaying high value fluctuations, with the highest value exhibited by bedding line 6 (Table 4.2). Thickness deviations are relatively uniform, where bedding line 1 display lowest deviation value of 10.19 and bedding line 7 demonstrate the highest standard deviation value of 27.83. Since most of the bedding lines appear near the average deviation value of 22, the data quality can be rated as good. High standard deviation values for Roghi outcrop are caused by highly dipping beds, viewing angle difficulties and bedding line overlaps.

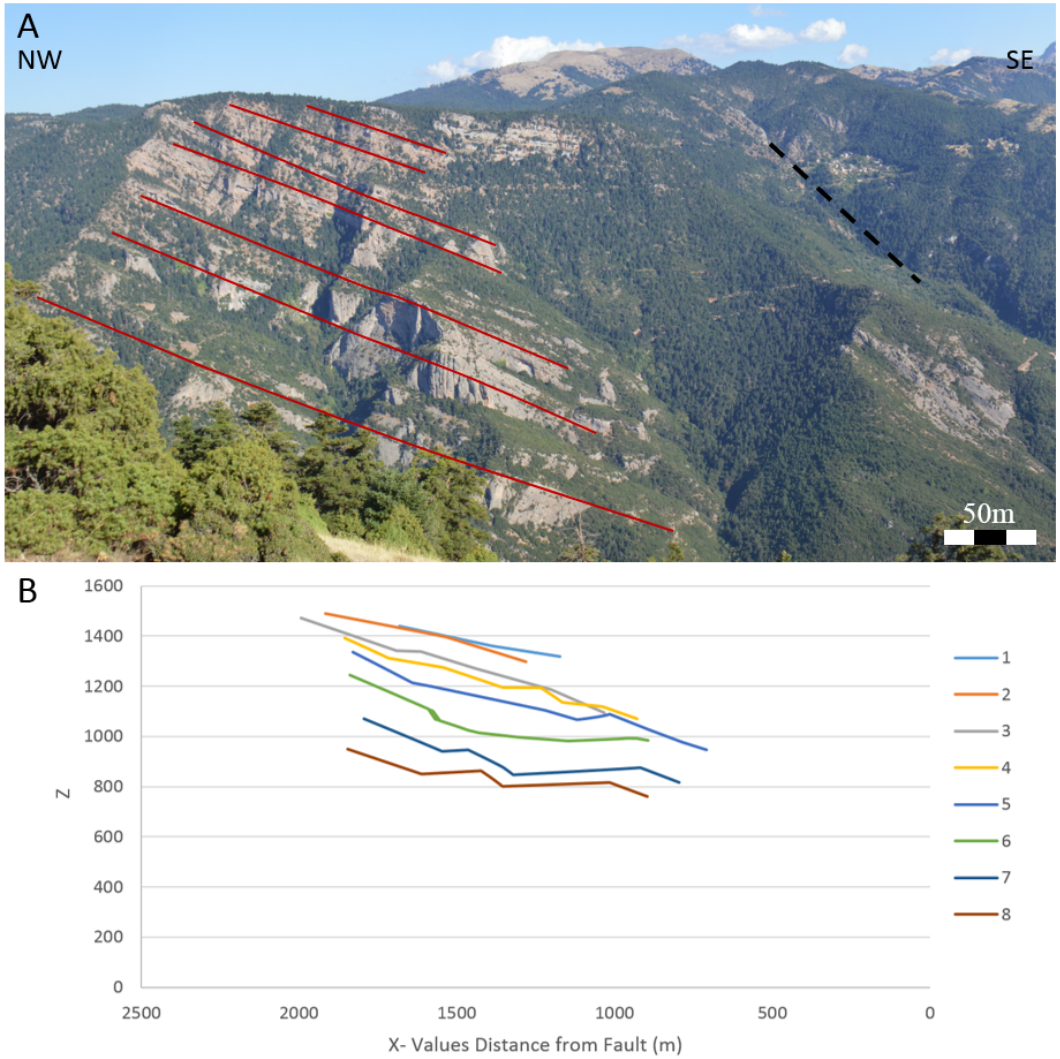


**Figure 4.11:** Figure A illustrates seven bedding lines interpreted from the Roghi outcrop. Figure B represents results from bedding line plot, illustrating similar bedding lines to the LiDAR data interpretation. The location of Kerpini fault is highlighted with black dashed line in Figure A.

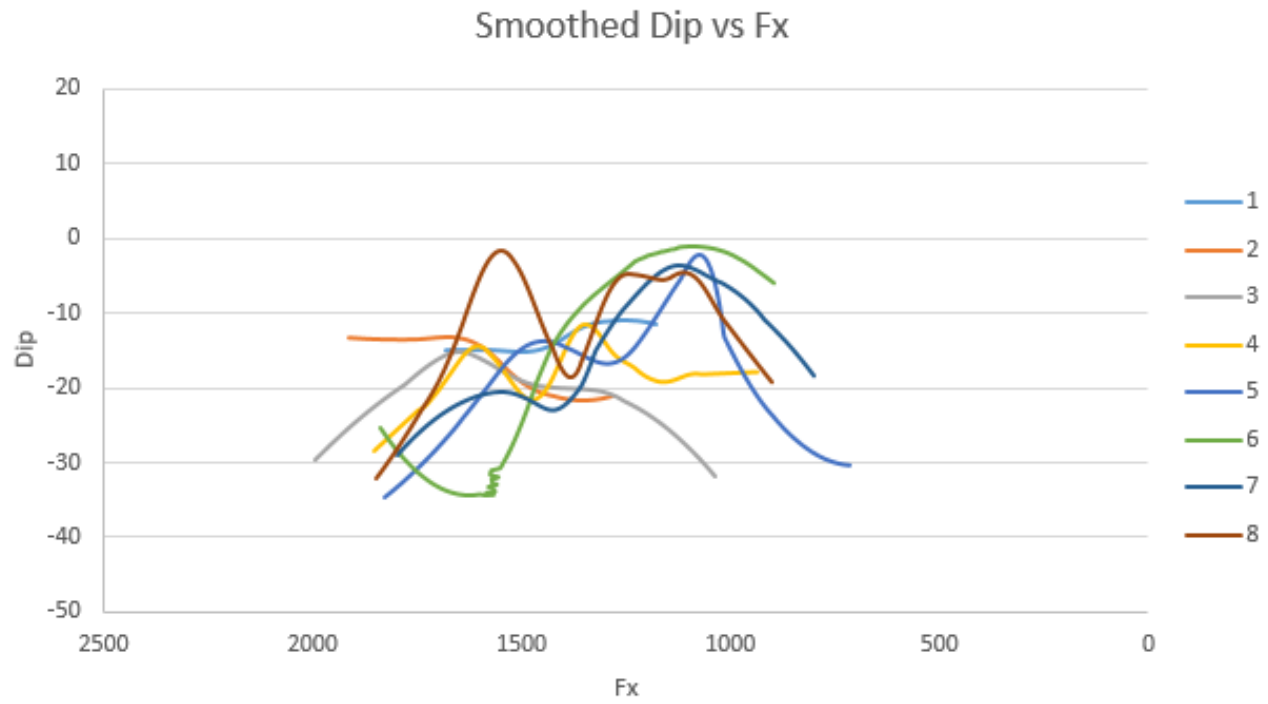


**Figure 4.12:** Structural analysis dip plot of the Roghi outcrop illustrating relatively uniform dip values. The dip plot display dip values plotted against $F_x$.

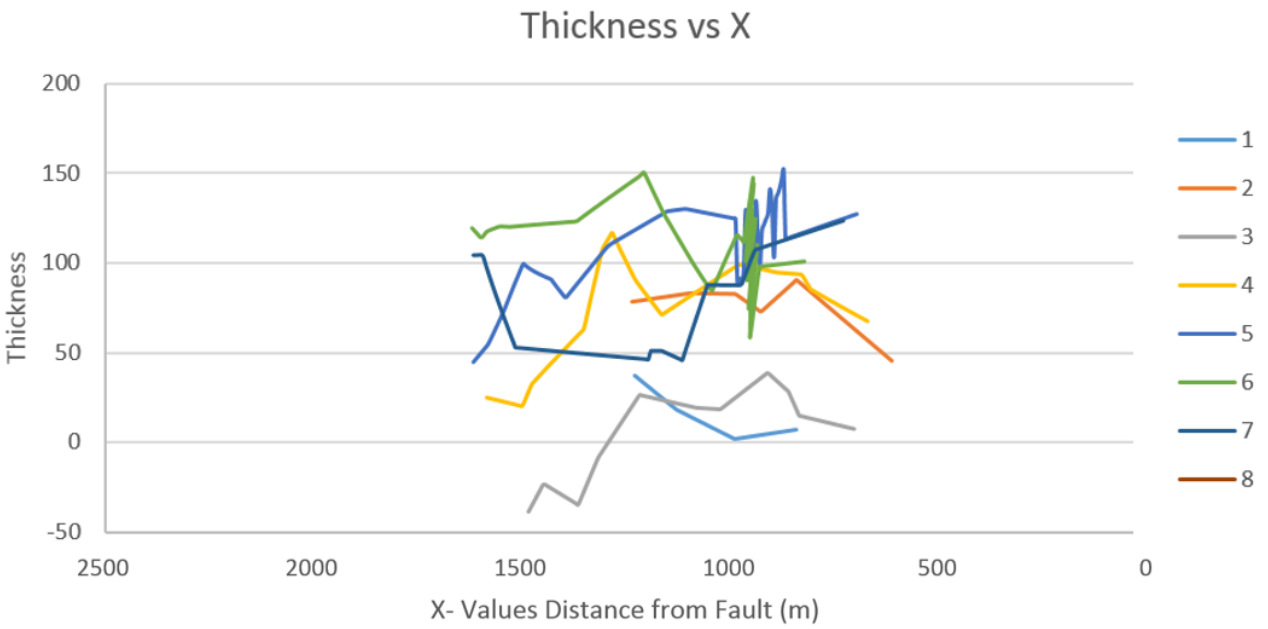


**Figure 4.13:** The bedding line thickness variation plot. The results are absent of extreme thickness variations.

| | Bedding Line nr. | Standard Deviation | |
|---|---|---|---|
| | | Dip | Thickness |
| Roghi | 1 | 1.86 | 10.19 |
| | 2 | 3.55 | 18.83 |
| | 3 | 4.26 | 21.27 |
| | 4 | 3.71 | 25.15 |
| | 5 | 8.85 | 21.50 |
| | 6 | 13.28 | 18.28 |
| | 7 | 7.54 | 27.83 |
| | 8 | 7.82 | N/A |

**Table 4.2:** Standard deviation of bedding line dip and thickness values for Roghi's structural analysis.

## 4.3 Vrachni

### 4.3.1 General Information

The outcrop of Vrachni extends from Souvardo town to the north to Ano Lousi to the south, located approximately 8 km to the east from the Kalavryta town (Figure 4.14). The Vrachni outcrop compose of conglomerate outcropping in the west and limestone basement in the east with an unconformity contact in the upper part of the outcrop (Figure 4.15). Due to the high vegetation coverage and lack of outcropping sediments, the outcrop has been ranked as moderate quality.

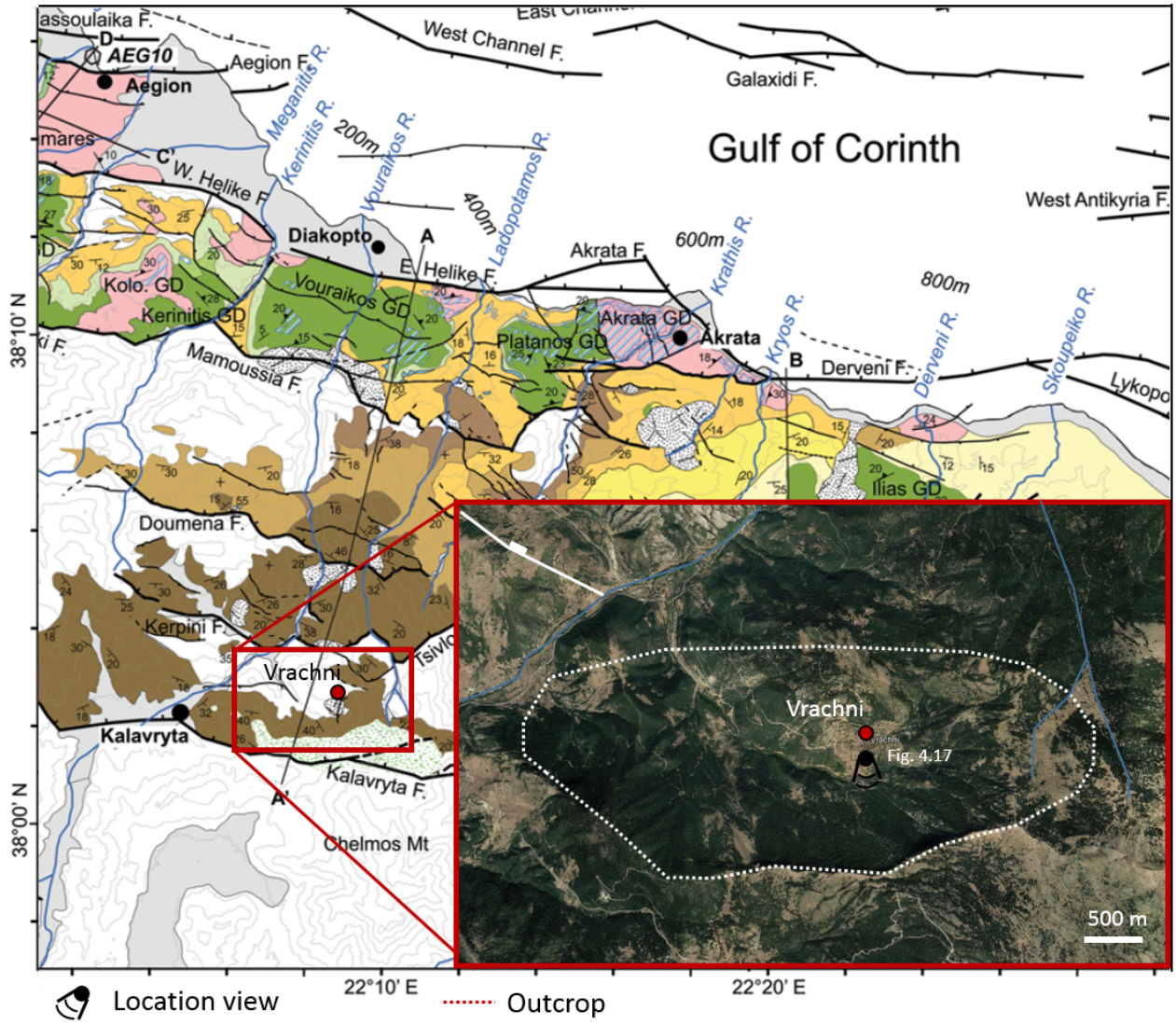


**Figure 4.14:** Map displaying location of Vrachni outcrop illustrating rivers highlighted in blue and faults in white. The top-view of the outcrop is displayed in a red rectangle. Location view of Figure 4.15 is indicated. Satellite imagery was retrieved from Google Earth Pro. Map is modified after Ford, Hemelsdael, et al. 2016.

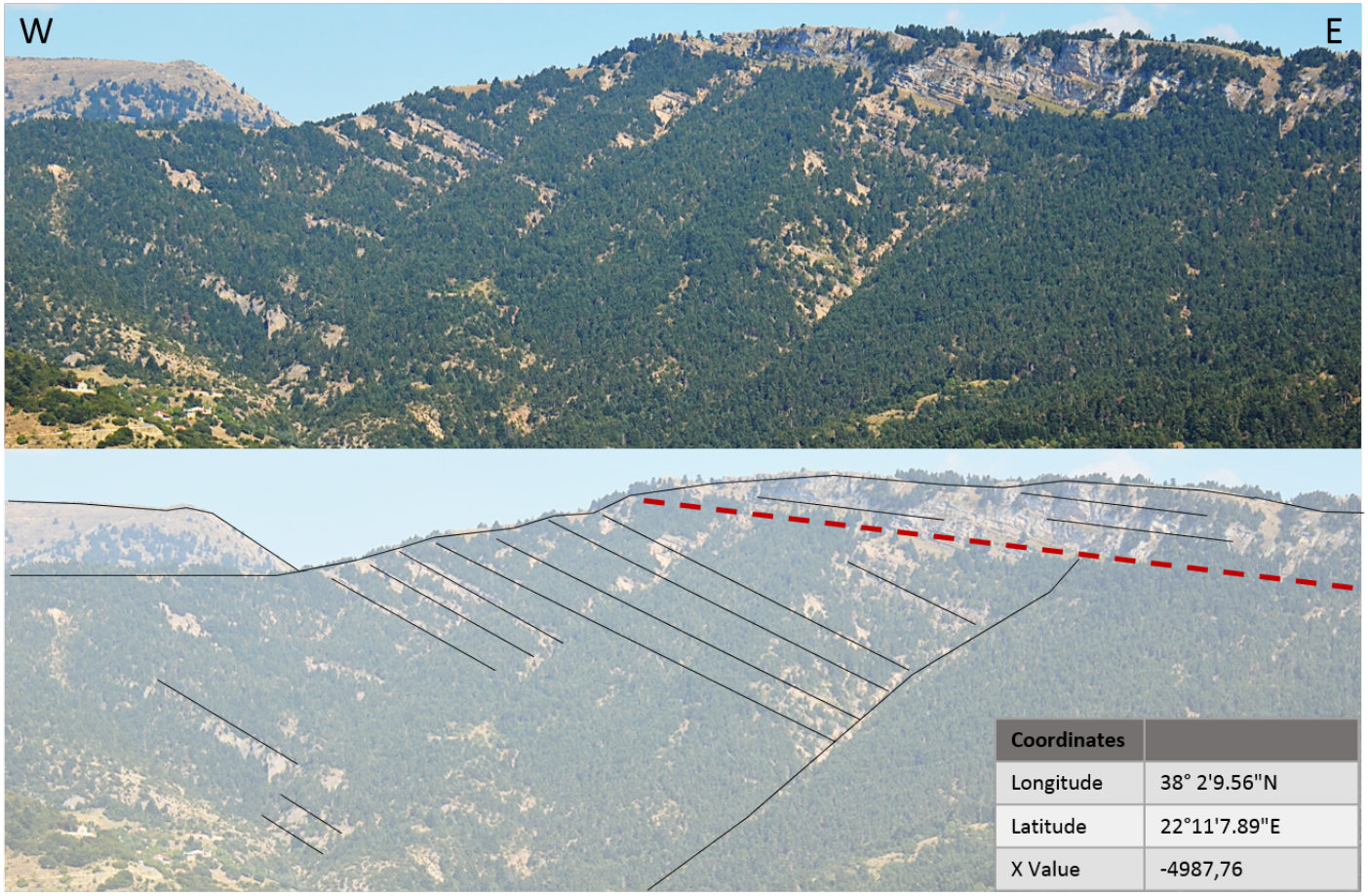


**Figure 4.15:** Vrachni outcrop bedding line interpretation carried out in the field. The red dashed line highlights the unconformity and the coordinate table indicates fault's location used as a reference point for structural analysis plot creation.

### 4.3.2 LiDAR Data

The acquired point-cloud of Vrachni area was assembled using 8 different data acquisition locations (Figure 4.16). The LiDAR data of the outcrop comprises of 90 497 410 points providing an opportunity to examine 11 km$^2$ area. Data coverage is limited due to the high amount of vegetation in the outcrops area.

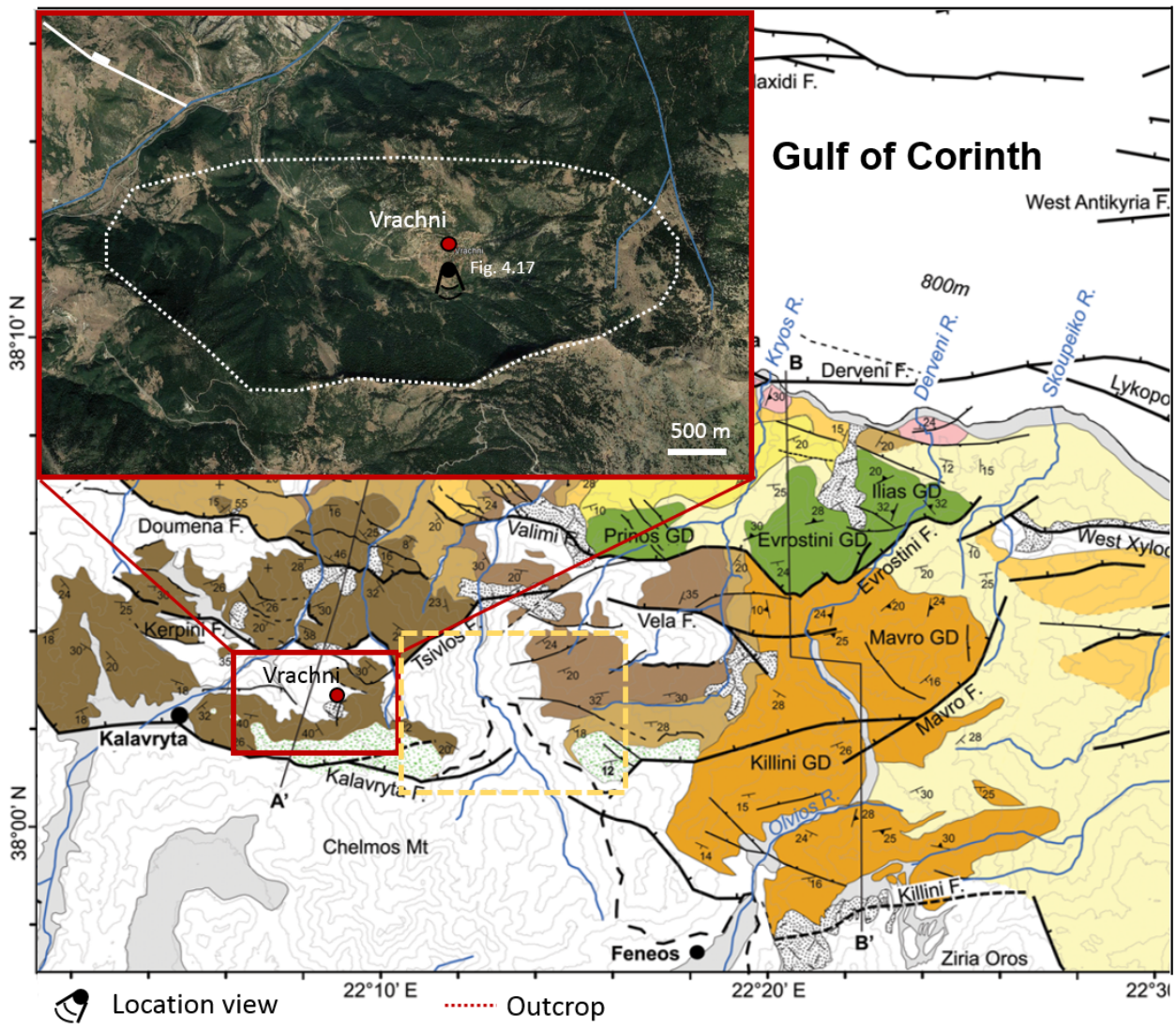


**Figure 4.16:** Map illustrating location of the Vrachni town, outcrop, scanning position and scanning range utilized for LiDAR field data acquisition. Location of Vrachni outcrop is highlighted in red and outcrop recommended for further syn-rift growth geometry investigation is highlighted in yellow.

### 4.3.3 Structural Analysis

Seven bedding lines were interpreted from Vrachni outcrop which truncate with the fault in the east. The plotted bedding lines exhibit overlapping and relatively fluctuation free data, in addition to some bedding lines not appearing as perfectly straight lines. Bedding lines display minor fluctuations, caused by outcrop walls irregularities. The overlapping features are induced by the visualization angle and vegetation cover of the outcrop, causing difficulties for the bedding line interpretation using LiDAR data (Figure 4.17). The results obtained from bedding line plots were validated with additional thickness and dip value and plot analysis. The dip variation plot exhibits high peaks in the bedding lines 2, 3, 4, 7 and 8 induced by line overlaps and slight oscillations originating from initial bedding line interpretation (Figure 4.18). The overlap induces changes in dip, in addition to fluctuations in thickness values. Generally, bedding line thicknesses decrease towards the fault, followed by value oscillation towards the west, as shown in the thickness plot of Vrachni outcrop (Figure 4.19). Thickness plot include two bedding lines displaying high bedding line thickness values (bedding lines 6 and 7), caused by a bigger gap between interpreted bedding lines, due to the thick vegetation cover in the lower part of the outcrop. Rest of the bedding lines display thickness value drop until approximately $F_x = 7700$, followed by an increase. Bedding lines 2, 5 and 7 display thickness decrease towards the location of the fault. Additionally, bedding line 8 exhibits value irregularities at $F_x = 7400$ - 7500. If bedding line overlapping was removed, minor value fluctuations would only appear in thickness and dip plots, not indicative of thickness and dip increases and corresponding to the field interpretation. Additionally, thickness plot includes negative values induced by the bedding line overlap.

Vrachni bedding line standard deviation values indicate relatively consistent and high quality dip value results apart of bedding line 5 illustrating the highest deviation of 5.96. Thickness values display higher standard deviation values (Figure 4.3). The result of bedding lines 5, 7 and 8 thicknesses deviate the most, with highest deviation value of 11.42 exhibited by bedding line 7. Furthermore, bedding line overlapping removed, would display minor value fluctuations in thickness and dip. By cause of nearly equal amount of bedding line thicknesses increasing and decreasing towards the fault in addition to the constant dip trend, growth geometry existence

is not indicative.

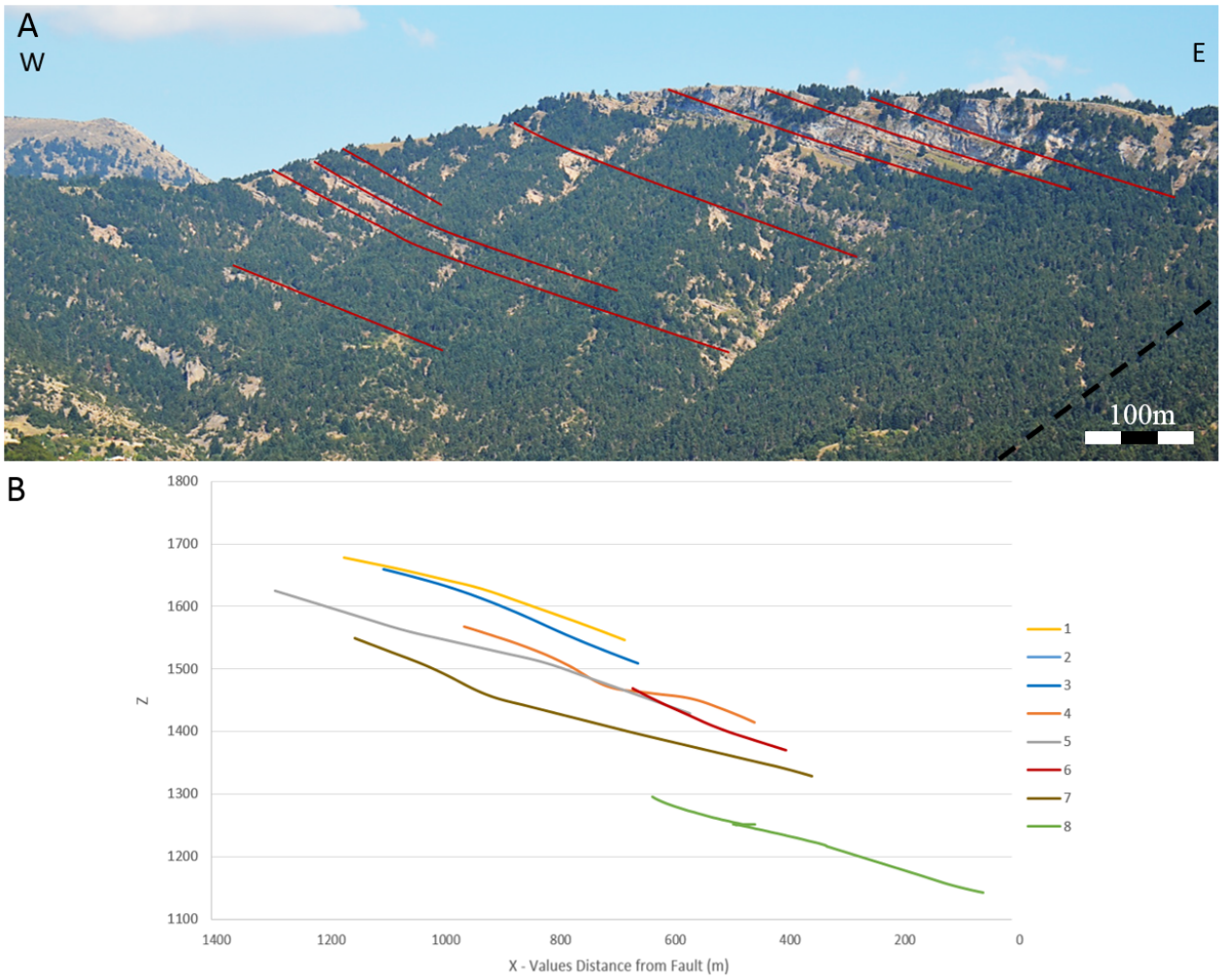


**Figure 4.17:** Figure A illustrate Vrachni outcrop and bedding lines interpreted based on LiDAR data. The fault used as a reference for X values. Figure B show the plot illustrating the corresponding bedding line Z values against $F_x$ values.

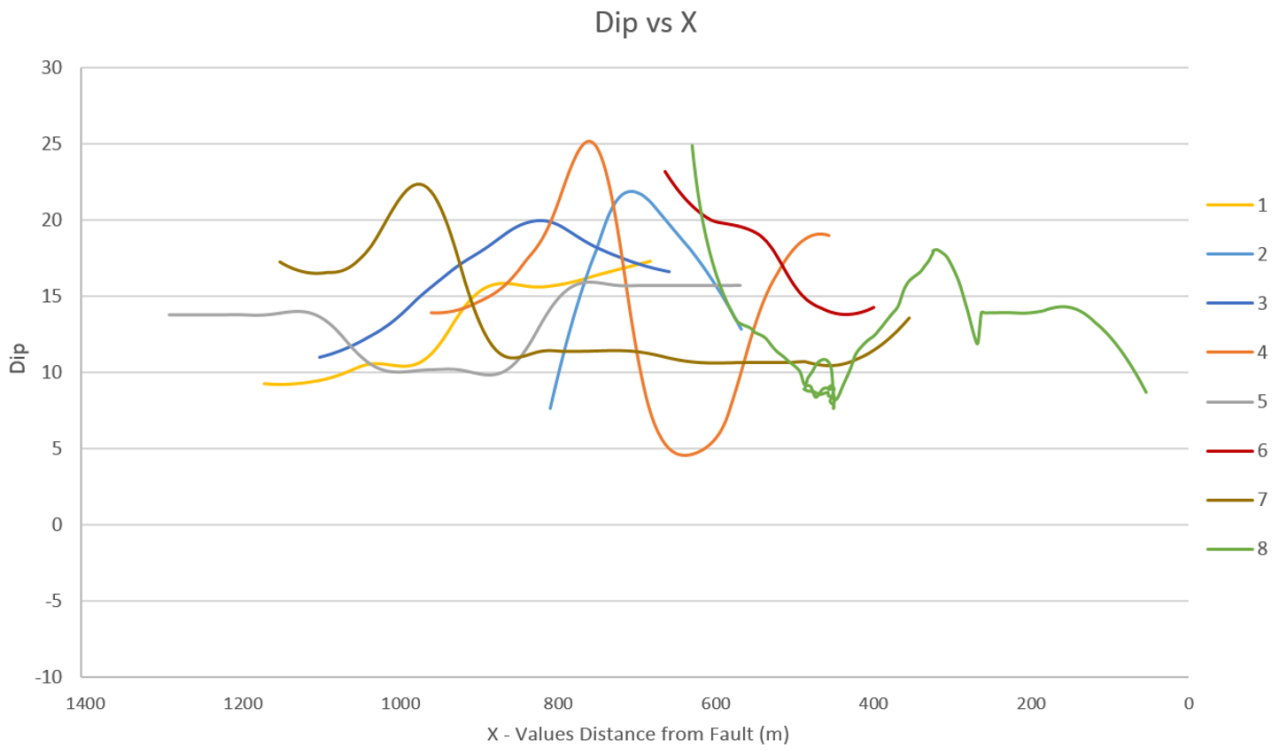


**Figure 4.18:** Structural analysis dip variation plot of Vrachni outcrop.

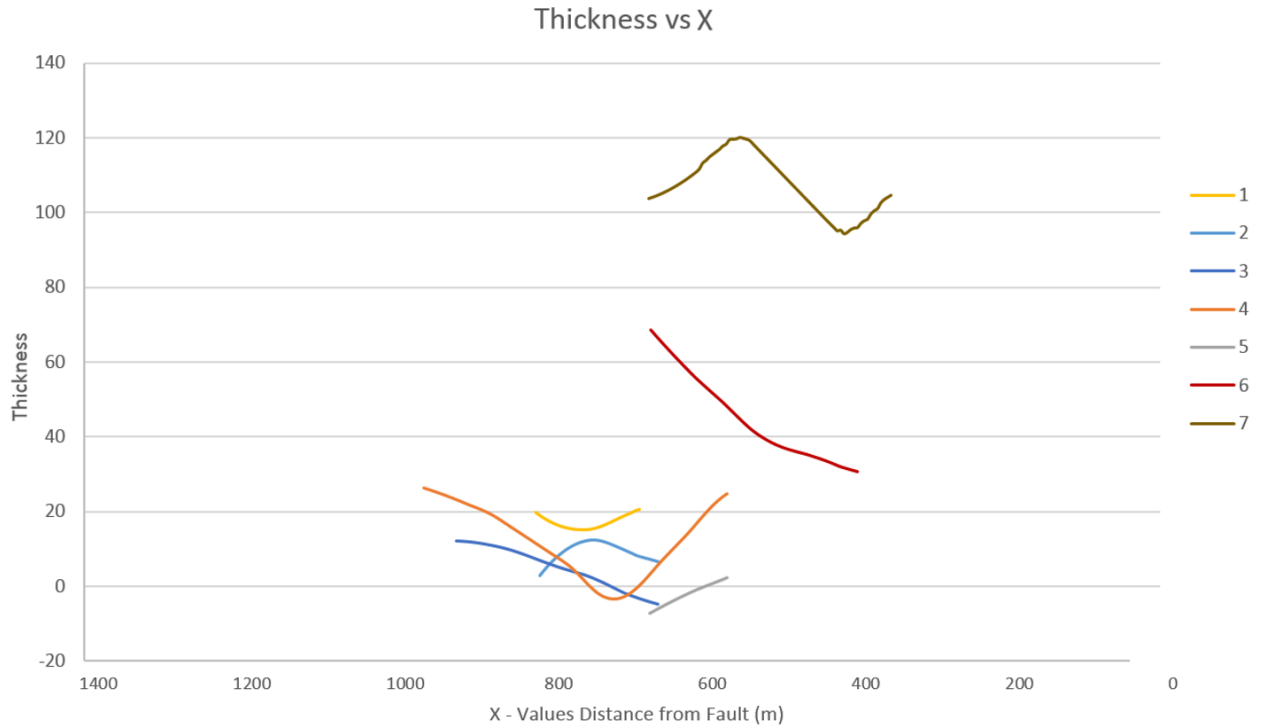


**Figure 4.19:** Thickness variation plot of Vrachni outcrop.

| | Bedding Line nr. | Standard Deviation | |
|---|---|---|---|
| | | Dip | Thickness |
| Vrachni | 1 | 2.96 | 1.70 |
| | 2 | 3.69 | 2.56 |
| | 3 | 2.80 | 5.40 |
| | 4 | 1.46 | 5.79 |
| | 5 | 5.96 | 9.43 |
| | 6 | 2.21 | 2.85 |
| | 7 | 3.00 | 11.42 |
| | 8 | 3.67 | 7.83 |
| | 9 | 3.51 | N/A |

**Table 4.3:** Standard deviation of bedding line dip and thickness values for Vrachni structural analysis.

## 4.4 Monastery

### 4.4.1 General Information

The outcrop of Monastery was named after Spileo Monastery appearing on the southwestern edge of the outcrop. Monastery outcrop is situated northeast from the Roghi outcrop and approximately 12 km northeast from the Kalavryta town (Figure 4.20). The geological overview indicates several normal faults uplifting limestone basement against conglomerate beds and inducing an unconformity in addition to two antithetic faults creating a graben structure (Figure 4.21). The field observations support Oppedal (2017) interpretation of the area. Additionally, monastery outcrop is rated as one of the poorest data qualities based on the lowest amount of bedding lines interpreted and lack of LiDAR data.

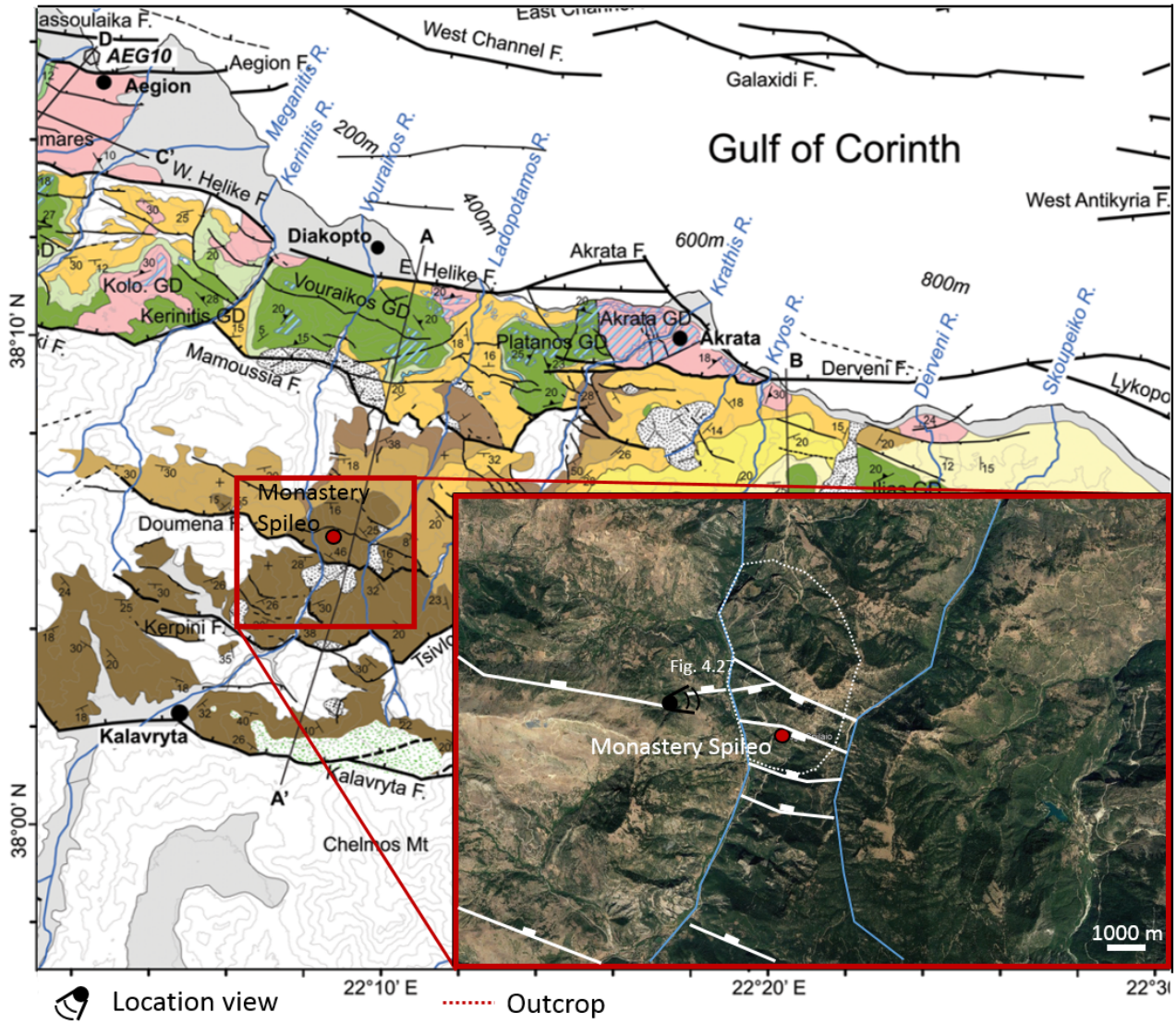


**Figure 4.20:** Map displaying location of Monastery outcrop illustrating rivers highlighted in blue and faults in white. The top-view of the outcrop is displayed in a red rectangle. Location view of Figure 4.21 is indicated. Satellite imagery was retrieved from Google Earth Pro. Map is modified after Ford, Hemelsdael, et al. 2016.

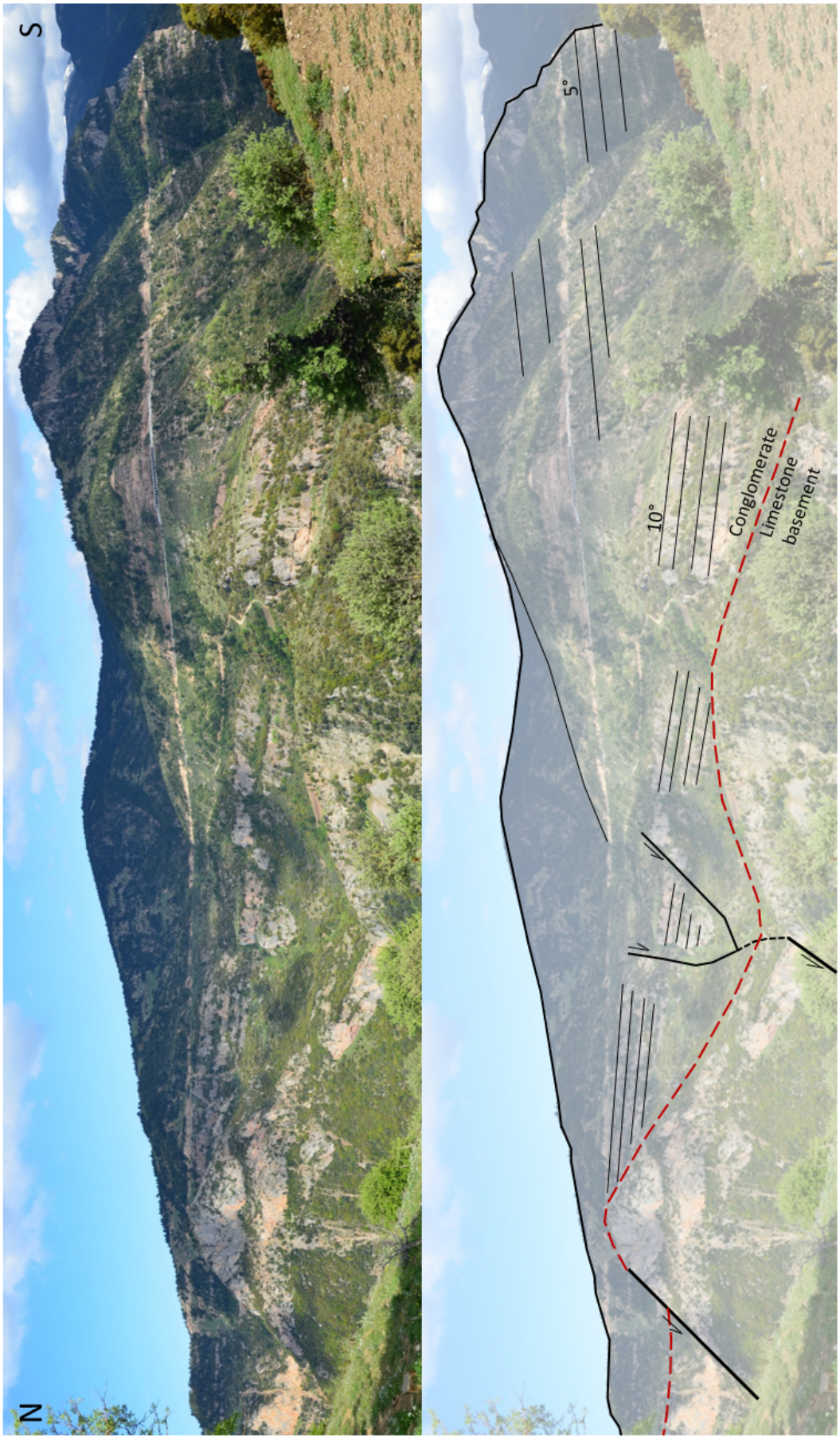


**Figure 4.21:** Field interpretation of the Monastery outcrop, displaying several normal faults and an unconformity highlighted in red.

### 4.4.2 Structural Analysis

Structural analysis results of Monastery outcrop are based on field and photogrammetry data, utilizing six bedding lines for structural analysis plot generation. The created bedding line plot displays relatively parallel bedding lines with fluctuations appearing due to the fault intersection with bedding lines 1 and 2 (Figure 4.22). The fluctuations consistently appear in thickness and dip plots at corresponding $F_x$ values, while the bedding lines non-intersecting with faults display consistent thicknesses absent of fluctuations, proving fault intersection influence on the bedding lines.

The investigation of the bedding line dip variation plot results in a common anticlinal trend of dip value decrease followed by an increase (Figure 4.23). The bedding line thickness plot exhibit more fluctuating trend compared to the dip variation plot, displaying thickness increase and decrease at points of intersection. The intersection points in the thickness plot are not appearing at same locations caused by the dip and inclination of the fault (Figure 4.24). The northeastern fault block thickness values are lower than the southwestern block. Additionally, bedding line thickness and dip results demonstrate relatively low standard deviation values indicating high data quality and structural analysis results. Bedding line 3 exhibit the highest dip deviation and bedding line 6 shows the highest thickness deviation (Table 4.4).

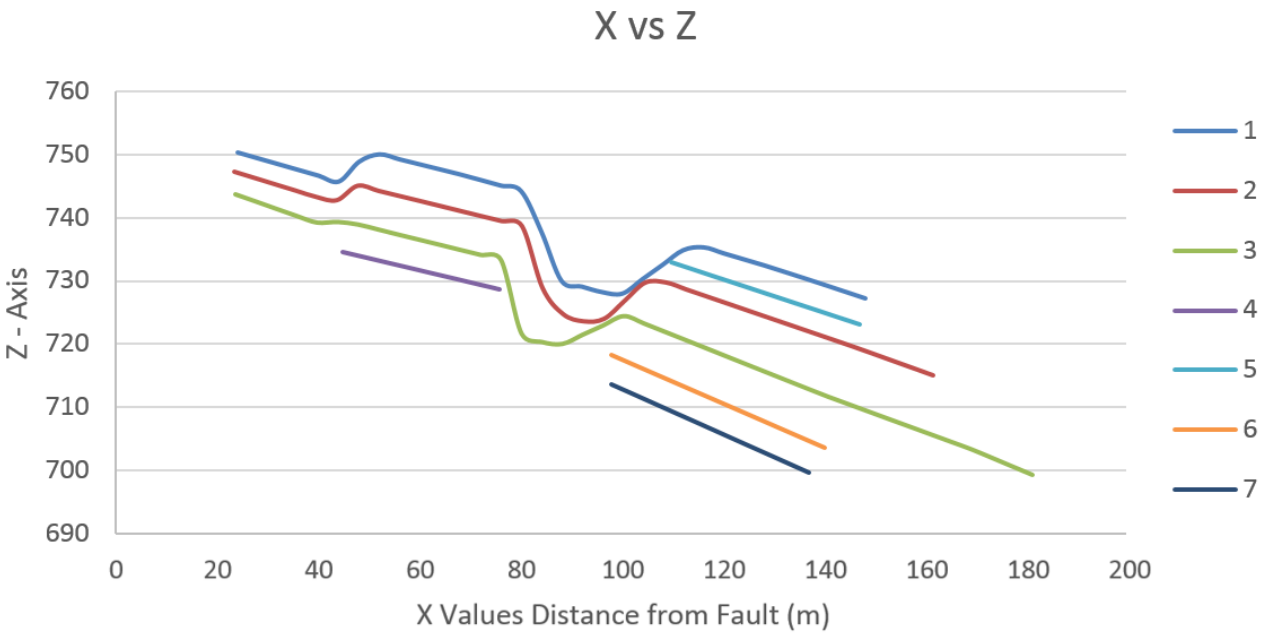


**Figure 4.22:** Bedding line plot of Monastery outcrop.

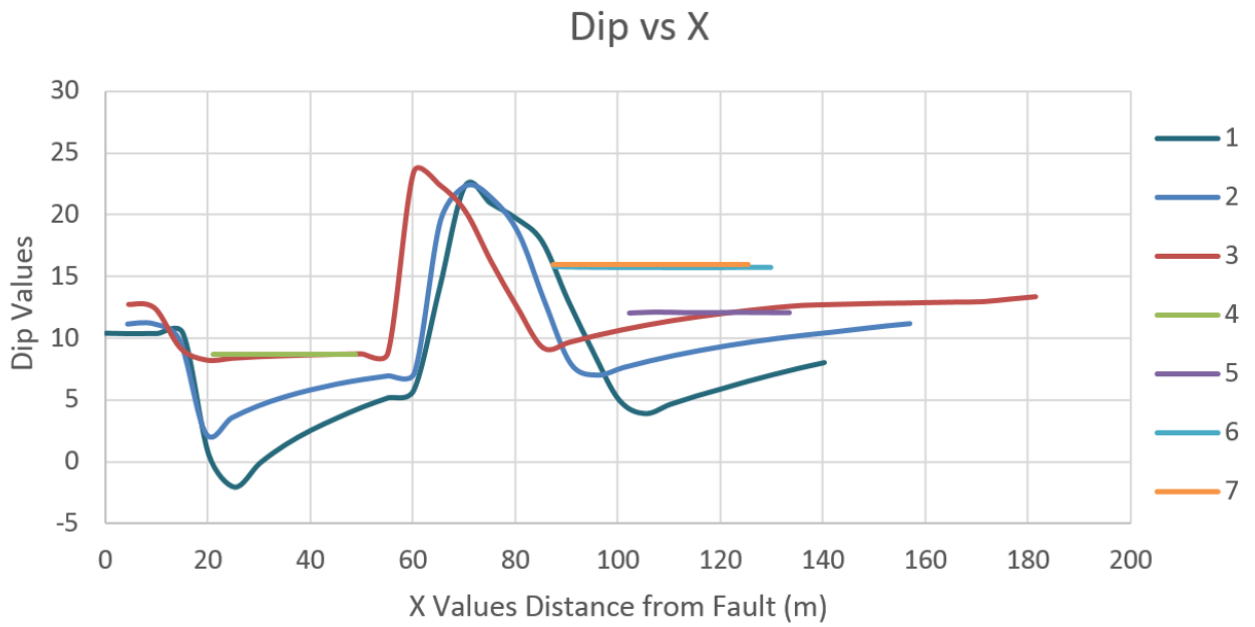


**Figure 4.23:** Structural analysis results of Monastery dip values.

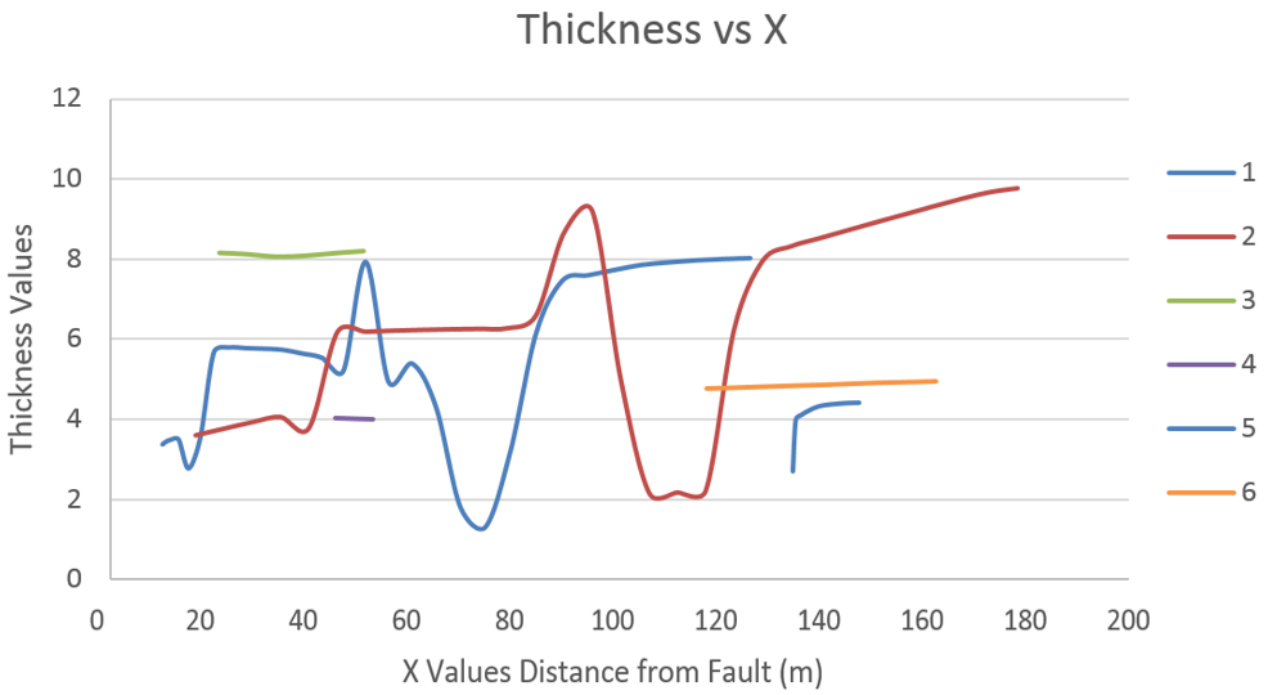


**Figure 4.24:** Monastery thickness variation plot.

| | Bedding Line nr. | Standard Deviation | |
|---|---|---|---|
| | | Dip | Thickness |
| Monastery | 1 | 6.18 | 1.97 |
| | 2 | 4.84 | 3.06 |
| | 3 | 8.33 | 0.43 |
| | 4 | 3.28 | 0.05 |
| | 5 | 4.03 | 0.52 |
| | 6 | 4.96 | 4.77 |
| | 7 | 5.05 | N/A |

**Table 4.4:** Standard deviation of bedding line dip and thickness values for Monastery structural analysis.

## 4.5 Roghi West

Roghi West outcrop is located near the Roghi town, west from Roghi outcrop (Figure 4.25). Roghi West outcrop was investigated using field data only. The outcrop appears approximately 12 km northeast from the Kalavryta town and display two normal faults down-throwing syn-rift sediments (Figure 4.26). Figure 4.26 displays viewing angle along the strike line, illustrating true thickness and dip results. The outcropping syn-rift sediments exhibit constant bed thickness and dip. Field observations of the outcrop bedding lines are not supporting Sigmundstad's (2016) research concluding in growth geometries.

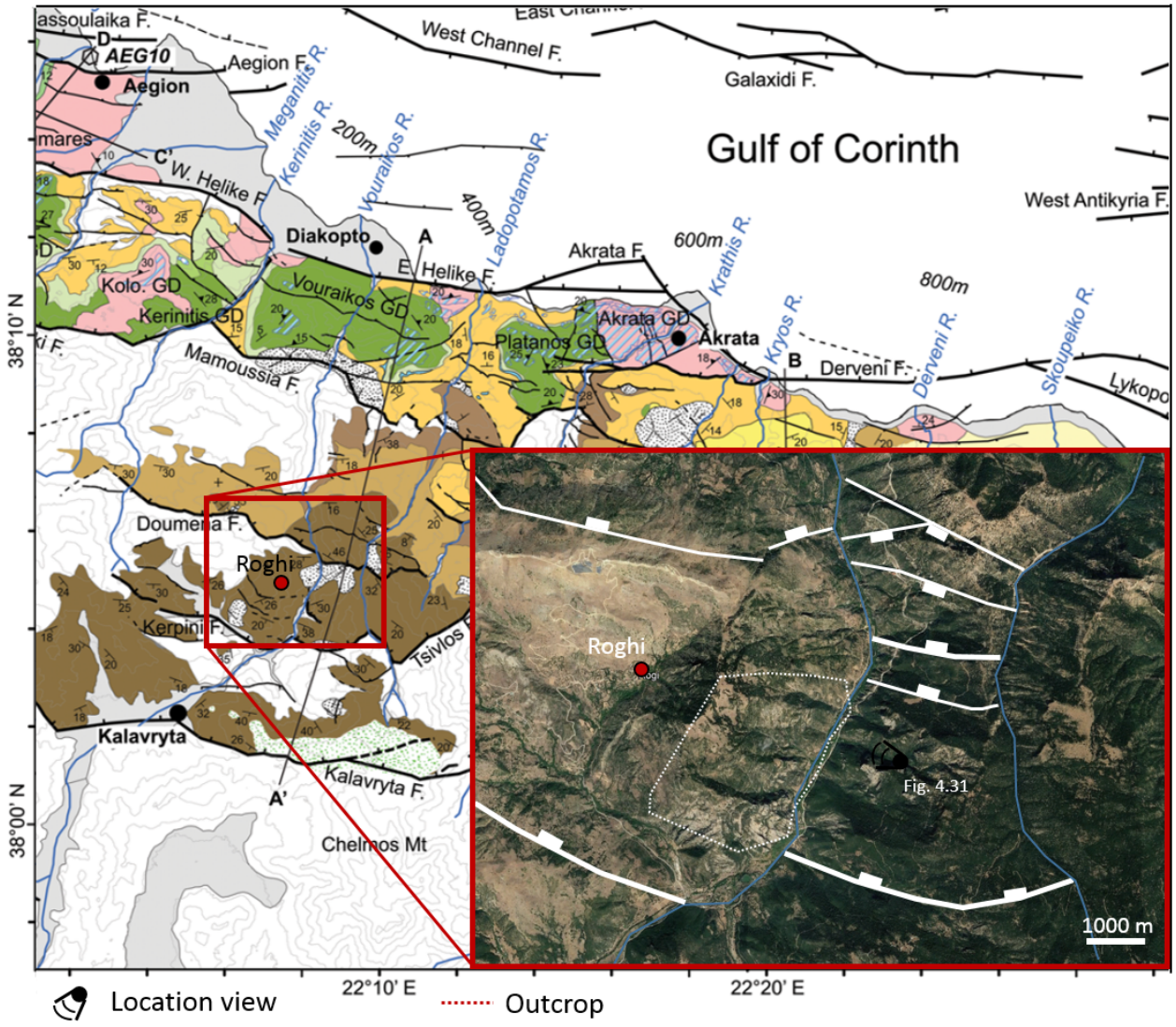


**Figure 4.25:** Map displaying location of Roghi Mountain outcrop illustrating rivers highlighted in blue and faults in white. The top-view of the outcrop is displayed in a red rectangle. Location view of Figure 4.26 is indicated. Satellite imagery was retrieved from Google Earth Pro. Map is modified after Ford, Hemelsdael, et al. 2016.


**Figure 4.26:** Field interpretation of the Roghi Mountain outcrop, displaying two normal faults and bedding lines highlighted in black.

## 4.6 Summary

The summary of structural analysis results are assembled in the Table 4.5.

| Outcrop | Data (Software) | Bedding Line Plot | Thickness Plot | Dip Plot | Bedding Line Nr. |
|---|---|---|---|---|---|
| Lapanagoi | LiDAR (Riscan Pro) | • Constant thickness<br>• Constant dip<br>• Minor fluctuations caused by outcrop irregularities | • Relatively constant thickness<br>• Fluctuations caused by outcrop irregularities<br>• One bedding line display increasing thickness values | • Relatively constant dip<br>• Fluctuations caused by outcrop irregularities | 10 |
| Roghi | LiDAR (Riscan Pro) | • Constant thickness<br>• Constant dip<br>• Minor fluctuations<br>• Bedding line overlaps | • Relatively constant thickness<br>• Fluctuations caused by outcrop irregularities<br>• Negative values of one bedding line caused by bedding line overlap | • Relatively constant dip<br>• Fluctuations caused by outcrop irregularities | 8 |
| Vrachni | LiDAR (Riscan Pro) | • Constant thickness<br>• Constant dip<br>• Minor fluctuations<br>• Bedding line overlaps | • Relatively constant thickness<br>• Minor fluctuations caused by outcrop irregularities<br>• Two bedding lines indicate higher thickness values | • Relatively constant dip<br>• Fluctuations caused by outcrop irregularities | 8 |
| Kefalari East | Field (Petrel and Agisoft) | • Constant thickness<br>• Constant dip<br>• Minor fluctuations | • Relatively constant thickness<br>• Minor fluctuations<br>• One bedding line indicate higher thickness values | • Relatively constant dip<br>• Fluctuations caused by outcrop irregularities | 8 |
| Monastery | Field (Petrel and Agisoft) | • Constant thickness<br>• Constant dip<br>• Fluctuations due to intersection with 2 faults | • Constant thickness<br>• Two fluctuating lines due to intersection with 2 faults | • Relatively constant dip<br>• Fluctuations caused by fault intersection | 7 |

**Table 4.5:** The summary of structural analysis.

## 4.7 Study Area B

The investigated northern area displays constant thickness and dip of the syn-rift packages in the field. However, Gawthorpe, Leeder et al. (2018) propose syn-rift sediment indicating characteristic growth geometry features in the area, in the contrast to the cross-section displaying packages with constant thicknesses and dip values (Figure 4.27). The lack of characteristic growth geometry features in the cross-section is not discussed in the paper.

In order to assess if growth geometry existence in the area is true, numerous outcrops mentioned in Gawthorpe, Leeder et al. (2018) research have been examined. Kefalari East delta was examined in most detail with structural bedding line analysis applied, followed by Kefalari West, Kyllini and Mavro deltas investigated only in the field. The Xylocastro and Amphithea outcrops were hardly accessible and, therefore, were investigated from far distance.

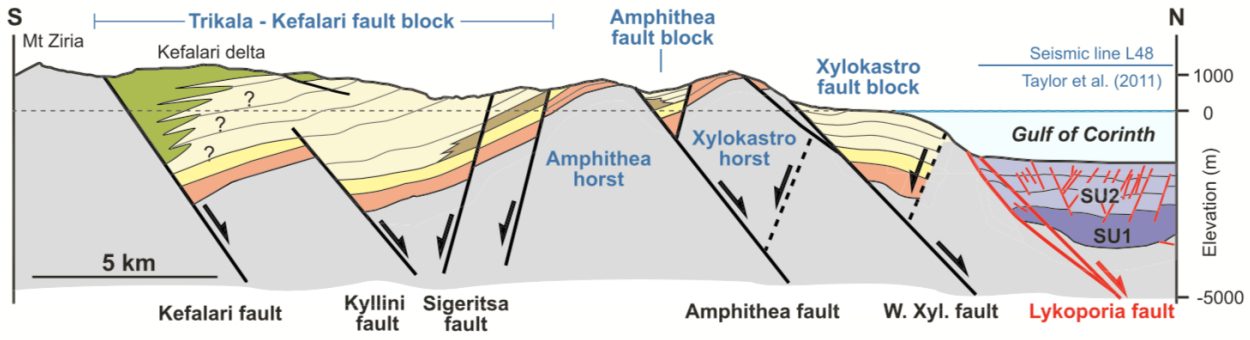


**Figure 4.27:** Conceptual cross-section indicating constant thickness and dip values of syn-rift packages (Gawthorpe, Leeder, et al. 2018).

### 4.7.1 Kefalari East

#### General Information

The Kefalari East (Kefalari E) outcrop is named after the nearest town Kefalari, located approximately 38 km northeast from the Kalavryta town (Figure 4.28). The outcrop comprise of conglomerate with eight bedding lines interpreted for the structural analysis. The bedding line interpretation of the outcrop is based on field data and photographs, supplemented by 3D visual outcrops view achieved with photogrammetry (Figure 4.29). Kefalari E outcrop's field data and photographs are based on images acquired from various viewing angles, portraying

bedding lines along the strike (Figure 4.30) and perpendicular to the strike line (Figure 4.29). Lack of the bedding line connectivity in the lower part of the outcrop points towards fluvial channel deposition system, although, according to Gawthorpe et al. (2018) Kefalari E outcrop originates from deltaic depositional environment, but topsets, bottomsets and foresets are not indicative in the outcrop.

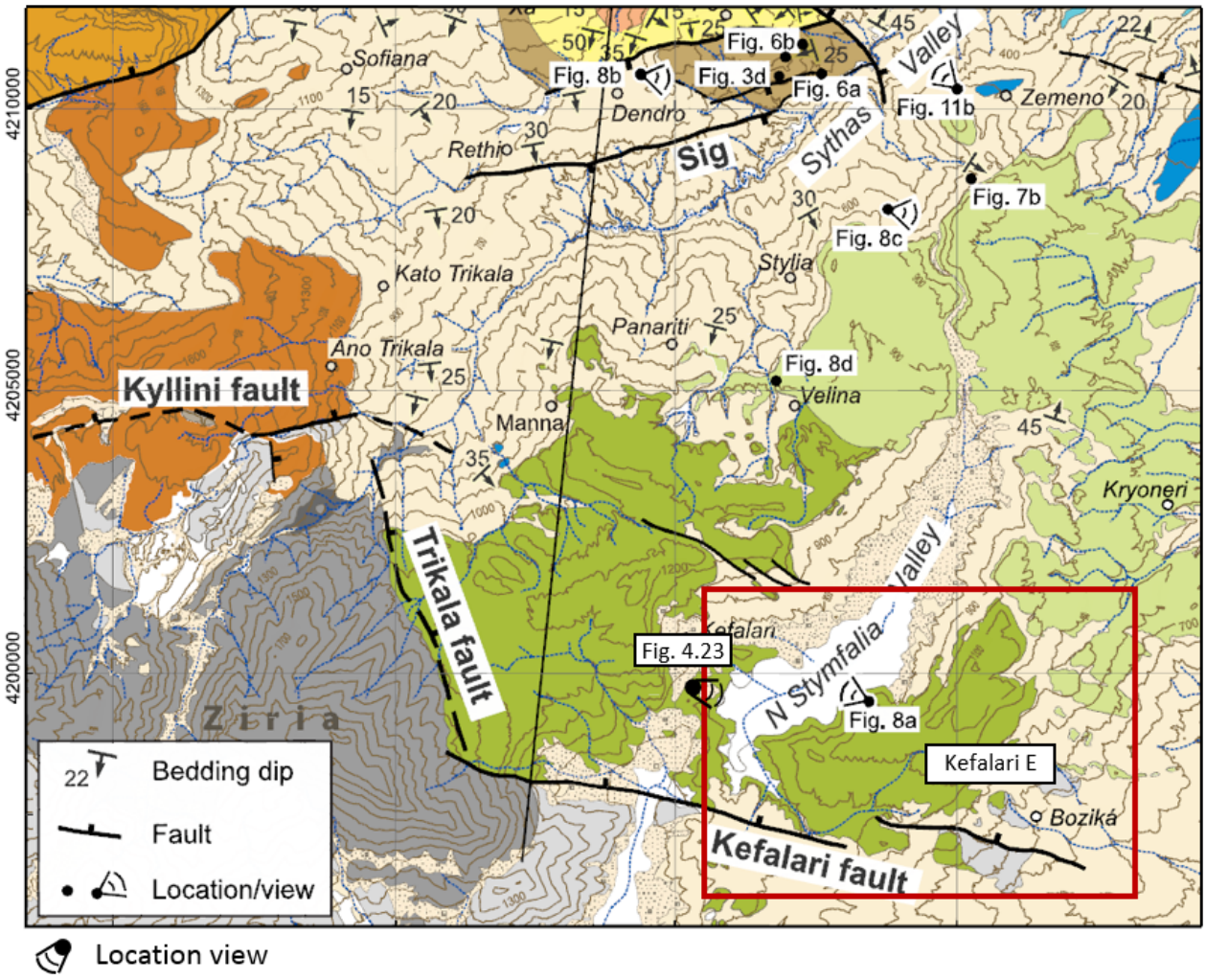


**Figure 4.28:** Map displaying location of Kefalari East outcrop illustrating rivers highlighted in blue and faults in white. The top-view of the outcrop is displayed in a red rectangle. Location view of Figure 4.29 is indicated. Satellite imagery was retrieved from Google Earth Pro. Map is modified after Ford, Hemelsdael, et al. 2016.

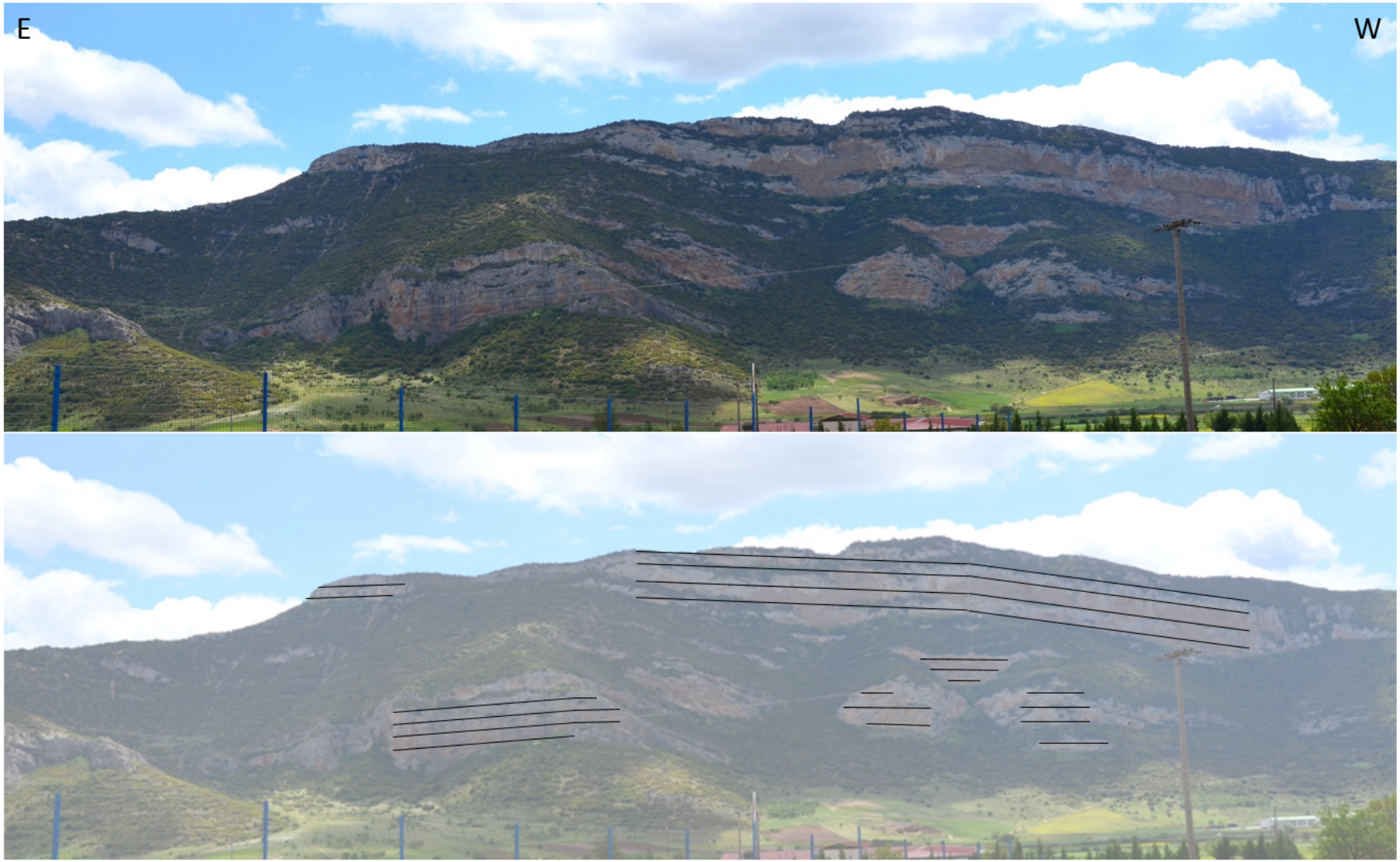


**Figure 4.29:** Kefalari East outcrop bedding line field's interpretation. Bedding lines are illustrated without angle distortion and highlighted in black.

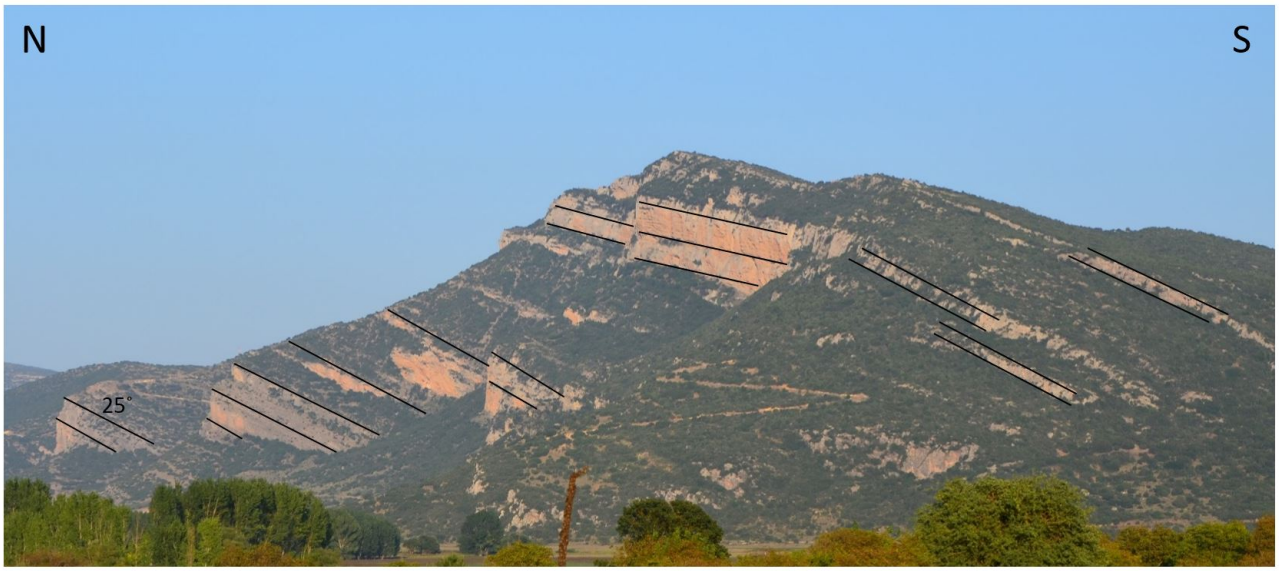


**Figure 4.30:** Kefalari East outcrop bedding line field's interpretation from a different viewing angle, portraying view of the outcrop along the strike line.

### Structural Analysis

Bedding line generation and interpretation of Kefalari East outcrop was based on photogrammetry and field data, utilized for structural analysis plot generation. Eight bedding lines were interpreted for Kefalari outcrop, displaying constant thickness and dip angles throughout the continuous bedding lines. All three plots display minor fluctuations only appearing at exact locations in all of the plots ($F_x$ = 150, 200, 225 and 250) (Figure 4.32), in the contrast to the highly fluctuating results of the outcrops containing LiDAR data. Bedding line plot for Kefalari outcrop display two sets of bedding lines - four bedding lines interpreted on the lower part of the outcrop and four on the upper part. The bedding lines were subdivided into two sets due to the interpretation angle on the image, causing the bedding line sets divergence in the plot (Figure 4.31).

Bedding lines indicate relatively constant dip throughout the outcrop exhibiting minor and insignificant value fluctuations, caused by the irregular outcrops wall and interpretation angle. The thickness plot displays relatively constant thickness values with minor value variations of 2-3 degrees (Figure 4.33). Bedding line 4 exhibits the highest thickness values, induced by the big gap between interpreted bedding lines. Thickness and dip plot bedding line values display low standard deviation rates, with bedding line 5 exhibiting largest deviation in thickness of

5.03 (Table 4.6). Therefore, the interpretation quality of the outcrop is of good quality and since the bedding lines display constant dip and thickness values, the outcrop is not indicative of thickness or dip increase throughout the section.

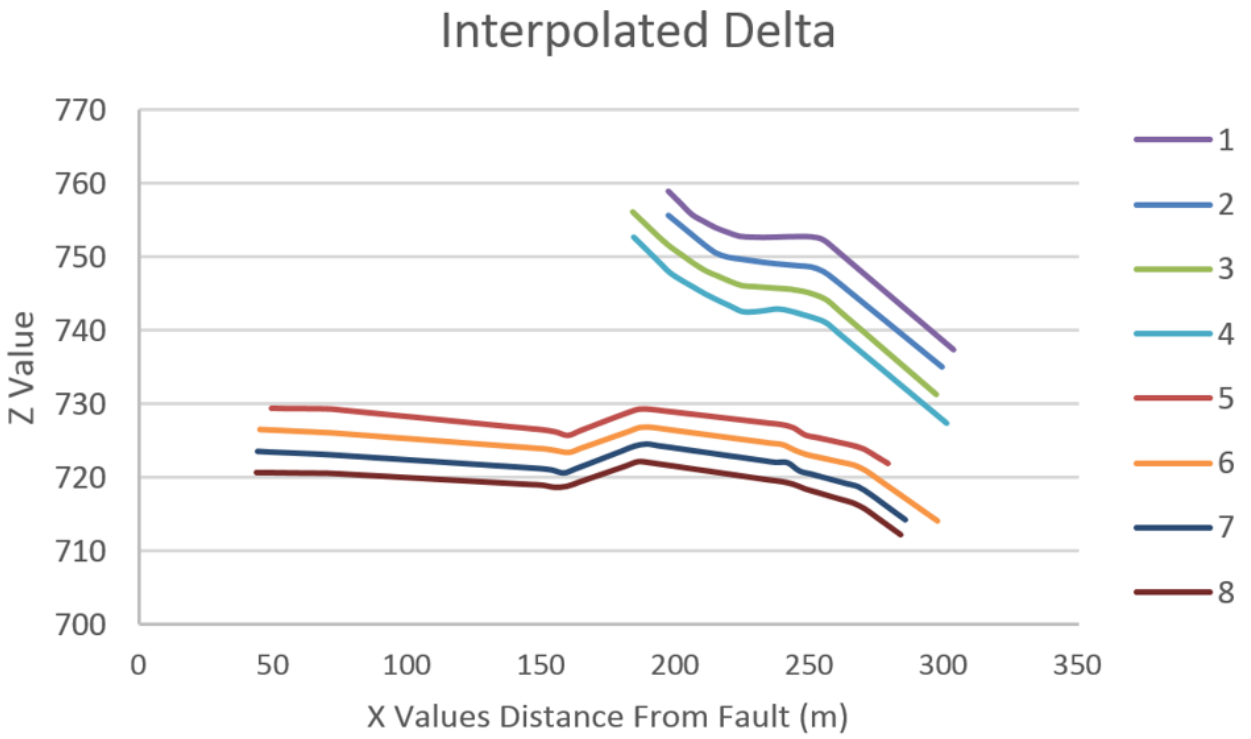


**Figure 4.31:** Structural analysis bedding line plot of Kefalari E outcrop.

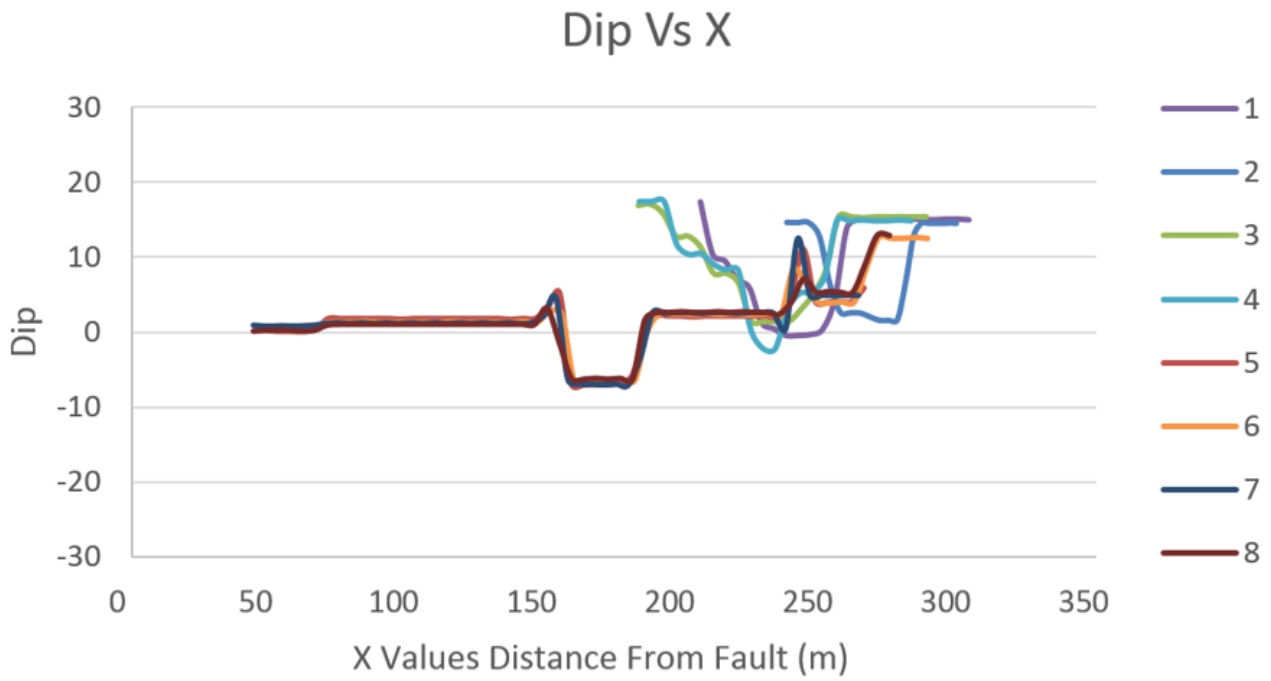


**Figure 4.32:** Dip plot of Kefalari E outcrop, dip values are plotted against $F_x$.

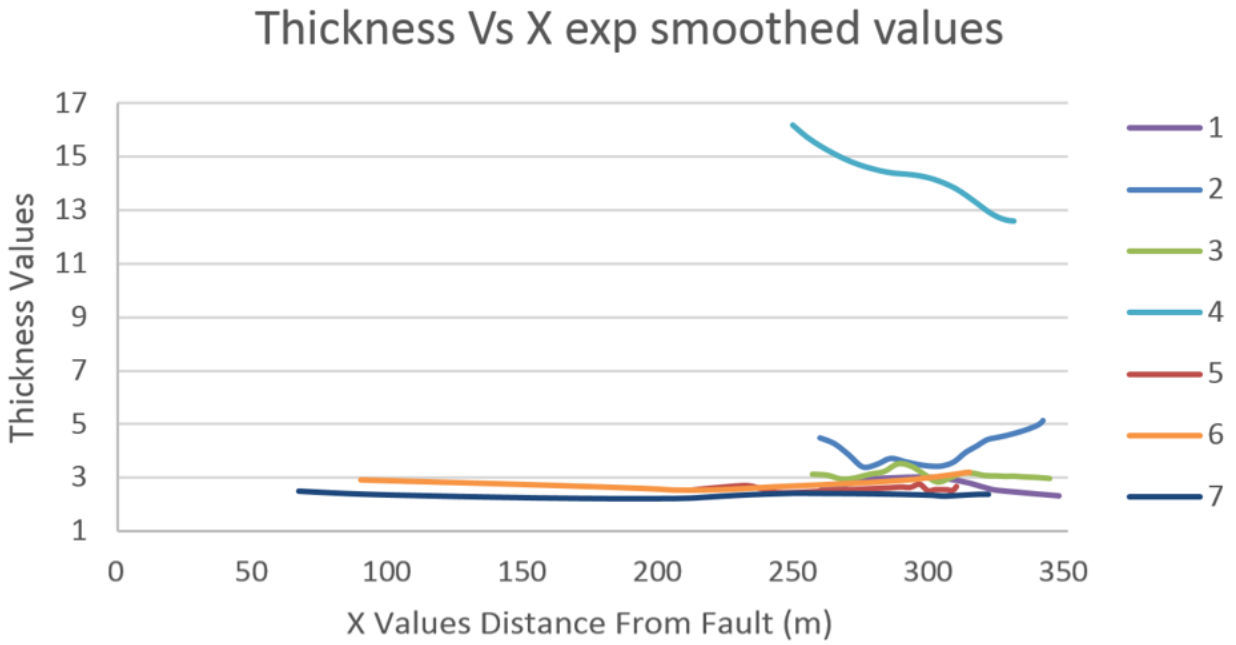


**Figure 4.33:** Kefalari E thickness plot, thickness values are plotted against $F_x$.

| | Bedding Line nr. | Standard Deviation | |
|---|---|---|---|
| | | Dip | Thickness |
| Kefalari East | 1 | 2.48 | 0.63 |
| | 2 | 2.57 | 0.58 |
| | 3 | 2.54 | 0.15 |
| | 4 | 2.42 | 2.24 |
| | 5 | 1.36 | 5.03 |
| | 6 | 1.53 | 0.24 |
| | 7 | 2.18 | 0.18 |
| | 8 | 1.71 | N/A |

**Table 4.6:** Standard deviation of the bedding line dip and thickness values for Kefalari East structural analysis.

### 4.7.2 Kefalari West

The Kefalari West delta is truncated by Trikala fault in the west, against the metamorphosed limestone basement. The outcrop is influenced by two faults, down-throwing tilted sedimentary beds. An unconformity between tilted sedimentary beds towards NW and tilted beds towards SE were interpreted. The bedding lines interpreted in the field display no change in thickness and dip (Figure 4.34). Although, bedding lines are tilted in the opposite direction to the rotation, due to the angle of delta foreset and topset deposition.

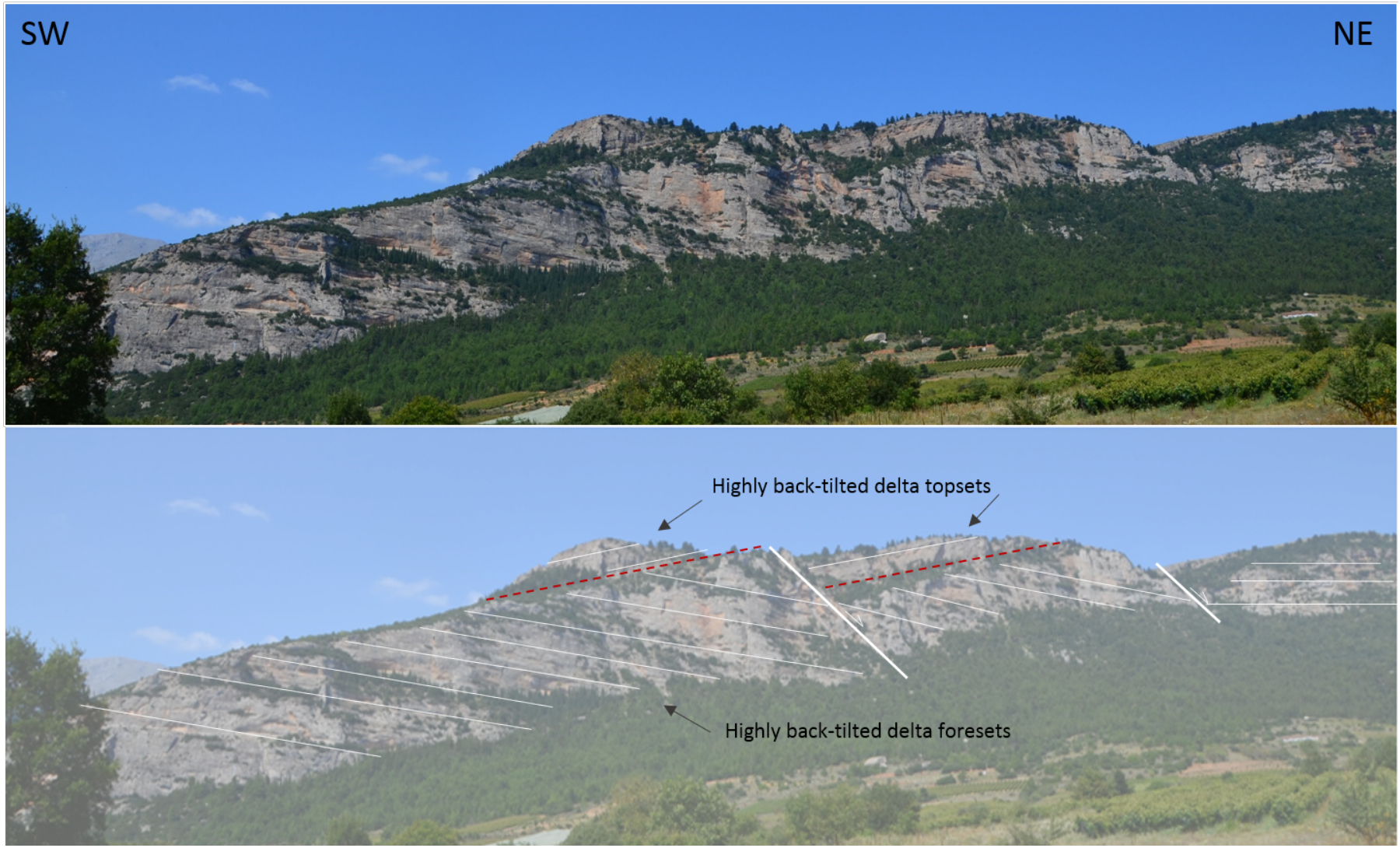


**Figure 4.34:** Kefalari West outcrop bedding line field's interpretation. The red dashed line marks the edge of the unconformity.

### 4.7.3 Kyllini

Kyllini outcrop appears on the western edge of the northern study area (Figure 1.3). The outcrop is comprised of several hundreds of meters of exposed conglomeratic sediments deposited on the hanging-wall of the normal fault (Figure 4.35). The true dip of the outcrop is hard to determine due to the hardly accessible angle in the field, therefore, the acquired photographs indicate a nonexistent increase in dip of 10° down-section. The dip is simulated by the irregular outcrop's wall stepping back due to the erosion. Additionally, the interpreted sedimentary packages lack thickness variations throughout. The outcrop lack clear characteristic delta features (topsets, foresets and bottomsets) in the field and, therefore, was not interpreted as delta in the contrast to the research of Gawthorpe, Leeder et al. (2018).

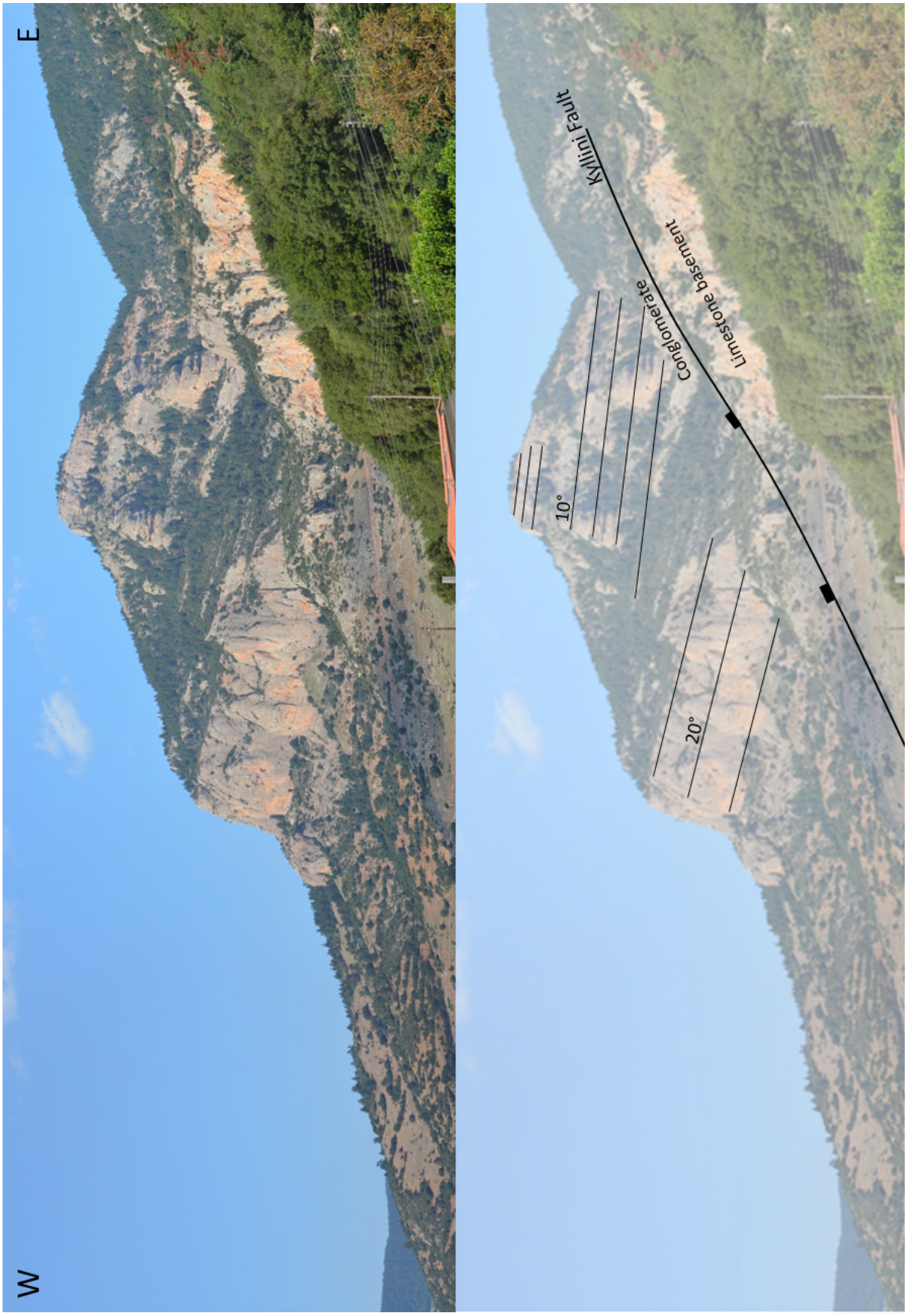


**Figure 4.35:** Field interpretation of the Kyllini outcrop displaying a fault contact between sediments and limestone basement.

### 4.7.4 Xylocastro and Amphithea

Xylocastro outcrop is located in the northern part of the Peloponnese area, near the Xylocastro town. Amphithea outcrop is situated south from Xylocastro town. Both outcrops were investigated from distance, due to the lack of accessibility and time limit. The Xylocastro and Amphithea outcrops display relatively flat sediments, absent of bedding thickness changes (Figure 4.36).

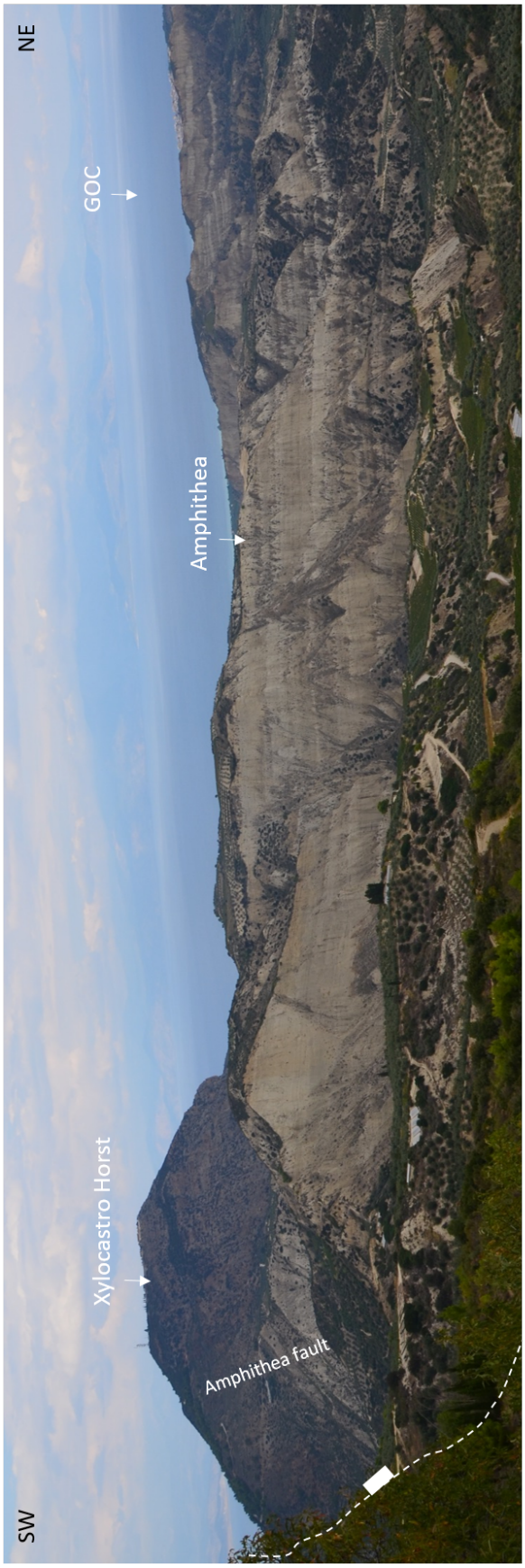


**Figure 4.36:** Field interpretation of the Xylocastro and Amphithea outcrops displaying a Amphithea fault and flat outcrop's deposits.

# Chapter 5

# Comparison with Analogues

The Corinthian rift has been widely used as an analogue for the NCS due to the rift's recent development and well preserved sediments. The GOC displays a lack of growth geometry structures in syn-rift packages, which might lead to GOC being a poor analogue for the NCS. Therefore, the main goal of this chapter is to compare syn-rift packages studied in the Gulf of Corinth with syn-rift packages studied in the NCS and evaluate differences and similarities between the two areas. In order to do so, LiDAR and field acquired data from the study area in Greece will be compared with seismic data from NCS.

## 5.1 Tectonic Events Comparison

Even though the GOC and NCS are rift basin analogues, both rifts have undergone different histories of tectonic events. The various events might have contrasting effects on both rifts in addition to the influence on sediment deposition and accommodation space creation (e.g, the Barents Sea inversion and the recent Corinthian Gulf's rifting activity). Hence, it is necessary to take the differences in the tectonic and sedimentary history of both rift systems into account, in order to perform an accurate comparison. North Sea represents the southern part of the NCS and is dominated by rotated fault blocks, relay ramps and sub-platforms structural features. These major structural features might have a strong impact on basin configuration and sediment distribution in the basin (Faleide et al. 2010). The continental margin of Norwegian Sea is located in the middle part of the NCS. This area was tectonically active from Carboniferous to

Late Pliocene experiencing long periods of rifting, extension and major volcanism in addition to the subsequent Norwegian-Greenland sea-floor spreading (Brekke 2000). The northern area of NCS is represented by the Barents Sea, which is influenced by volcanism, regional uplift, strike-slip, inversion, salt structures in addition to the widespread extensional events (Faleide et al. 2010).

## 5.2 Analysis of Norwegian Continental Shelf

The analysis of NCS was carried out using six seismic lines located in the North Sea, Norwegian Sea and Barents Sea (Figure 5.1). Seismic lines were chosen from popular exploration areas dominated by typical rift features (e.g., grabens, half-grabens, normal faults and uplifted rift flanks). The seismic sections were interpreted focusing on the structural elements and syn-rift packages.

The A-A', B-B' and C-C' seismic lines are located in the northern part of the North Sea. The line A-A' crosses Lomre Terrace from NW-SE and cuts across the well known Troll petroleum field. The B-B' line appears north of the A-A' section in the Måløy Slope and represents structural elements of Gjøa field, while the C-C' line is situated west of the B-B' line and appears in Tampen Spur Basin and intersects the Snorre field (Table 5.1). Singular seismic line in the Norwegian Sea is D-D', located in the Halten Terrace near the Fenja petroleum exploration field. Seismic sections E-E' and F-F' are located in the southern part of the Barents Sea. Seismic line E-E' cuts across the Hammerfest Basin from NW-SE, crossing the Snøhvit gas field, while the F-F' seismic line starts in the Tromsø Basin and extends over to the Loppa High.

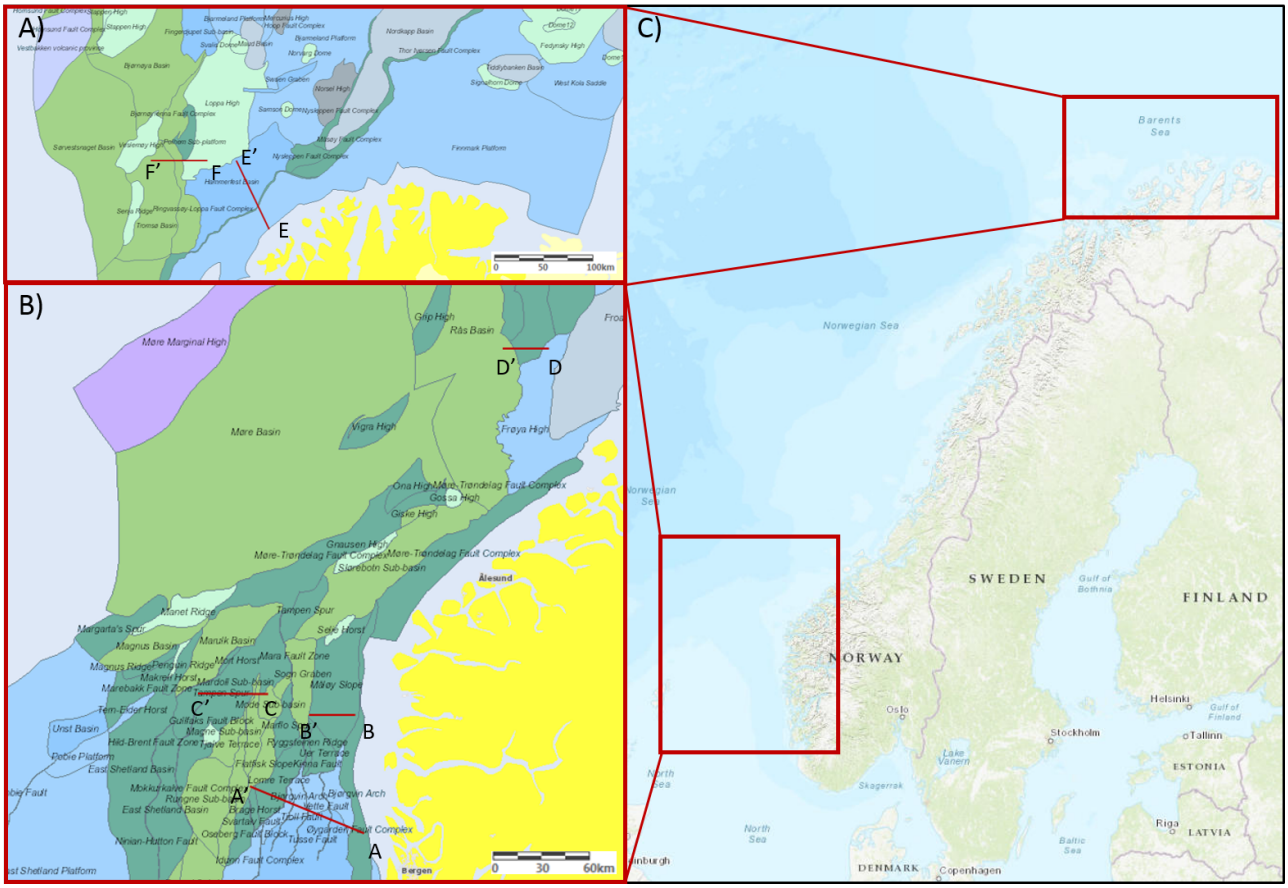


**Figure 5.1:** Maps displaying the locations of the interpreted seismic lines. Section A) displays two seismic line locations in the Barents Sea; section B) shows the locations of four seismic lines in the North and Norwegian Seas; section C) exhibits the regional locations of the aforementioned areas. Seismic lines are marked as red lines and coded in letters. The maps are made utilizing World Topographic Map (ArcMap) and NPD Map (FactMap).

| Seismic Line | Location | Area | Field |
|---|---|---|---|
| A-A' | North Sea | Lomre Terrace | Troll |
| B-B' | North Sea | Måløy Slope | Gjøa |
| C-C' | North Sea | Tampen Spur | Snorre |
| D-D' | Norwegian Sea | Halten Terrace | Fenja |
| E-E' | Barents Sea | Hammerfest Basin | Snøhvit |
| F-F' | Barents Sea | Tromsø Basin/Loppa High | |

**Table 5.1:** Table representing the location of the six seismic lines used for syn-rift strata analysis. The location of seismic lines are divided into its locality with respect to NCS, its locality with respect to structural areas and petroleum fields. The location of the lines is displayed in Figure 5.1.

The seismic line interpretation in most of the packages show thickening of the syn-rift packages in the down-thrown hanging walls of the normal faults. Abrupt thickness changes are identified in the graben structures displaying packages almost twice thicker. Some locations displays thickening in the foot-wall blocks of the normal faults, possibly induced by inversion.

The A-A' seismic line displays clear thickness changes throughout the section. The thickening beds have gradual increase in dip down-section, displaying typical growth geometry characteristics towards the western bounding fault (Figure 5.2 A). However, thickening beds absent of dip change in the syn-rift packages are observed in the same seismic line (Figure 5.2 B). Fault and growth geometries development are highly related to each other. Seismic lines B-B' (Figure 5.3), C-C' (Figure 5.4) and D-D' (Figure 5.5) display thickening beds and changes in dip in the hanging-walls of the normal faults. This is in contrast to structures observed in the GOC. The E-E' line displays thickness variations with nearly no changes in dip down-section (Figure 5.6 A); a slight dip increase was observed in the southeast section of the line (Figure 5.6 B). The seismic line F-F' shows growth strata structures characterized by gradual dip increase down-section and thickening towards the fault and in the half-graben structures (Figure 5.7). Additionally, the syn-rift strata are overlain by an unconformity.

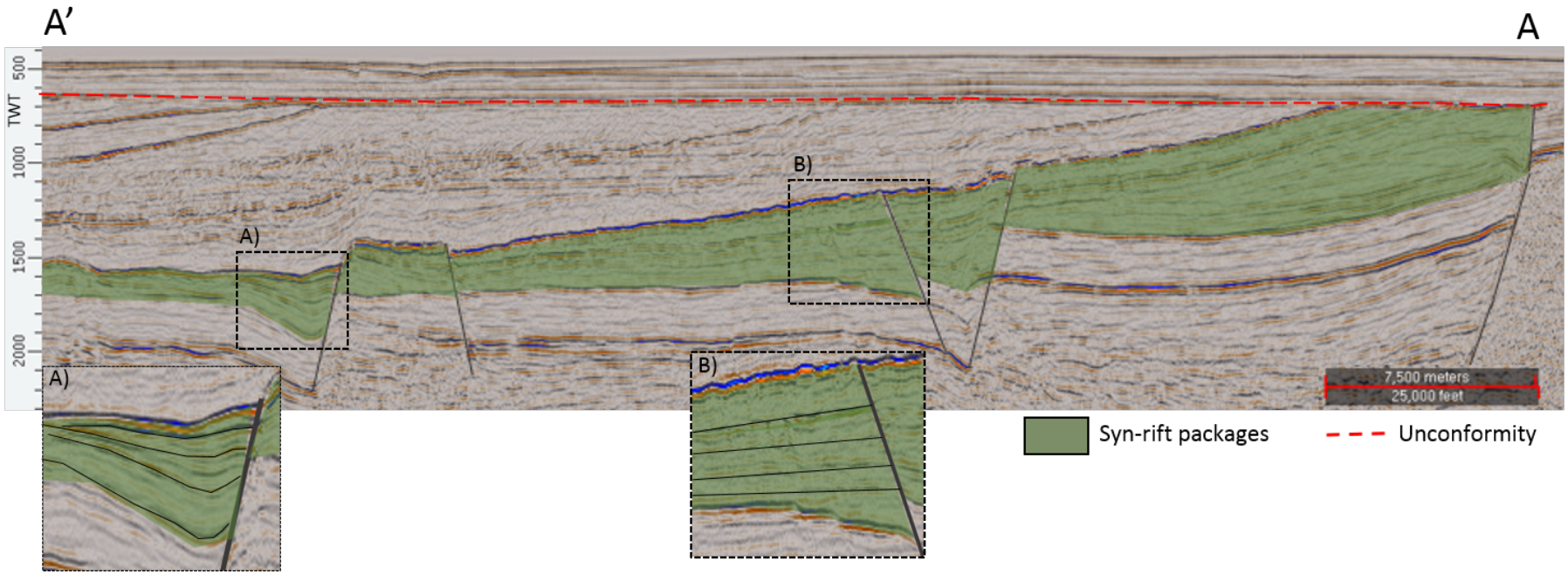


**Figure 5.2:** The interpretation of seismic line A-A' cutting across the northern part of the North Sea. Location A) displays a typical growth strata characteristics of bed thickening and increase in dip down-section; location B) display bed thickening towards the fault and a lack of change in dip down-section. The syn-rift packages are marked in green.

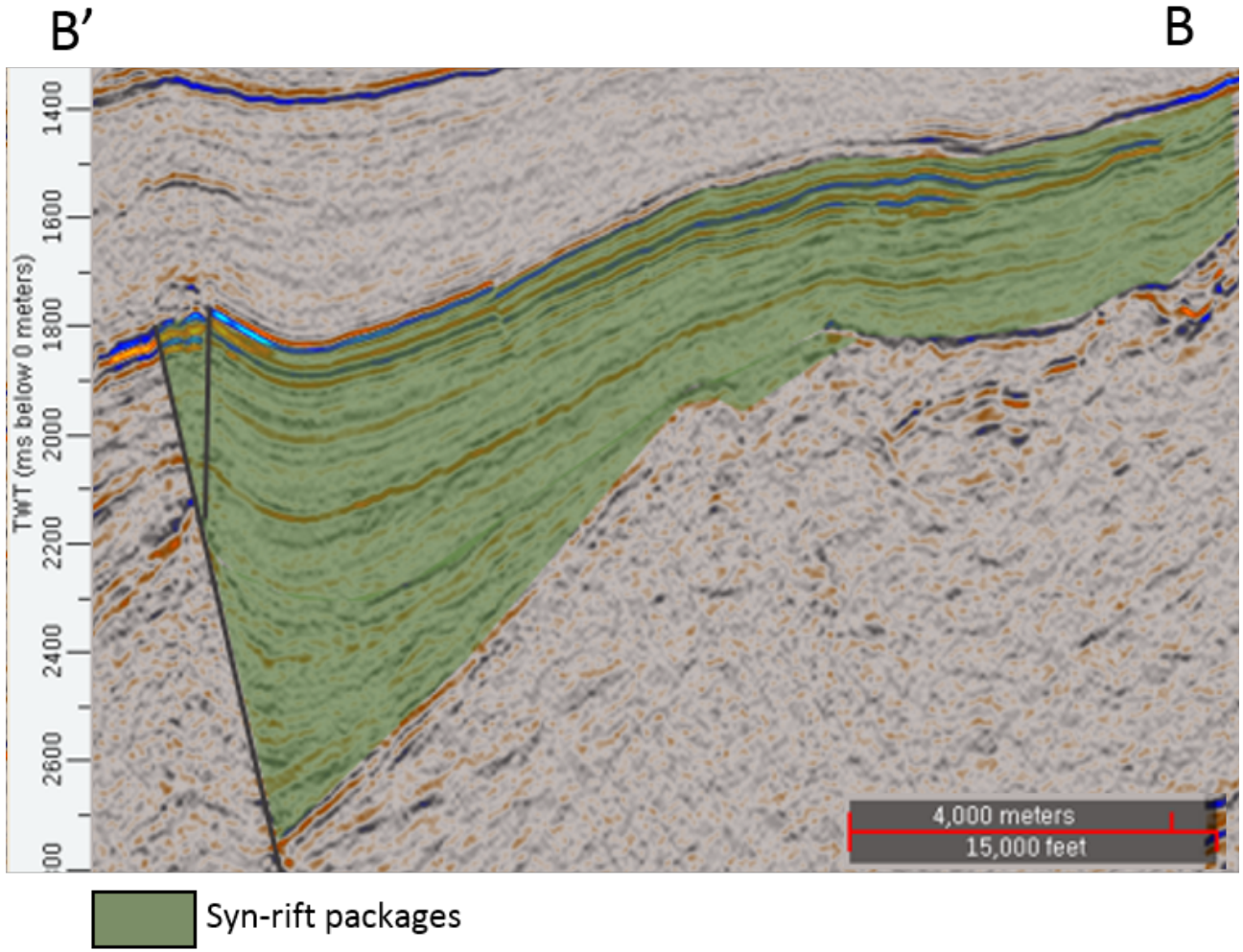


**Figure 5.3:** The interpretation of seismic line B-B' appearing on Måløy slope. The section displays thickness increase towards the fault and down-section dip increase. The syn-rift packages are marked in green.

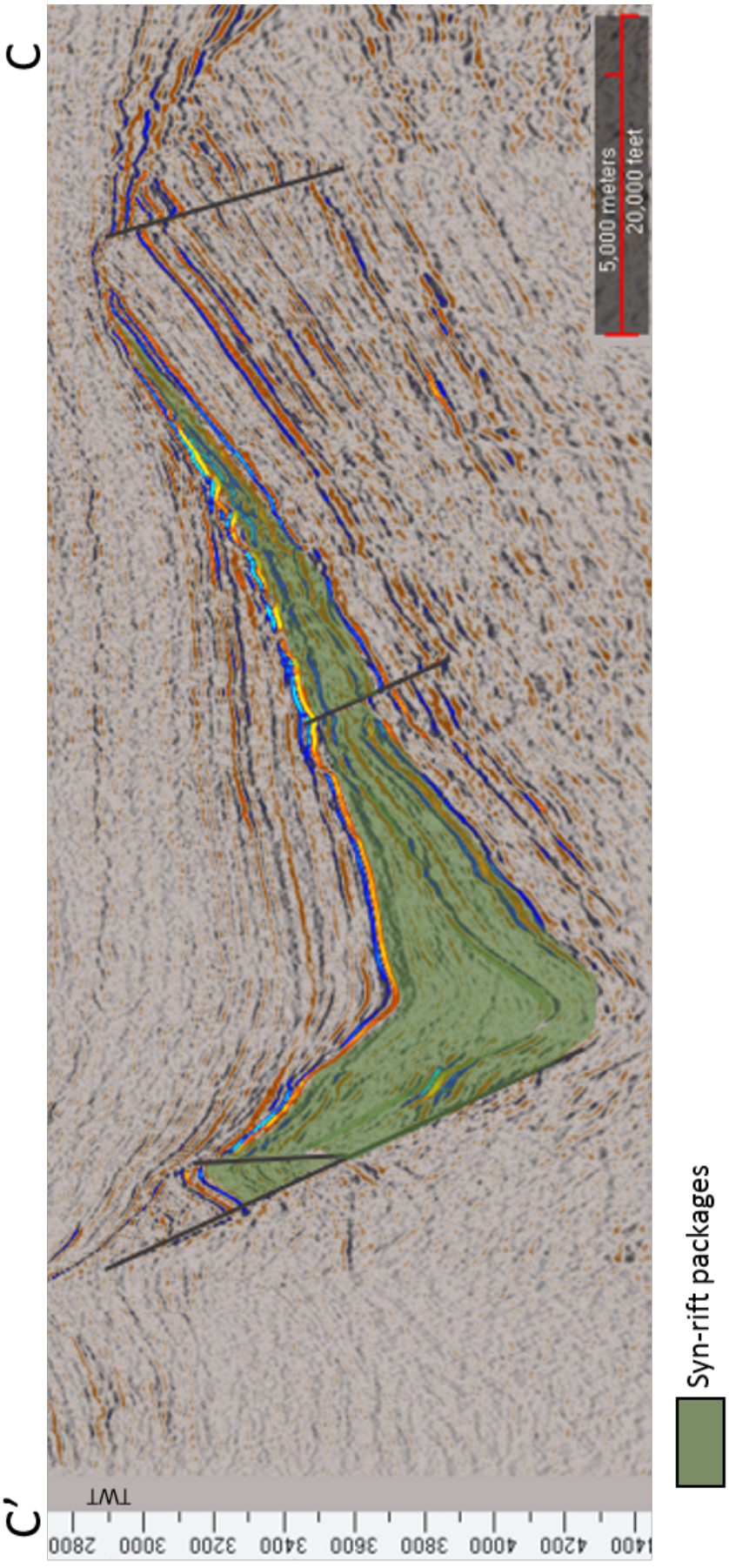


**Figure 5.4:** The interpretation of seismic line C-C', representing Tampen Spur area and Snorre gas field. The section displays thickness increase towards the syncline and down-section dip increase. The syn-rift packages are marked in green.

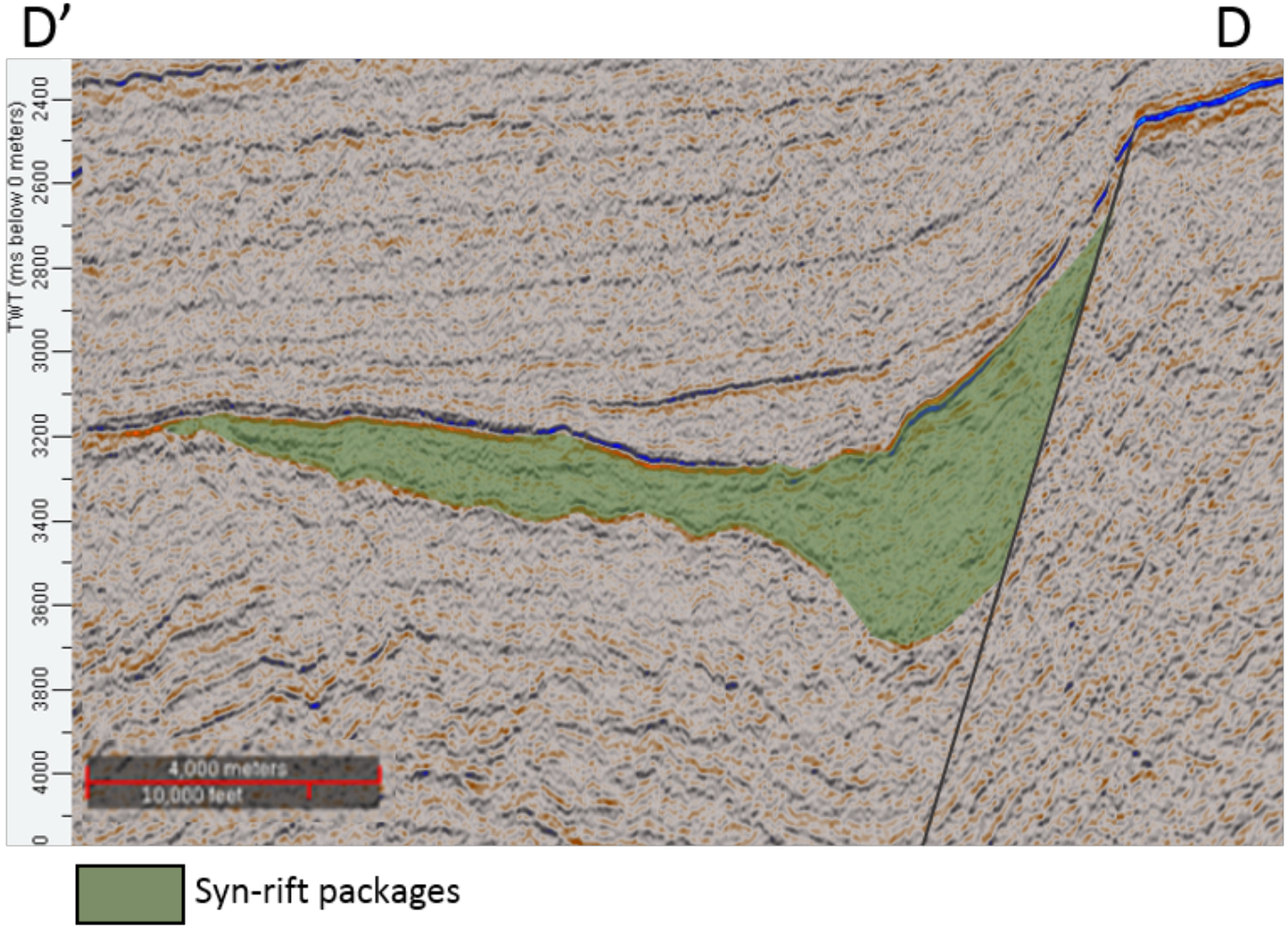


**Figure 5.5:** The interpretation of seismic line D-D' cutting across Halten Terrace in the Norwegian Sea. The section displays thickness increase towards the fault. The syn-rift packages are marked in green.

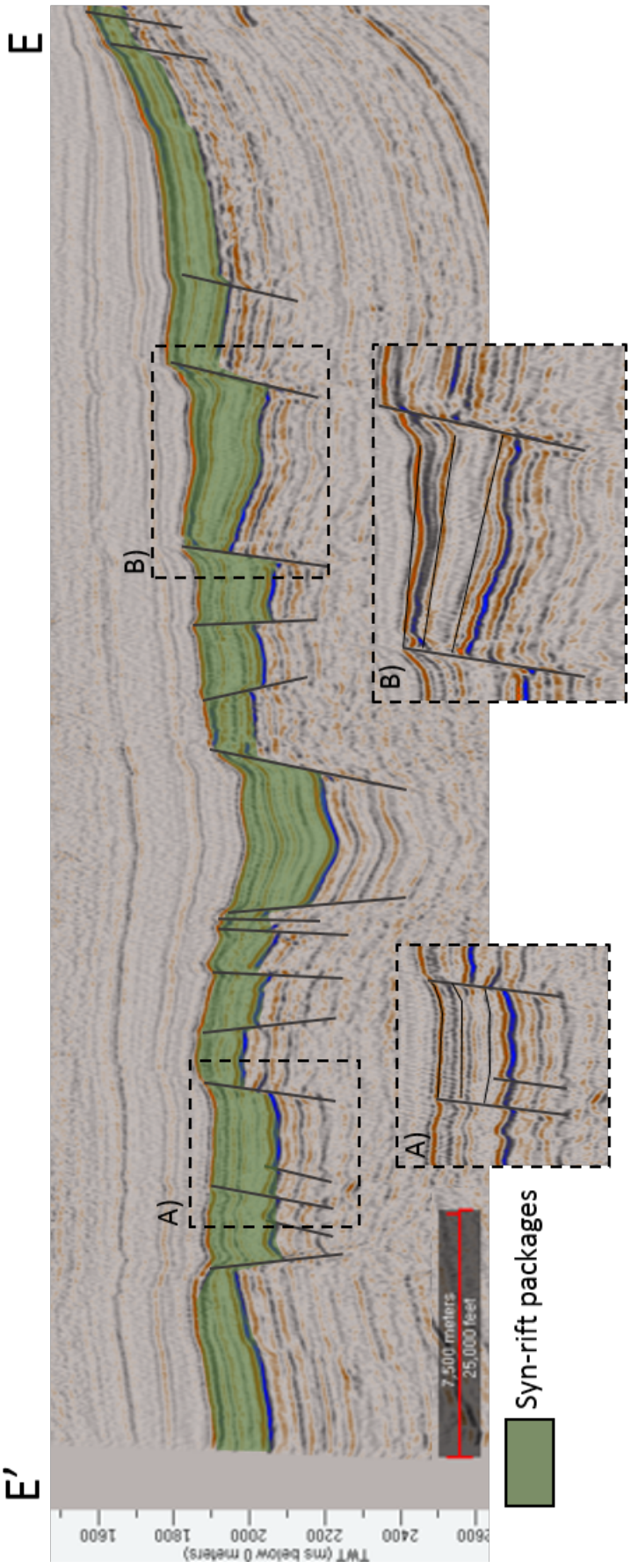


**Figure 5.6:** The interpretation of seismic line E-E', representing Hammerfest basin in the Barents Sea. Location A) displays a lack of beds thickening and no change in dip of the syn-rift packages; location B) exhibits the only structure characterized by bed thickening and dip change. The syn-rift packages are marked in green.

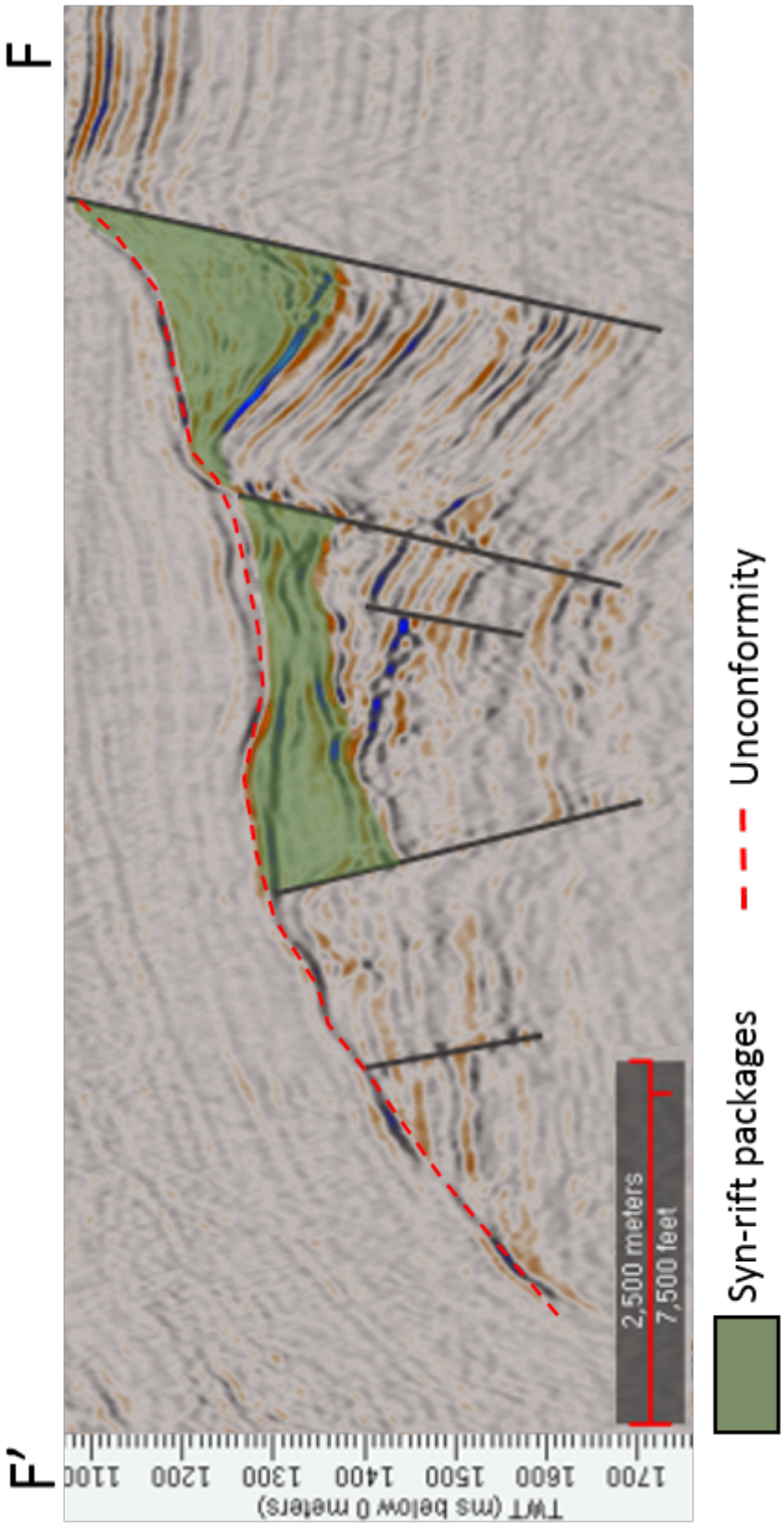


**Figure 5.7:** The interpretation of F-F' seismic line located in Tromsø basin and Loppa high. The section displays thickness increase towards the fault and down-section dip increase. Syn-rift packages are overlain by an unconformity. The syn-rift packages are marked in green.

# Chapter 6

# Discussion

Structural analysis results point towards half-graben structures lacking growth geometries, based on two quantitative analyses performed using Excel and Matlab software. The results of this research calls for a new discussion of the possible past geomorphology of the study area and a modification of the syn-rift strata definition. Generally, syn-rift sequences are interpreted using seismic data, where typical characteristics of packages are thickening towards a fault and increasing in dip down-section typically appear in the down-thrown hanging walls of the normal faults. The generation of these growth geometries is induced by simultaneous events of fault development, fault block rotation and sedimentation. Interpretation of syn-rift packages lacking growth geometries is unusual, partially supporting Syahrul's (2014) research, while contradicting Ford et al. (2016), Sigmundstad (2017) and Gawthorpe et al.'s (2018) conclusions stating existence of growth geometries. This chapter will discuss the quality of structural analysis perform in this study, the potential impact of external effects on the results and a consideration of possible past geomorphologic scenarios. Additionally, NCS's analogue potential for the GOC assessment is discussed via a comparison of seismic data with LiDAR and field data.

## 6.1 Structural Analysis

Structural analysis based on LiDAR, photogrammetry and field data focused on identifying characteristic growth geometry criteria of thickness and dip changes in syn-rift sequences. The results were based on eight outcrops, each with corresponding plots displaying the trends and

fluctuations of dip and thickness values. Irregular fluctuations cause difficulties when interpreting bedding lines and assessing the existence of growth strata, as they may obscure the real value variations. Therefore, the raw bedding line data values were smoothed utilizing appropriate parameters which preserved the initial bedding line trend while reducing the significant fluctuations. The generated structural analysis data plots displaying smoothed bedding line data exhibit moderate peaks and troughs, in addition to a few remaining significant fluctuations. These sudden bedding line data variations are partially caused by the irregular outcrops wall, which was used for bedding line interpretation. The irregularities in the outcrop surface induce data variations, due to the direct "true" point picking along the outcrop utilized during bedding line generation using LiDAR data. An additional source of the bedding line data fluctuations is due to the errors generated when 3D data are displayed in 2D plots, as done with the structural analysis performed.

Moreover, the plots generated using LiDAR data portray higher value fluctuations due to the high data resolution leading to fine detail interpretation of bedding lines. The fluctuations are visible in the bedding line, thickness and dip variation plots and they occur at the same X values thereby confirming outcrop irregularity's influence on the results. Furthermore, some LiDAR data containing outcrops display bedding line overlap (e.g., Roghi and Vrachni). The overlapping features are an artifact of the steep and skewed visualization angle of the outcrop. When the 3D data are projected into a 2D plot, the effect of viewing angle is exacerbated, which on a large scale and at further distances can generate overlapping bedding lines in the plots. The outcrops containing photogrammetry and field data have less fluctuations in bedding lines, possibly due to the use of fewer visualization angles and worse interpretation quality which may conceal minor bedding line variations (e.g., Monastery and Kefalari East). However, these outcrops exhibit a few significant fluctuations due to the bedding line's intersections with faults (e.g., bedding lines 1, 2 and 3 in Monastery outcrop) or irregularities in the outcrop surface (e.g., bedding lines 3 and 4 in Kefalari East outcrop). The generated bedding line plots used for structural analysis display varying bedding line lengths in some cases. This is believed to be caused by poor outcrops exposure and heavy vegetation cover in addition to erosion affecting the bedding line continuity.

Despite the occurring value fluctuations observed in structural analysis plots, the results are geologically accurate and correspond to the initial field data outcrop interpretations. Bedding line data plots exhibit similar bedding patterns and trends, confirming the accuracy of the structural analysis data. The generated dip variation plots are dominated by constant dip values, although, a few bedding line display trends of dip increase (e.g., bedding lines 6 and 4 in Roghi and Vrachni outcrops, respectively). These bedding lines are dominated by dip increase of a single bedding line per outcrop, which is not indicative of growth geometries throughout the sequence. Growth geometry existence would cause a substantial and consistent increase in dip down-section. Furthermore, singular bedding lines exhibiting dip value increase results in thickness increase illustrated in the structural thickness plots (e.g., bedding line 9 in Lapanagoi; bedding line 5 in Roghi, bedding line 7 in Vrachni etc.). Thickness variations exhibited in less than two bedding lines per outcrop are induced by similar issues related to value fluctuations caused by the irregular outcrops wall and occasional bedding line overlap. Furthermore, growth geometries are expected to display significant thickening towards the fault, corresponding to the fault displacement and accommodation space creation. Thickness increase in at least more than three bedding lines would be expected to interpret a significant thickness trend indicative of growth geometries.

Supplementary data quality assessment was carried out by calculating standard deviation of the bedding line thickness and dip results. Standard deviation values are high and inconsistent when data are of lower quality, and low and uniform when data are of high quality. The lowest and most uniform standard deviations for dip values are at Lapanagoi, Vrachni and Kefalari East, while the largest standard deviation values appear at Roghi and Monastery outcrops. Standard deviation thickness values are more uniform throughout, with the lowest variations displayed in Lapanagoi, Monastery and Kefalari East outcrops. The results from standard deviation analysis show a strong relationship between thickness and dip value dependent trends, where outcrops displaying high dip variations also exhibit high thickness variations. However, a few bedding lines with significant thickness changes display relatively low standard deviation for dip values, but this is not common and is considered to be insignificant. The results with high standard deviation correspond with areas of poor data quality. This is explained in different

cases by bedding line interpretation based on only one bedding line situated in a highly eroded areas (e.g., bedding line 9 in Lapanagoi outcrop) and negative thickness value results caused by overlapping of two bedding lines (e.g., bedding lines 3 and 4 in Vrachni outcrop, bedding line 3 in Roghi outcrop).

## 6.2 Comparison with Other Research

Several research projects have been conducted in the past at study areas A and B, often concluding in existence of growth strata geometries in the syn-rift packages. Misleading results indicating growth strata existence could likely be induced by improper viewing angle of the outcrop, displaying misleading apparent thickness and dip angles. Furthermore, numerous research results are based solely on literature and field data, creating a bigger error margin due to the lack of data quality control. Studies with results based on the 3D model constructed with field data input results in identical errors as in the acquired field data. Furthermore, bedding line interpretation extrapolation in highly vegetated areas produce low quality interpretations stemming from the unreliable data.

Some researches display contrasting field data and interpretation results, proposing growth geometry existence, although, illustrating constant dip and thicknesses in the cross-sections (Figure 6.1). Gawthorpe et al. (2018) generated cross-sections that are not indicative of growth strata in syn-rift packages, but the observations are not mentioned or explained (Figure 4.27). A few studies propose syn-rift strata absent of growth geometries (Syahrul 2014; Oppedal 2017). Oppedal (2017) constructed a 3D model suggesting the existence of growth geometries in the eastern Kerpini fault block, but absence of growth features in Roghi and Monastery outcrops (Figure 6.2). Similarly, Sigmundstad (2017) concluded the existence of growth strata's presence in the Kerpini fault block. Furthermore, several research projects were conducted in the GOC offshore. For instance, Mostafa (2017) provided an interpretation of late and early syn-rift sequences displaying a lack of typical growth geometry characteristics in numerous sections. The interpretation displayed relatively parallel bedding lines of constant thickness which were falsely misinterpreted as syn-rift with regards to the general syn-rift definition (Figure 6.3).

In addition, research of Syahrul (2014) states that growth geometries are not indicative of

its characteristic criteria at locations situated more than 10 km away from the fault. However, eight investigated outcrops are situated at various distances away from faults and different half-grabens, but even the outcrops located only few hundred of meters away from the fault (e.g., Lapanagoi and Roghi) are dominated by syn-rift sequences absent of growth geometries.

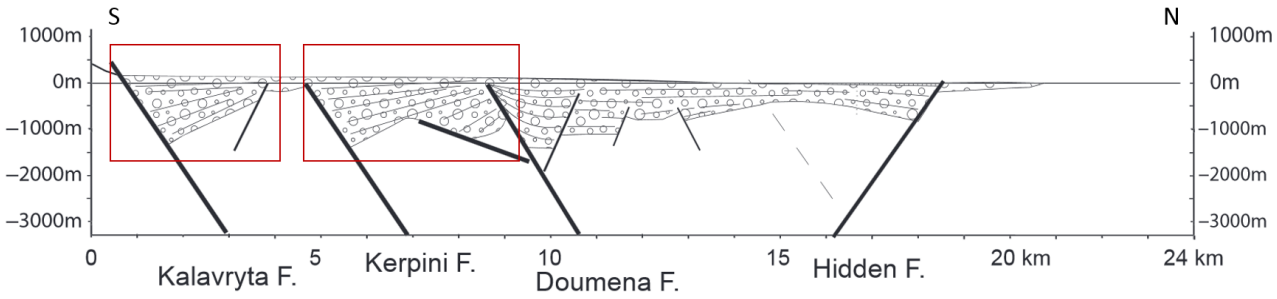


**Figure 6.1:** Cross-section illustrating structural elements, lithologies and bedding lines, stretching across study area A in N-S manner. Modified after Ford, Rohais, et al. 2013.

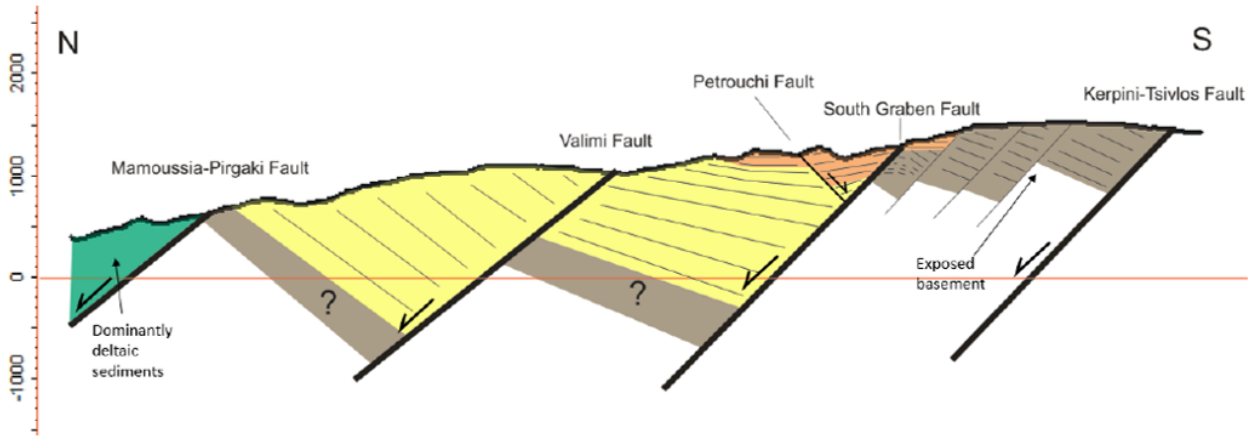


**Figure 6.2:** Cross-section illustrating structural elements, lithologies and bedding lines retrieved from a 3D model. The cross-section stretches across study area A in N-S manner. Modified after Oppedal 2017.

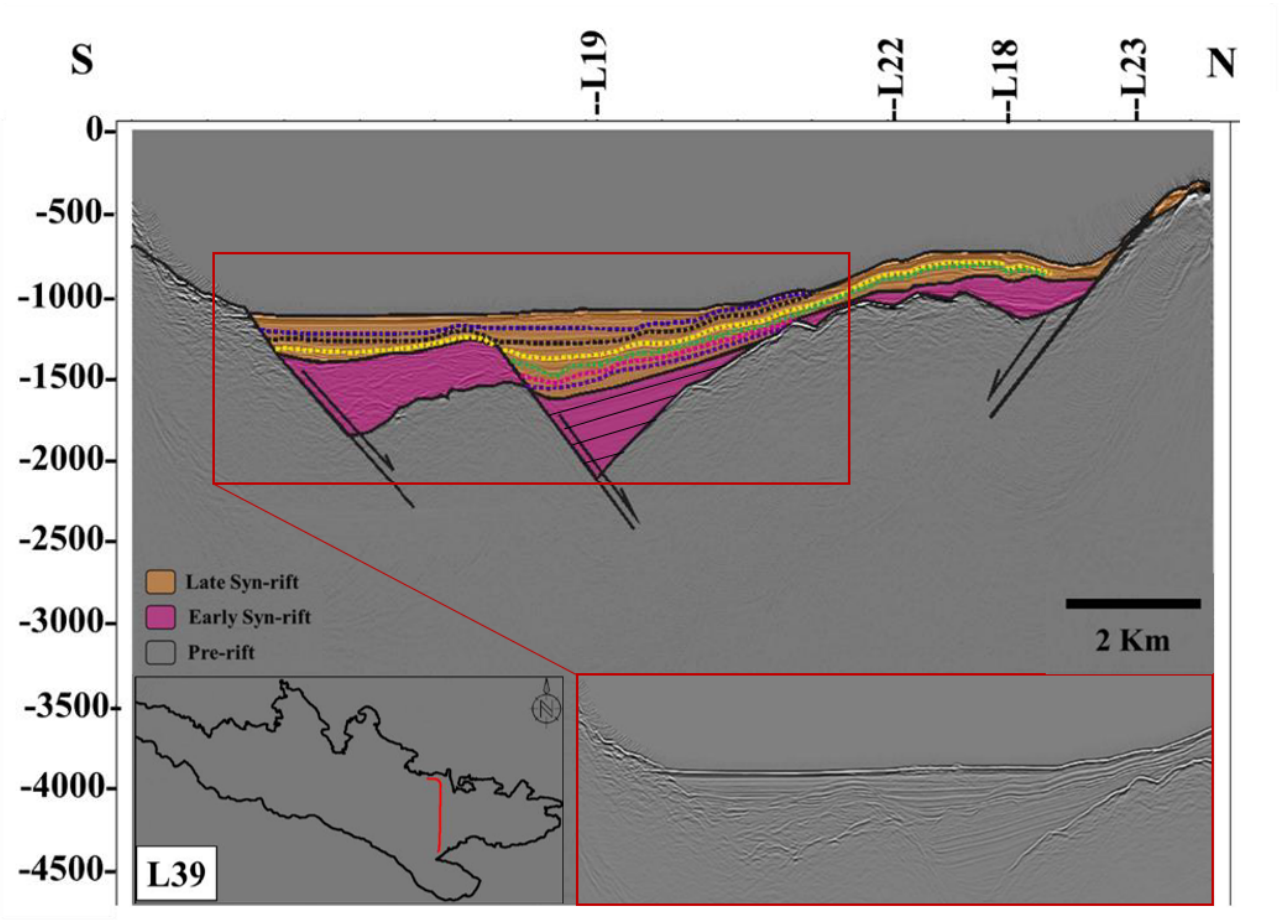


**Figure 6.3:** Interpretation of seismic section located offshore of GOC. Modified after Mostafa 2017.

## 6.3 Past Geomorphology

Several possible past geomorphological scenarios are proposed and discussed to explain the lack of growth strata in syn-rift packages. All of the proposed scenarios are potentially controversial, and no individual scenario provides an explanation to all aspects of the depositional history. Therefore, it is highly probable that syn-rift packages absent of growth strata developed from combination of proposed scenarios and geological events.

### 6.3.1 Late Fault Block Tilting

The late fault block tilting scenario describes syn-rift package deposition during active rifting (Figure 6.4). The active normal fault induces uplift of the foot-wall, creating sediment supply due to the erosion of the fault block tip. The down-thrown hanging wall creates free accom-

modation space, which sediments infill parallel to the hanging-wall plane. The simultaneous rifting reaches its climax, causing fault block and sediment rotation. The horizontal syn-rift packages incline, remaining parallel to the hanging-wall.

The scenario of late fault block rotation explains one of the possibilities for sediment deposition lacking growth strata during active rifting. However, it contains uncertainties regarding the mechanism causing late rotation. Geologically favored domino fault model describes fault block rotation simultaneous with rifting, which would typically produce growth strata.

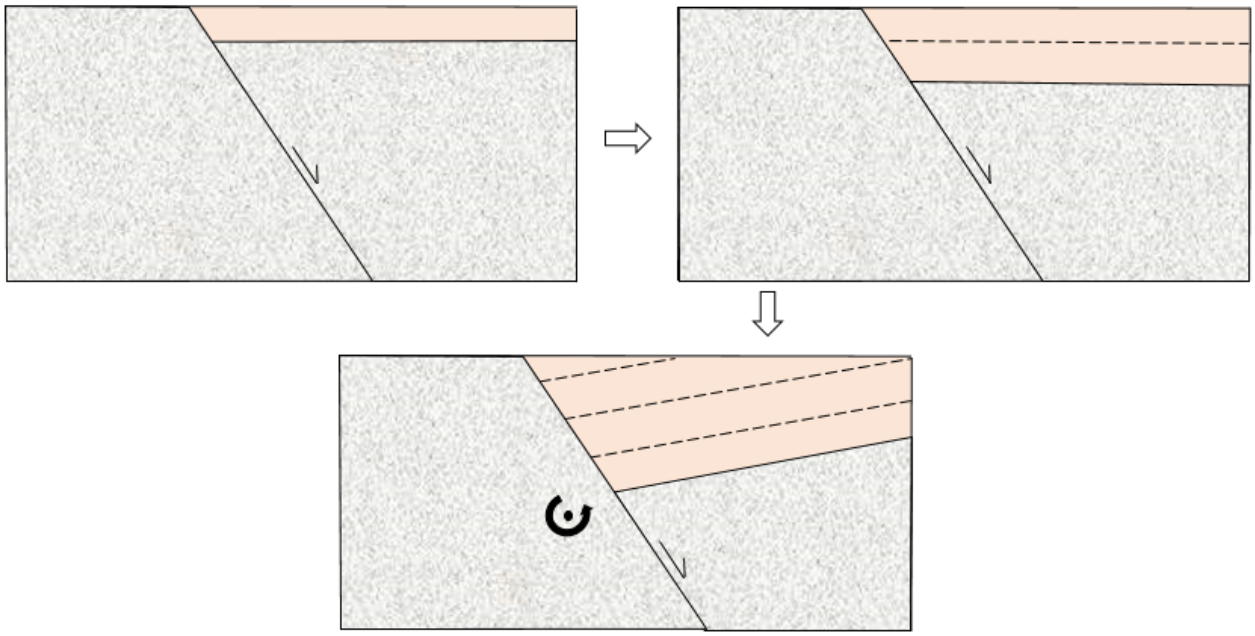

**Figure 6.4:** Conceptual sketch illustrating late fault block tilting and its influence on syn-rift packages.

### 6.3.2 Gradual Fault Movement

The theory of gradual fault movement takes into account the continuous rotation of fault blocks induced by active rifting (Figure 6.5). The scenario explains sediment deposition with simultaneous fault block rotation and relatively low sediment supply incoming from the uplifted hanging-wall. Moderate rifting induced normal faults creating limited accommodation space and nearly parallel sediment deposition to the hanging-wall surface. The rotation rate is nearly equal to the rifting rate, causing slow rotation of the fault blocks and allowing deposition of packages nearly absent of growth geometries. The deposited syn-rift packages would display slight changes in thicknesses, nearly impossible to identify in the field. Gradual fault movement

scenario requires slow rifting conditions. However, GOC is known as one of the Earth's most active continental rifting zones and, therefore, this theory might not be correct for the GOC.

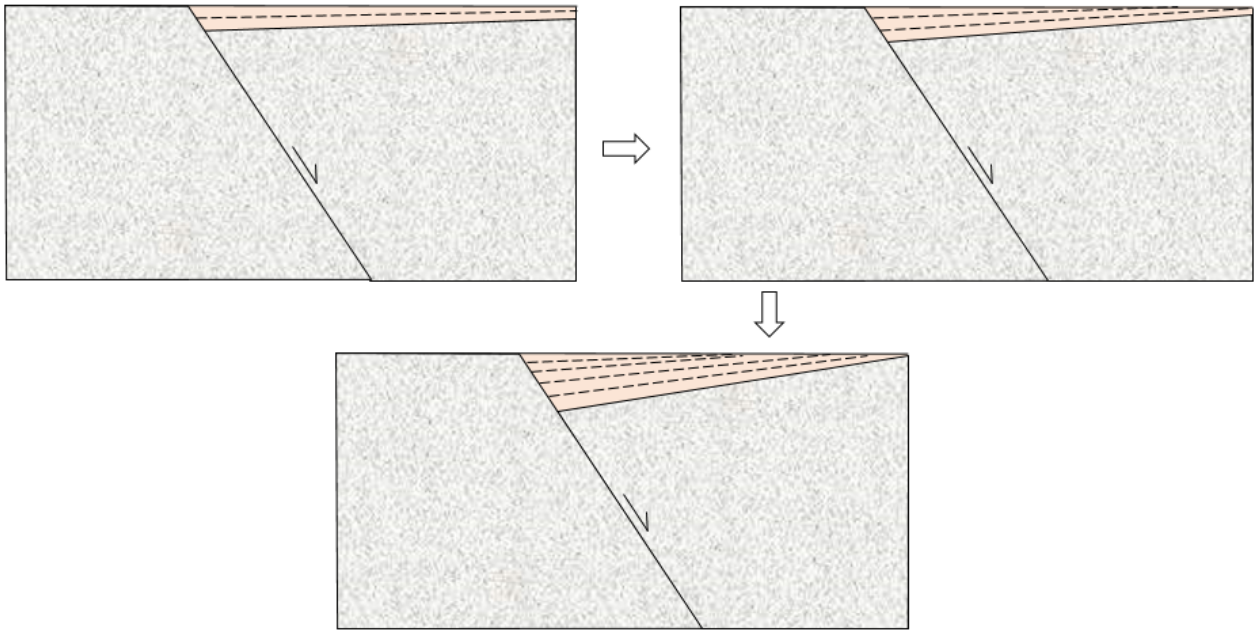

**Figure 6.5:** Conceptual sketch illustrating episodic fault movement and its influence on syn-rift packages.

### 6.3.3 Erosion

The erosion scenario describes the syn-rift packages deposition with characteristic growth geometry strata. Uplifted foot-wall supplies sediments deposited on the hanging-wall during active rifting and fault block rotation (Figure 6.6). The free accommodation space is infilled simultaneously to the rotation and active faulting, creating dip increase down-section, thickening towards the fault and facies changes throughout the sedimentary packages. The deposited syn-rift strata are then partially eroded, generating a misleading view of packages absent of growth geometries in the field. The scenario requires a very high erosion rate to partially erode the syn-rift packages, creating the visual illusion of lack of growth strata. Additionally, detailed structural analysis, conducted for this research, indicate no hard evidence of dip and thickness variations in the syn-rift packages.

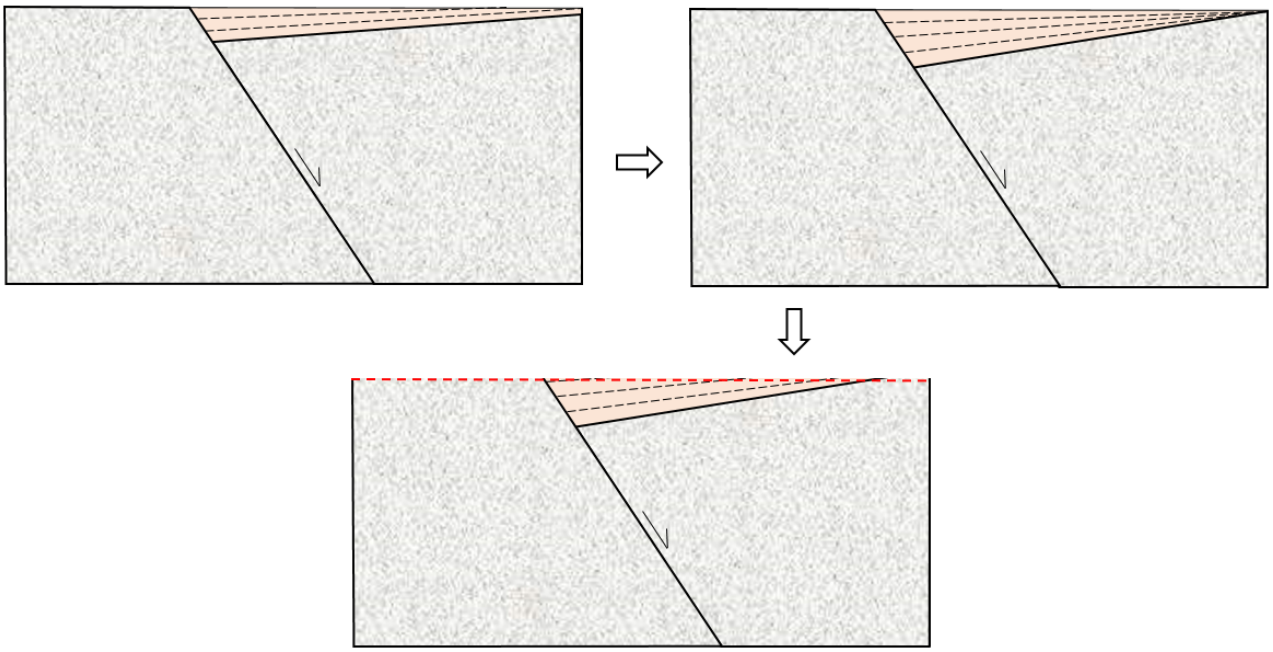

**Figure 6.6:** Conceptual sketch illustrating depositional scenario of sediments lacking growth geometries and its influence on syn-rift packages. Erosion is highlighted with red dashed line.

### 6.3.4 Reverse Drag

Reverse drag is a common structure appearing in highly faulted areas, often associated with normal faults. The reverse drag scenario was first proposed by Syahrul (2014) to explain the lack of growth geometry strata in syn-rift packages. The structures commonly appear adjacent to the fault plane on both up-thrown and down-thrown blocks (Figure 6.7). The distance between the reverse drag and fault influences the dip angle on the syn-rift deposits (Syahrul 2014; Cunningham 2015). Therefore, reverse drag can lead to particular areas lacking growth geometries, at least 10 km away from the fault. Reverse drag theory requires outcrops situated 10 km from the fault, in order for lack of growth geometries observations to occur. The studied half-graben systems appear relatively close to the fault, less than 10 km away, which makes this scenario not applicable.

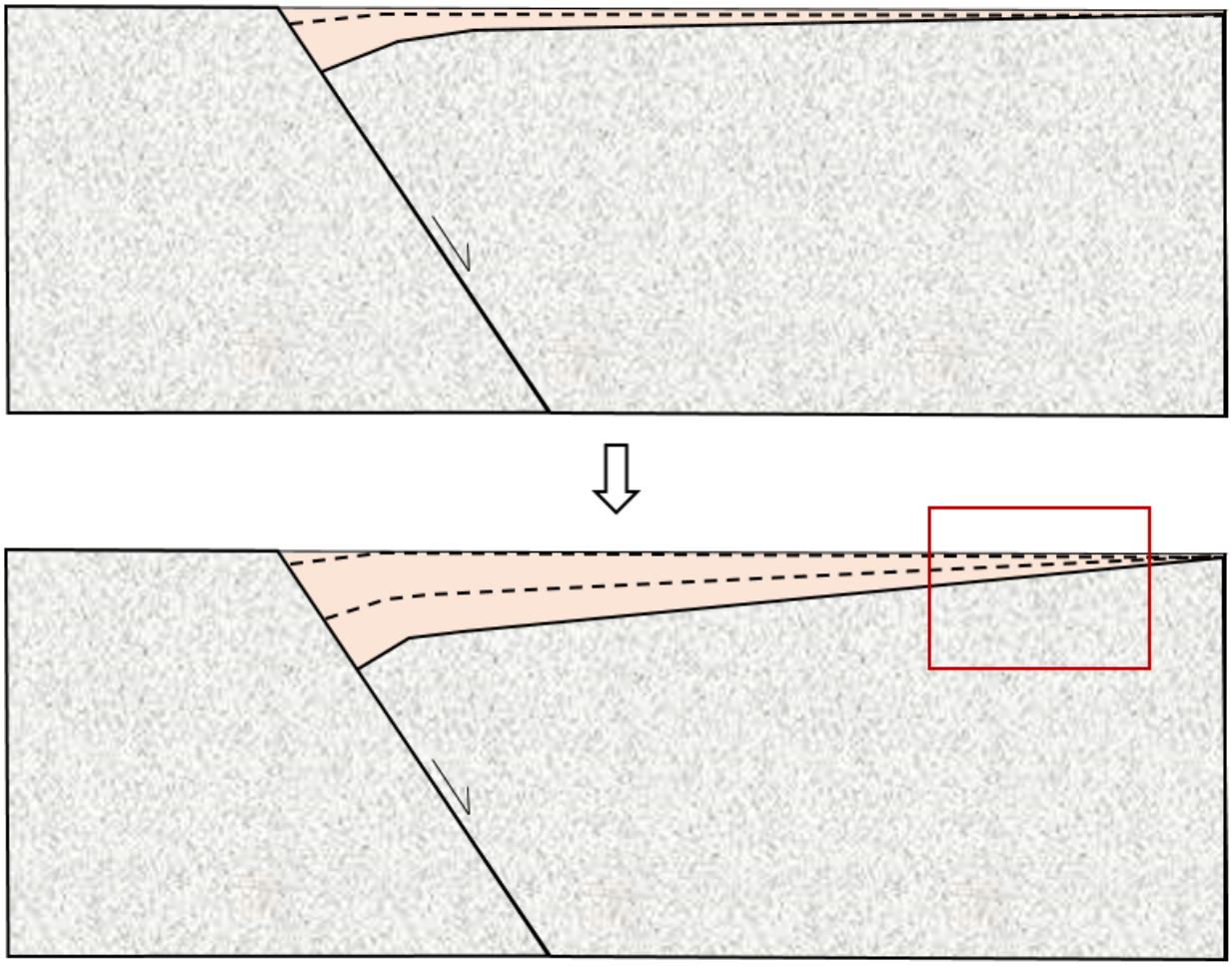

**Figure 6.7:** Conceptual sketch illustrating reverse drag scenario and its influence on syn-rift packages. The area indicative of lack of growth geometries is highlighted in a red rectangle.

### 6.3.5 Inactive Faults

Inactive fault theory explain sequence deposition lacking growth geometry structures by sediment deposition during inactive faulting appearing prior to rifting and normal fault development. The theory suggests pre-rift definition of the analyzed conglomerate deposits rather than syn-rift. The basement in GOC is defined as a 1.5 km thick metamorphosed limestone deposits, overlain by conglomerates consisting of rounded limestone clasts. The metamorphosed limestone had to be uplifted in order to supply sediment for the deposition of conglomeratic sediments. Thus, the studied half-graben outcrops consisting of conglomeratic sediment had to be deposited during active rifting. Since, syn-rift sedimentary sequences are controlled by syn-depositional normal faulting, and are usually defined as strata deposited during active rifting

which exhibit growth geometries generated during rift-climax (Ravnas and Steel 1998). The syn-rift thickness variations are often correlated with fault activity patterns indicating periods of high and low throw rates, and are utilized for fault evolution analysis (Mannie et al. 2016). The Corinthian rift is characterized by a high rifting rate (10-15 mm/year) and is dominated by normal fault systems located on the northern and eastern flanks of the rift. However, the outcrops studied at the GOC display syn-rift packages absent of growth geometries. On average, the major faults exhibit average high displacement values ranging 460-815m; 488-1775m; 1195-1622m; 1768-3655m; 2022-2529m in the GOC area (Egeland 2018). High displacement values indicate equivalently large amount of free accommodation space creation, which could be infilled with sediments originating from uplifted foot-walls comprising metamorphosed limestone. The coarse conglomerate limestone clasts indicate rapid sediment deposition supplied from south-southwest (Ford, Hemelsdael, et al. 2016, Oppedal 2017). Rapid sedimentation and thick conglomeratic packages imply maximum accommodation space, thus, indicating conglomerate sediments deposition during the syn-rift.

The inactive fault theory contradicts with sediment deposition, displacement rates and uplift explanation of the GOC are and, therefore, is unlikely to hold true.

### 6.3.6 Visual Deception

Lack of growth geometries depositional history is hard to explain. Most of the theories does not describe a correct depositional history that is appropriate for the GOC's geological settings. Therefore, it is logical to investigate a visual deceptions theory, which describes the existence of growth strata by evaluating misleading field interpretation results.

A possible theory describes thick packages with growth geometries, that are only partly outcropping in the field. This leads to an inability to identify typical growth strata characteristics which remain located underground. However, fault growth is related to accommodation space creation and sediment supply, which means that the extent of growth geometries is related to the displacement of the fault. Therefore, a fault with 500 meters displacement would generate approximately 500 meters thick growth geometries, which should be visible in the field. Growth geometries would be visible in the field independent of fault's displacement rate, due to the

proportional development ratio. The amount of erosion required to remove evidence of growth geometry strata at the surface would therefore also be related to the thickness of growth geometries and degree of fault displacement. While the GOC is a young rift meaning that erosion is likely minimal, this theory is a possibility.

Additionally, geological events like fault rotation and faulting induce the growth geometry generation in the contrast to the interpretation of early rift packages which are continuous horizons whose coherency may have been destroyed during faulting and fault rotation (Taylor et al. 2011).

## 6.4 Analogues

The GOC has been utilized as an analogue for several rift basins all over the world, including the NCS. However, GOC displays lack of growth geometries in syn-rift packages, which might not be the case in NCS. Additionally, both rifts were influenced and shaped by different tectonic. After a quick tectonic history and seismic analysis comparison of GOC and NCS, the main differences were assessed. The difference between the GOC and NCS geological provinces include differences in rift initiation age, types of erosional events, geologic structural features present, and presence and type of volcanism and tectonic events (e.g., uplift and inversion). These causative differences are possibly related to the lack of growth geometries in the GOC interpreted from the field data, compared to the abundance of growth strata in the NCS.

The overall interpretation of the seismic lines resulted in syn-rift packages displaying an abundance of common growth geometry structures. Typically, four types of different syn-rift packages were encountered in the NCS and were classified as follows:

- Thickening in the hanging wall of a normal fault
- Thicker strata evenly distributed in graben
- Thickening towards a singular fault in the graben
- Thickening strata without increase in dip down-section

Two out of six seismic sections displayed a lack of gradual increase in dip down-section with the thickening of packages towards the fault (seismic lines A-A' and E-E'). The seismic lines displaying similar structural features lacking growth strata are located in Hammerfest Basin (Barents Sea) and Lomre Terrace (North Sea). The absence of growth geometries could be caused by low resolution of the seismic profile; although, with a 200 meter high Lapanagoi outcrop should be possible to resolve in seismic (Figure 6.8). Therefore, some particular areas in the Norwegian Continental Shelf have potential for being a good analogue with the Gulf of Corinth. In order to determine the analogue's quality between these two geological provinces, a thorough investigation of NCS and areas displaying similar features is needed.

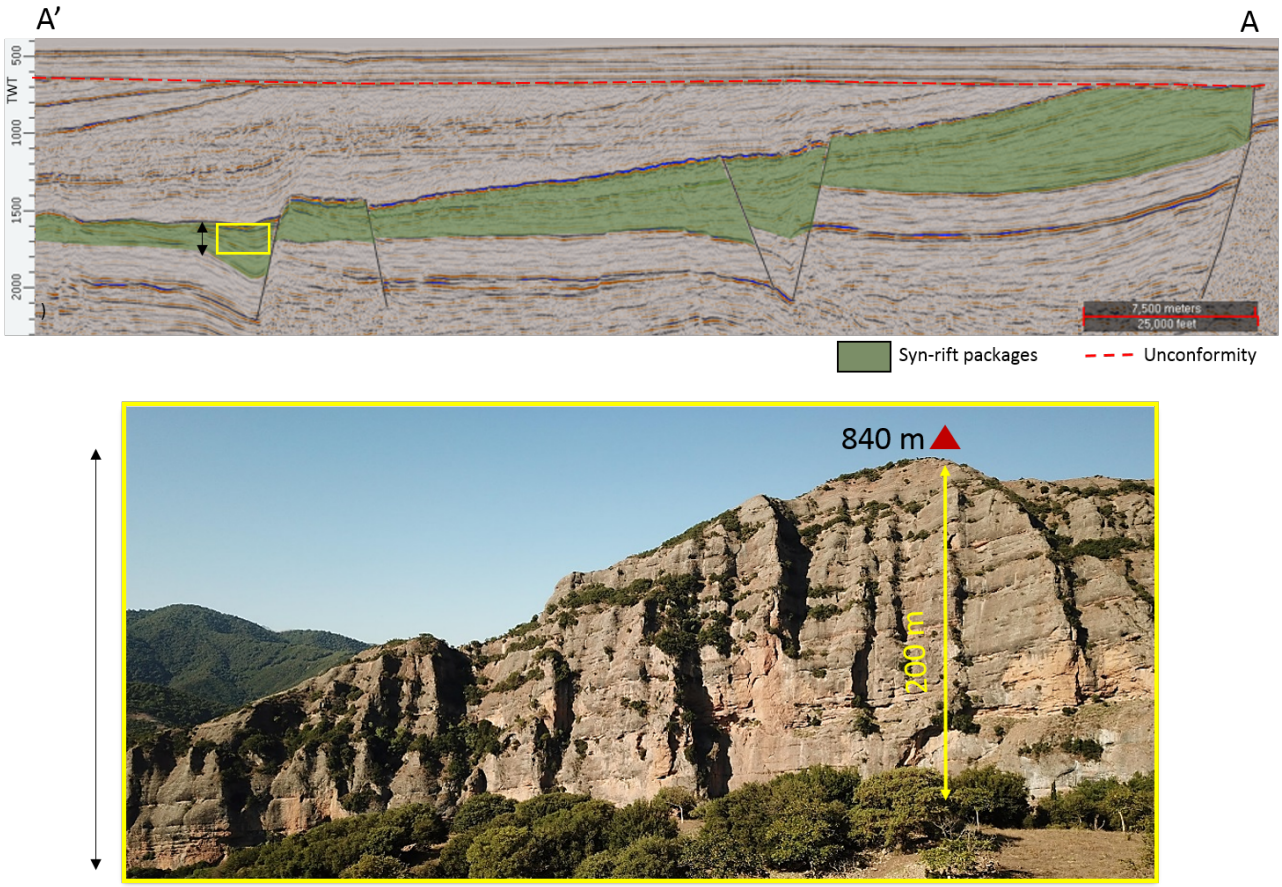


**Figure 6.8:** Scale representation between seismic resolution and Lapanagoi outcrop. Two way travel time (TWT) of seismic line A-A' is displayed in relation to Lapanagoi outcrop's height. The approximate estimate of Lapanagoi outcrop size in a seismic line is highlighted with a yellow box.

## 6.5 Syn-rift Packages Interpretation

Growth geometries are common features in rift basins, usually defined by sediments deposited during active rifting and exhibiting clear package's thickness increase towards a fault and dip increase down-section. These few criteria are often utilized for seismic interpretation of the syn-rift packages all over the world, which might be false in some areas. Probability of syn-rift packages absent of growth geometry features occurring in several other rift basins in the world is rather great. The evidence is exhibited by the performed NCS analysis, demonstrating possibility for lack of growth in syn-rift outside the GOC. Furthermore, biased interpretations completed with expectations of typical growth indications in the syn-rift packages presents incorrect results, which might lead to several already examined areas dominated by structural features lacking growth strata. In order to assess if syn-rift packages absent of suspected thickness and dip changes is a global occurrence, additional outcrop studies from other half-grabens are necessary. If true, syn-rift sequences are difficult to distinguish from post or pre rift sequences and further investigation of syn-rift should be based on several geological aspects including analyses of basin architecture, depositional patterns and depositional history together with tectonic events influencing the study area. The reliance on conventional growth geometry characteristics without a careful consideration of these various other factors could lead to a misinterpretation of syn-rift packages.

# Chapter 7

# Conclusion

The study presents relatively new observations of syn-rift strata in half-graben structures lacking typical growth geometry features. These results provide valuable insight into the syn-rift strata deposition, possible past geomorphology and potential quality as an analogue for the NCS of the half-grabens in the Corinthian Rift. The conclusions of the research are as follows:

- The structural analysis was carried out using field data supplemented with LiDAR and photogrammetry data. This combination provides high resolution, accurate results of the interpreted bedding lines. A byproduct of the high resolution is high value fluctuations which complicate interpretation of data trends.

- Two different structural analysis approaches were carried out utilizing Matlab and Excel software. The approaches include slightly different bedding line thickness and dip value calculations and resulted in contrasting data qualities. The most suitable and effective approach for growth geometry determination in syn-rift packages is the approach of Matlab, where 3D data are projected in 2D along the outcrop's strike line.

- The interpretation of syn-rift packages lacking growth geometries does not have a straightforward explanation, requiring several extensive investigations of half-grabens in order to determine the past geomorphology.

- The observed syn-rift sequences absent of growth geometry features contradict with general syn-rift strata description characteristics. Based on these results, perhaps syn-rift

packages should no longer be specified solely by the conventional characteristics of thickening towards the fault and dip increase down-section. The interpretation of syn-rift packages should be based on more than just one criteria, ideally combining basin architecture, depositional patterns and depositional history together with tectonic events influencing the study area to guide the interpretation.

- The proposed past geomorphological scenarios do not, individually, take into account all of the geological factors and, as such, no single scenario is believed to be able to lead to syn-rift sequences lacking growth geometries. Rather, a combination of geomorphological scenarios occurring simultaneously is proposed to explain the lack of growth geometries in the investigated syn-rift packages. The proposed scenarios are:
  - Late fault block tilting
  - Gradual fault movement
  - Erosion
  - Reverse drag
  - Inactive faults
  - Visual deception
- Analogue assessment analysis of the NCS resulted in two areas exhibiting similar syn-rift features to the GOC. However, it is highly probable that syn-rift packages lacking growth geometries is a global trend, which is often falsely interpreted today due to the inaccurate syn-rift description and biased interpreters.
- Possible analogue areas for the GOC in the NCS is situated in the Lomre Terrace in the North Sea and the Loppa High area in the Barents Sea.

Recommendations for similar future projects concerning the structural analysis workflow for investigating syn-rift strata using LiDAR and field data include the refinement of the utilized point-cloud and bedding line interpretation workflow, together with a streamlined file import and export step, resulting in more efficient workflow. Other recommendations for future work

include analogue assessment of the NCS with other rift systems in the world, refinement of the syn-rift strata interpretation criteria through further analysis of syn-rift packages utilizing various data types and novel interpretation criteria and several half-graben syn-rift sequence global investigations in order to assess lack of growth geometries occurrence. The potential half-grabens for growth strata investigation include 1) outcrop appearing east from Vrachni town (Figure 4.16) and 2) detailed analysis of Xylocastro and Amphithea outcrops. Finally, thorough studies in the GOC area focusing on past geomorphological reconstruction are recommended to shed light on the possible combination of geomorphological scenarios that could result in syn-rift strata lacking growth geometries.

# Bibliography


Ambraseys, N. and J. Jackson (1997). "Seismicity and Strain in the Gulf of Corinth (Greece) since 1964." PhD thesis, pp. 433–474. DOI: 10.1080/13632469708962374.

Armijo, R., B. Meyer, G. King, A. Rigo, and D. Papanastassiou (1996). "Quaternary evolution of the Corinth Rift and its implications for the Late Cenozoic evolution of the Aegean." In: *Geophysical Journal International* 126.1, pp. 11–53.

Barnett, J. A., J. Mortimer, J. Rippon, J. Walsh, and J. Watterson (1987). "Displacement Geomentry in the Volume Containing a Single Normal Fault." In: *The American Association of Petroleum Geologists Bulletin* 71, pp. 925–937.

Benedicto, A., V. Plagnes, P. Vergely, N. Flotte, and A. Schultz (2008). "Fault and fluid interaction in a rifted margin: integrated study of calcite-sealed fault-related structures (southern Corinth margin)". In: *Geological Society, London, Special Publications* 299, pp. 257–275. DOI: https://doi.org/10.1144/SP299.16.

Brekke, H. (2000). "The tectonic evolution of the Norwegian Sea Continental Margin with emphasis on the Voring and More Basins." In: *Geological Society London Special Publications* 167(1), pp. 327–378.

Chen, Z. (2017). *The Application of Airborne Lidar Data in the Modelling of 3D Urban Landscape Ecology.* Newcastle: Cambridge Scholars Publishing. ISBN: 1-4438-9986-0.

Chery, J. (2001). "Core complex mechanics: From the Gulf of Corinth to the Snake Range." In: *Geology* 29.1, pp. 439–442.

Cunningham, J. E. (2015). *Modeling Synrift Sediment Infill Patterns of Synthetic Normal Faults. Master Thesis.*

Dercourt, J. (1964). "Contribution a l'etude geologique du Secteur du Peloponnese Septentrional." PhD thesis. Universite de Paris.

Doutsos, T. and S. Kokkalas (2001). "Stress and deformation patterns in the Aegean region." In: *Journal of Structural Geology* 23, pp. 455–472.

Doutsos, T., I. Koukouvelas, and P. Xypolias (2006). "A new orogenic model for the External Hellenides. In: Robertson, A.H.F. & Mountrakis, D. (eds) Tectonic Development of the Eastern Mediterranean Region." In: *Geological Society, London, Special Publications* 260, pp. 507–520.

Doutsos, T. and G. Poulimenos (1992). "Geometry and kinematics of active faults and their seismotectonic significance in the western Corinth-Patras rift (Greece)." In: *Journal of Structural Geology* 14, pp. 689–699.

Egeland, D. (2018). *Fault Displacement Analysis in the Kalavryta Region of the Corinth Rift System, Greece. Master Thesis.*

Einsele, G. (2000). "Sedimentary Basins - Evolution, Facies and Sediment Budget". In: *Heidelberg, Germany: Springer.*

Exadaktylos, G., I. Vardoulakis, M. Stavropoulou, and P. Tsombos (2003). "Analogue and numerical modelling of normal fault patterns produced due to slip along a detachment zone." In: *Techonophysics* 376, pp. 117–134.

Faleide, J. I., K. Bjørlykke, and R. Gabrielsen (2010). "Geology of the Norwegian Continental Shelf." In: *Petroleum Geoscience: From Sedimentary Environments to Rock Physics*, pp. 467–499.

Flotte, N. (2003). "Characterisation structurale et cinematique d'un rift sur detachement: le rift de Corinthe-Patras, Grece." PhD thesis. Universite Paris Xi Orsay.

Ford, M., M. Hemelsdael, M. Mancini, and N. Palyvos (2016). "Rift migration and lateral propagation: Evolution of normal faults and sediment-routing systems of the western Corinth rift (Greece)." In: *Geological Society London Special Publications 439* 1.

Ford, M., S. Rohais, E. Williams, S. Bourlange, N. Backert, F. Malartre, R. Notre, and V. Nancy (2013). "Tectono-sedimentary evolution of the western Corinth rift (Central Greece)." In: *Basin Research, IAS EAGE*, pp. 3–25. DOI: 10.1111/j.1365-2117.2012.00550.x.

Gawthorpe, R. L. and M. R. Leeder (2000). "Tectono-sedimentary evolution of active extensional basins." In: *Basin Research* 12.3-4, pp. 195–218. DOI: 10.1111/j.1365-2117.2000.00121.x.

Gawthorpe, R. L., M. R. Leeder, et al. (2018). "Tectono-sedimentary evolution of the Plio-Pleistocene Corinth rift, Greece." In: *Basin Research* 30, pp. 448–479.

Gibbs, A. D. (1984). "Structural evolution of extensional basin margins." In: *J. Geol. Soc. London* 141, pp. 609–620.

Goldsworthy, M. and J. Jackson (2001). "Migration of activity within normal fault systems: examples from Quaternary of mainland Greece." In: *Journal of Structural Geology* 23, pp. 489–506.

Hemelsdaël, R., M. Ford, F. Malartre, and R. Gawthorpe (2017). "Interaction of an antecedent fluvial system with early normal fault growth : Implications for syn-rift stratigraphy, western Corinth rift (Greece)". In: *International Association of Sedimentologists*. DOI: 10.1111/sed.12381.

Hyndman, R., A. Koehler, K. Ord, and R. Snyder (2008). *Forecasting with Exponential Smoothing: The State Space Approach.* Springer.

Jolivet, L., J.P. Brun, P. Gautier, S. Lallemeant, and M. Patriat (1994). "3D kinematics of extension in the Aegean region from the early Miocene to the present, insights from the ductile crust." In: *Bulletin de la Societe Geologique de France* 165, pp. 195–209.

Jolivet, L. and C. Faccenna (2000). "Mediterranean extension and the Africa-Eurasia collision." In: *Tectonics* 19.6, pp. 1095–1106.

Kontopoulos, N., G. Poulimenos, A. Zelilidis, and T. Doutsos (1993). "Geometry of trapezoidal fan deltas and their relationship to extensional faulting along the southwestern active margins of the Corinth rift, Greece." In: *Basin Research* 5.February 2014, pp. 179–192.

Lambotte, S. et al. (2014). "Reassessment of the rifting process in the Western Corinth Rift from relocated seismicity." In: *Geophysical Journal International* 197, pp. 1822–1844.

Laux, D. and A. Henk (2015). "Terrestrial laser scanning and fracture network characterisation - Perspectives for a (semi-) automatic analysis of point cloud data from outcrops." In: *Zeitschrift der Deutshen Gesellschaft fur Geowissenschaften* 166, pp. 99–118.

Le Pichon, X. and J. Angelier (1979). "The hellenic arc and trench system: a key to the neotectonic evolution of the eastern Mediterranean area." In: *Tectonophysics* 60, pp. 1–42.

Mannie, S. A., A. C. Jackson, J. G. Hampson, and J. A. Fraser (2016). "Tectonic controls on the spatial distribution and stratigraphic architecture of a net-transgressive shallow-marine synrift succession in a salt-influenced rift basin: Middle to Upper Jurassic, Norwegian Central North Sea." In: *Journal of the Geological Society* 173(6), pp. 2016–2033.

Models, The Geo and P. Prince (2018). "Normal fault sandbox model: Rift-style faulting using a stretching base layer". In: *Virginia Tech Active Tectonics and Geomorphology Lab*. URL: http://tiny.cc/i7615y.

Moretti, L., D. Sakellariou, V. Lykousis, and L. Micarelli (2003). "The Gulf of Corinth: an active half graben?" In: *Journal of Geodynamics* 36, pp. 323–340.

Mostafa, E. K. A. (2017). *Subsurface investigation in the Gulf of Corinth (GoC), Greece. Master Thesis.*

Nixon, C., T. J. Henstock, D. Christodoulou, M. Ford, B. Taylor, and D. Sakellariou (2016). "Rapid spatiotemporal variations in rift structure during development of the Corinth Rift, central Greece." In: *Tectonics* 35, pp. 1225–1248. DOI: 10.1002/2015TC004026.

Okay, A., E. Demirbag, H. Kurt, N. Okay, and I. Kuscu (1999). "An active, deep marine strike-slip basin along the North Anatolian fault in Turkey." In: *Tectonics* 18.1, pp. 129–147.

Oppedal, E. (2017). *Rift segmentation: structural mapping of syn-rift successions between Kerpini-Tsivlos and Mamoussia-Pirgaki faults, Greece. Master Thesis.*

Prosser, S. (2000). "Rift-related linked depositional systems and their seismic expression." In: *Tectonics and Seismic Sequence Stratigraphy* 71, pp. 35–66.

Ravnas, R. and J. Steel (1998). "Architecture of Marine Rift-Basin Successions." In: *AAPG Bulletin* 82.January 1998, pp. 110–146.

Reilinger, R., S. Mcclusky, S. Ergintav, D. Paradissis, and P. Vernant (2010). "Geodetic constraints on the tectonic evolution of the Aegean region and strain accumulation along the Hellenic subduction zone." In: *Tectonophysics* 488(1), pp. 22–30.

Rietbrock, A., C. Tiberi, F. Scherbaum, and H. Lyon-Caen (1996). "Seismic slip on a low angle normal fault in the Gulf of Corinth: Evidence from a high-resolution cluster analysis of microearthquakes". In: *Geophysical Research letters* 23, pp. 1817–1820.

Salveson, J.O. (1981). "Rift basins – A tectonic model." In: *Abstracts of Papers presented to the conference on Processes of Planetary Rifting. A Lunar and Planetary Institute Topical Conference held December 3-5, 1981, in Napa Valley, CA.* 1, pp. 39–42.

Schlische, W. R. and M. O. Withjack (2002). "Tectonics of Rifting and Drifting: Pangea Breakup - Rift Basin Architecture and Evolution." In: *Lamont-Doherty Earth Observatory, Columbia University, Earth Institute.*

Setkowicz, J. (2014). *Evaluation of algorithms and tools for 3D modeling of laser scanning data.*

Sigmundstad, E. (2016). *Detailed structural mapping and correlation of a thick syn-rift sequence in the kerpini fault block, Greece. Master Thesis.*

Sorel, D. (2000). "A Pleistocene and still-active detachment fault and the origin of the Corinth-Patras rift, Greece." In: *Geology* 28, pp. 83–86.

Syahrul, R. A. (2014). *Fault Controlled Sedimentation: A Case Study of the Kerpini Fault, Greece. Master Thesis.*

Taylor, B., R. J. Weiss, M. A. Goodlife, M. Sachpazi, M. Laigle, and A. Hirn (2011). "The structures, stratigraphy and evolution of the Gulf of Corinth, Greece." In: *Geophysical Journal International* 185(3), pp. 1189–1219.

Westaway, R. (2002). "The Quaternary evolution of the Gulf of Corinth, central Greece: coupling between surface processes and flow in the lower continental crust." In: *Tectonophysics* 348, pp. 269–318.